PolyPublie
Polytechnique Montréal

POLYTECHNIQUE MONTRÉAL
UNIVERSITÉ D'INGÉNIERIE

Titre: Title:	Design and Implementation of a High Power Pulsed Source for Biomedical Imaging
Auteur: Author:	Justine Rakotomalala
Date:	2024
Type:	Mémoire ou thèse / Dissertation or Thesis
Référence: Citation:	Rakotomalala, J. (2024). Design and Implementation of a High Power Pulsed Source for Biomedical Imaging [Master's thesis, Polytechnique Montréal]. PolyPublie. https://publications.polymtl.ca/58352/

Document en libre accès dans PolyPublie
Open Access document in PolyPublie

URL de PolyPublie: PolyPublie URL:	https://publications.polymtl.ca/58352/
Directeurs de recherche: Advisors:	Denis Seletskiy, & Frédéric Lesage
Programme: Program:	Génie physique

Ce fichier a été téléchargé à partir de PolyPublie, le dépôt institutionnel de Polytechnique Montréal
This file has been downloaded from PolyPublie, the institutional repository of Polytechnique Montréal

https://publications.polymtl.ca

POLYTECHNIQUE MONTRÉAL
affiliée à l'Université de Montréal

Design And Implementation Of A High Power Pulsed Source For Biomedical Imaging

JUSTINE RAKOTOMALALA
Département de génie physique

Mémoire présenté en vue de l'obtention du diplôme de *Maîtrise ès sciences appliquées*
Génie physique

Mai 2024

© Justine Rakotomalala, 2024.

POLYTECHNIQUE MONTRÉAL
affiliée à l'Université de Montréal

Ce mémoire intitulé :

Design And Implementation Of A High Power Pulsed Source For Biomedical Imaging

présenté par **Justine RAKOTOMALALA**
en vue de l'obtention du diplôme de *Maîtrise ès sciences appliquées*
a été dûment accepté par le jury d'examen constitué de :

Clara SANTATO, présidente
Denis SELETSKIY, membre et directeur de recherche
Frédéric LESAGE, membre et codirecteur de recherche
Frédéric LEBLOND, membre

DEDICATION

Here is to you S,
Lumière de mon existence!

ACKNOWLEDGEMENTS

Just like it takes a village to raise a child, this master research has been made possible by the help and contribution of numerous people. It is time to give credit where credit is due.

First of all I would like to extend my most heartfelt gratitude to my research directors: Denis Selestkiy and Frederic Lesage. Thank you for this opportunity to work in your laboratory. Their respective expertise is what I strive to achieve and I cannot wait to carry on this subject in thesis.

Thank you to professor Nicolas Godbout, director of the Laboratoire des Fibres Optiques (LFO) for letting me use the LFO. Credit is due also to Mikael Leduc. Mikael's expertise has saved on more than one occasions my fibers and he is the reason amplification was possible.

Similarly, I would like to take this opportunity to thank Laurent Mouden, for his expertise on Ultrafast oscilloscope and his kindness.

To Patrick Delafontaine-Martel, thank you for your kindness and your help. Patrick dedicated time to ensure the the coupling of the pump and signal with the fiber.

I would also like to express my sincere appreciation to Lyne Denommé for her unwavering support and assistance through my academic journey.

How could I not thank my family and friends. To my parents, who always gently encourage me to strive for perfection, to my brother and sister for their support through thick and thin (with the occasional cookie matcha and meme), and of course to my friends for bringing me out of my submarine-survival-zone, most of the time despite my protestations. Your unwavering support is truly flabbergasting.

Lastly, I would like to thank you, S, you magnificent, sneaky, sweet, light bubble. Nothing, not even the biggest horde of dementors stands a chance against you.

To all of you, thank you.

RÉSUMÉ

La microscopy multiphotonique est une technique d'imagerie médicale présentant de nombreux avantage, en terme de résolutions et de profondeur de tissu biologique atteignable. Cependant le phénomène à l'origine de la technique -l'absorption multiphoton- de hautes puissances pour être significatif et l'utilisation des pulses pico-femto est employée afin de prévenier totue dégradation du tissu biologique. L'objectif de ce travail est de développer un source pulsée à haute puissance afin de pouvoir réaliser ces applications. Ce travail est divisé en deux parties.

Tout d'abord, la conception du stretcher et du compresseur. Cette partie du travail est réalisé en plusieurs étapes. Dans un premier temps, on néglige la contribution de la fibre et de la déformation du front d'onde dû aux aberrations optiques. Le but est de sélectionner les optiques et les configurations permettant d'obtenir un stretcher et compresseur tout deux générant une Group Delay Dispersion de 11.44 ps^2 et compensant l'ordre trois. Dans toute cette étude, les ordres supérieurs sont négligés. Ce GDD théorique est obtenu par deux configurations types: Offner pour le stretcher et Treacy pour le compresseur. Seules les positions relatives des optiques sont autorisées à différer, l'angle d'incidence du stretcher et du compresseur doivent être strictement identiques, sans quoi des phases spectrales résiduelles significatives risquent d'impacter le profile final du pulse. L'angle d'incidence est limité la configuration du compresseur et est fixé à 52°, les longueurs caractéristiques respectives sont fixées à 36.15cm et 2.577 cm. Les focales des miroirs du montage du stretcher sont fixées à 200mm et 100mm. Les efficacités théoriques sont estimées à 60% et 40% pour respectivement le compresseur et le stretcher.

Une fois la paire idéale de stretcher/compresseur conçue, on introduit la contribution de la fibre. Cette dernière est faible par rapport aux Group Delay Dispersion et Third Order Dispersion générés dans les montages précédents, aussi une solution est de légèrement dérégler le stretcher et le compresseur afin de compenser le GDD de la fibre. Cependant, si l'intégralité du GDD de la fibre était compensée ainsi, le TOD résiduel serait catastrophique. Pour éviter une dégradation du profil du pulse, le GDD de la fibre n'est compensé que partiellement par dé-réglage, une partie de la phase résiduelle étant compensée par la génération d'aberrations optiques. On obtient ainsi de manière théorique un Group Delay Dispersion résiduel de -24fs^2 et un Third Order Dispersion résiduel de -31000 fs^3. Ces phases résiduelles induisent une variation de 0.2% sur le profil final du pulse.

La conception de la paire achevée, la solution est implémentée expérimentalement et les pulses de sortie caractérisés à l'aide d'un oscilloscope ultra-rapide. La précision de mesure est de 25ps, néanmoins on obtient des durées de pulses respectives de 291 ps et 306 ps dans un premier temps -l'ordre 3 modifie de manière significative le profil à la sortie du stretcher et à la sortie du compresseur. Un réalignement correctif est réalisé, et l'ensemble stretcher/compresseur - sans la fibre - est caractérisé par autocorrélation interférométrique. La durée du pulse est alors estimée à 631 fs.

Dans un second temps, l'amplificateur a été développé. Pour ce faire, un premier modèle numérique a été implémenté afin de réaliser une première estimation des gains atteignables, les longueurs de fibres à considérer et le la répartition des populations électroniques. Bien que cette simulation ne puisse ne aucun cas être une représentation fidèle d'une amplification pulsée, elle sert de base à la dynamique des populations électroniques et offre un premier ordre de grandeur pour la longueur de fibre minimale nécessaire, à savoir ~ 0.7m, ainsi que les ordres de grandeurs de bruits minimum, estimés à 5dB et le gain, estimé à 25dB. Ces résultats sont utilisés comme base dans l'implémentation d'une méthode numérique dépendante du temps. En effet, à cause de la durée du pulse, de la longueur de la fibre et des puissances en jeu, implémenter la dépendance temporelle dans la simulation d'état stationnaire demanderait une puissance de calcul irraisonnable -une des raisons pour laquelle la dynamique EYDFA est pour la grande majorité implémentée en état stationnaire. Face à cette difficulté technique, une autre approche de l'estimation du gain pulsé est proposé. En effet, étant donné le temps caractéristique du système pour atteindre l'équilibre, et la durée séparant deux pulses, le système n'a pas le temps de se remettre de changements drastiques. De fait, on considère que le régime pulsé présent est une faible variation autour de l'état d'équilibre précédemment déterminé. On tolère pour ce faire de faibles variations de longueur et de populations électroniques et le pulse est associé à un profile rectangulaire. L'estimation du gain pour le pulse gaussian de puissance de crête initial de I0 est supposée être la valeur moyenne entre le gain calculé pour un profile rectangulaire de puissance de crête de I0 et de I0/2 . Ces approximations conduisent à une estimation d'une puissance moyenne maximale de 4.73 ± 1.13W dans le cas d'un signal entrant à 0.040 W de puissance moyenne et de puissance de pompe de 30W.

Le gain maximal atteignable ayant été estimé, il est nécessaire de prendre en compte la contribution de l'amplification de l'émission spontanée. La puissance du signal d'entrée étant faible, on doit s'attendre à des puissances significatives. Pour y remédier, il est nécessaire d'ajouter un pré-amplificateur. Cependant, ajouter une interface augmente la complexité du

montage, ainsi que les pertes. De fait, on préfère plutôt allonger la longueur de la fibre. En effet, cette longueur supplémentaire n'est pas alimentée par la pompe -car cette dernière a été absorbée par la section précédente- et en conséquence l'absorption du signal issue de l'amplification de l'émission spontanée issue des ions Ytterbiums, à 1030nm, est favorisée. De fait, la puissance d'amplification de l'émission spontanée se propageant dans le sens inverse est utilisée comme source de pré-amplification du signal.

Ce modèle de gain a été confronté avec des premiers résultats expérimentaux, réalisé à une puissance de pompe à 6W pour un signal à 20mW de puissance moyenne. La valeur expérimentale est de l'ordre de 0.1 W, ce qui est bien l'ordre de grandeur prédite par le modèle: 0.0836 ± 0.0278 W. Ces résultats sont d'autant plus satisfaisant qu'ils sont réalisés à faible puissance, là ou l'amplification de l'émission spontanée est favorisée par le système, ce qui tend à montrer l'efficacité des stratégies mises en place pour limiter l'impact de l'amplification du signal d'émission spontanée.

ABSTRACT

Multiphoton microscopy paves the way for new biomedical imaging, but requires high peak power for the multi-photon absorption to take place. To prevent destroying the biological tissue, the solution is pulsed light. To this end, this work aims at developing a 4 W pulsed source from a 100 fs-laser source, at 100 mW average power and repetition rate 100 MHz. Given the duration of the pulse, amplification as it is would result in significant nonlinear effects and the peak power of the output would be impacted. To prevent this, the beam is amplified through Chirp Phase Amplification (CPA). The chirp is introduced in a grating-based stretcher setup, which induces spectral phase resulting in 300x broadening in the duration of the pulse envelope. The pulse is then amplified and compressed back into its original profile by applying reverse spectral phase.

The quality of CPA is highly dependent on the stretcher/compressor pair. This is achieved through successive steps, first by assuming ideal optics and considering spectral dispersion to the third order of Tailor expansion around the center frequency. To this end various configurations are reviewed -Offner's, Treacy's, and Martinez's - until compensation is achieved. To this end, the compressor is a Treacy's grating pair separated by 2.577 cm and the stretcher is an Offner's configuration with focals of 200mm and 100mm, a grating distance of $\sim$ 36.15 cm. The incident angle is 52 °resulting accumulated Group Delay Dispersion (GDD) of 11.44 ps^2 (of opposite signs) in both cases. The second step is to take into account the fiber's dispersion. To compensate it, the stretcher/compressor are slightly put off-balance and optical aberrations are generated in the stretcher to compensate both order 2 and 3. In theory, a residual GDD of 24 fs^2 and Third Order Dispersion (TOD) of $\sim$ -31 000 fs^3 is achieved. The implementation faces uncertainty to angle and position, but pulses at 291 and 306 ps are achieved with power efficiency at 60% and 40%. The alignment of the optics is corrected and the stretcher/compressor's output is characterized with an interferometric autocorrelator setup,

The second step is to design the amplifier. To do so, a numerical simulation in steady state of Erbium/Ytterbium Co-doped fiber amplifier is first implemented, yielding a 25 dB gain, a noise level of 5dB, for a length of $\sim$ 0.7m and a pump power of 30W. In order to better estimate the gain one can expect in pulsed-amplification, another numerical simulation is implemented, though not by modifying the steady state code to fit time dependence but by considering the system to be at a near equilibrium and allowing small variations. This

hypothesis is supported by the relaxation time characteristic of Erbium Ytterbium Doped Fiber Amplifier (EYDFA) -$\sim$ 100 μs- and the time duration between two pulses -0.1 ns- meaning the system does not have time to significantly recover between two amplification. The model predicts an average power of 4.73 $\pm$ 1.13 W for an initial pulse of 0.040W. To check this estimation, small power amplification is first done at a pump power of 6W with an average power of the signal set at 0.020 W. The output average power is estimated at 0.1 W, which is within the prediction of the model: 0.0836 $\pm$ 0.0278 W.

TABLE OF CONTENTS

DEDICATION iii

ACKNOWLEDGEMENTS iv

RÉSUMÉ v

ABSTRACT viii

TABLE OF CONTENTS x

LIST OF TABLES xiii

LIST OF FIGURES xiv

LIST OF SYMBOLS AND ACRONYMS xix

LIST OF APPENDICES xxi

CHAPTER 1 INTRODUCTION 1
1.1 A general introduction 1
1.1.1 Light-Matter interaction and Photodamage 4
1.1.2 Multiphoton Imaging 7
1.1.3 Optical amplification 10
1.1.4 Ultrafast Photonic and non-linear effects 11
1.2 Research Objectives 12
1.2.1 Objective 1 13
1.2.2 Objective 2 13
1.3 Thesis outline 13

CHAPTER 2 LITERATURE REVIEW 15
2.1 Optical amplifiers 15
2.2 Stretcher-Compressor 16

CHAPTER 3 STRETCHER AND COMPRESSOR DESIGN 18
3.1 General Theory of Pulse Chirp 18
3.1.1 Definition and conventions 19

3.1.2 Mathematical development and pulse modulation 21
3.1.3 Return to physics 23
3.2 Theory of Pulse Chirp in Free Space 24
3.2.1 A brief review on gratings 24
3.2.2 Grating Diffraction Theory 25
3.2.3 Grating Chirp Generation 27
3.3 Ideal Configuration Design 29
3.3.1 Theoretical target 29
3.3.2 Grating selection 30
3.3.3 Configuration study 33
3.4 Residual spectral phase 47
3.4.1 High Order and pulse sensitivity 47
3.4.2 Fiber dispersion 48
3.4.3 Aberrations generation 51
3.5 Experimental results 56
3.5.1 System precision 56
3.5.2 The power efficiency 60
3.5.3 Chirping of the pulse 61
3.5.4 Interferometric autocorrelator 63

CHAPTER 4 ERBIUM YTTERBIUM CO-DOPED AMPLIFICATION 69
4.1 Amplification theory 69
4.1.1 Definition and principles 69
4.1.2 Choice of Dopant 71
4.1.3 Rate and Propagation equations 72
4.2 Steady State Amplification 74
4.2.1 Algorithm structure 74
4.2.2 Constant Estimation 76
4.2.3 Numerical precision evaluation 78
4.2.4 Amplifier Optimization 80
4.3 Pulse amplification 83
4.3.1 Initial Time dependant simulation 83
4.3.2 Time dependant evaluation 84
4.3.3 ASE estimation and final fiber length 90
4.4 Experimental results 91
4.4.1 Presentation of the setup 91

4.4.2 Preliminary observations 92

CHAPTER 5 CONCLUSION 93
5.1 Summary of Works 93
5.2 Limitations 93
5.3 Future Research 94

REFERENCES 96

APPENDICES 100

LIST OF TABLES

Table 3.1	Pulse characteristic of the seed laser source (NKT Photonics)	24
Table 3.2	Fiber dispersion values (from [1])	48
Table 3.3	Seidel's coefficients formula in the case of an Offner stretcher	52
Table 3.4	Final compressor parameters and aberration generation	55
Table 3.5	Calculated values of GDD and TOD in all sections of the setup . . .	55
Table 4.1	Numerical parameters of the steady state simulation of EYDFA . . .	80
Table 4.2	powers of both signal, pump, and ASE noises, in a forward an backward configuration	82
Table 4.3	Time characteristics of electronic transitions, estimated in magnitude.	84
Table A.1	Cross-section values of EYDFA (source N-Light) in $10^{-25}\mathrm{m}^2$	100
Table A.2	Fiber characteristics (source Coherent, Nufern)	100
Table A.3	Reflection coefficient Treacy (source Spectrogon, Thorlab). All values are taken for a wavelength of 1573nm, in all cases, the mirrors are coated and aluminium, and the angle of incidence is 8° unless mentioned otherwise	100
Table A.4	Reflection coefficient Martinez (source Spectrogon, Thorlab). All values are taken for a wavelength of 1573nm, in all cases, the mirrors are coated and aluminium if not mentioned otherwise	100
Table A.5	Reflection coefficient Offner (source Spectrogon, Thorlab, Eskma). All values are taken for a wavelength of 1573nm, in all cases, the mirrors are coated and aluminium if not mentioned otherwise (S for Silver) .	100

LIST OF FIGURES

Figure 1.1 Light propagation in a biological medium. Light is either absorbed at focused length, absorbed by higher layers or scattered in another direction. 1

Figure 1.2 Jablonski Diagram illustrating bioluminescent mechanism. In blue the absorption in resonance, leading to in grey a non radiative transition. Either the emission of a photon (in green, fluorescence) or an intercrossing transition to a triplet leads to an emission of a photon (in red, phosphorescence). Figure inspired from [2] 3

Figure 1.3 Illustration of off-resonance transitions. Virtual states are at play in the transitions. Rayleigh scattering is an elastic transition, while Raman scattering is inelastic, in both cases (smaller energy in the emission photon, aka Stokes and higher energy in the emission photon aka AntiStokes). Figure inspired from [2] 4

Figure 1.4 Illustration of Multi-photon microscopy and 1-photon microscopy (present case 2 photon microscopy)). Because of the proportionality between the fluorescence emission irradiance and the initial irradiance square the area where the fluorescence takes place is more limited. 8

Figure 1.5 Water absorption relative to the wavelength. The data is attributed to Kebes and, under This file is licensed under the Creative Commons Attribution-Share Alike 3.0 Unported license [3]. 9

Figure 1.6 Amplification through population inversion. In dark blue the transitions associated to the pump power and in red the transitions associated to the signal. 10

Figure 1.7 non-linear Schrödinger equation, in this form, the Raman effect was simplified and the associated integral reduced to a constant over the pulse bandwidth. 11

Figure 1.8 Illustration of non-linear effects. The pulse is a 100-fs with a peak power at 100mW. The figures were obtained through the implementation of a classic Split-Step Fourier Method 12

Figure 3.1 Dispersion of light under a reflecting grating. By convention, diffraction orders on the same side of the incident light are negative. In this case, only the order -1 is represented, along with the order 0 (pure reflection without diffraction). 26

Figure 3.2 Evolution of the bandwidth cut-off imposed by the grating. The incident angle is 52°, which is the result of the iterative process of conception of both the stretcher and the compressor for the first diffraction order. 31
Figure 3.3 Evolution of variation of angle introduced relative to the grating spacing. The selected bandwidth is the interval [1550,1620]nm, with an incident angle of 52° -the choice value of the incident angle will be detailed later in this chapter 32
Figure 3.4 Evolution of the minimal angle allowed by the grating given the wavelength. The section is red is the area of interest: the beam has a central wavelength of 1573 nm and a bandwidth of 38.9 nm. 33
Figure 3.5 The Martinez Grating pair in its symmetric configuration (both lens are identical). Because of this, it is possible to reduce this setup's size by placing a plane mirror in the plane of focus common to both lens. While this simplifies the setup and prevent potential missmatch between the two lens and the two grating, it also leads to chromatic aberrations. f is the focal length of the lens, x is the relative position of the grating to the focal point. 34
Figure 3.6 Evolution of the stretch ratio given the focal length of the lens. In blue the maximum stretch ratio the system can yield, relative to the focal length of the lens, in red the stretch ratio required by the system and so the minimum stretch ratio expected of the setup 36
Figure 3.7 Evolution of focal length of the lens needed to achieve a GDD of 11.44 ps^2, relative to the incident angle. 37
Figure 3.8 Evolution of available configuration. 38
Figure 3.9 Evolution of the grating position given the incident angle of the input pulse. Each color corresponds to a different focal length: in red a focal length of 10cm, in green a focal length of 20cm and in blue a focal length of 40cm. The dotted lines represent the maximum value the grating position can take (stemming from the definition of the grating position along with physical constraint the grating is putting on the setup) 39

Figure 3.10 Evolution of the minimum lens diameter relative to the incident angle. Once again each color corresponds to a focal length of 10, 20 and 40 cm for the red, green and blue respectively. Straight lines correspond to the minimum diameter in inch while the dotted lines correspond to the available space between the incident ray optical path of the highest wavelength of the pulse spectrum. 40
Figure 3.11 Caption Offner setup (from above and side) 41
Figure 3.12 Evolution of the Stretch Ratio relative to the focal length of the mirror R1, in blue the stretch ratio obtain for an incident angle of 51.44°, the red dotted line in the minimal stretch required. 42
Figure 3.13 Evolution of the position of the grating relative to the incident line. One color is used per focal length -blue, green and red for respectively a focal of 10, 2-, and 4cm. The dotted line represent the minimum value taken by the grating. 43
Figure 3.14 Evolution of the minimum diameter of the concave mirror M_1 required given the interval of wavelength. The dotted lines represent the space available between the incident beam and the diffracted beam. 44
Figure 3.15 Treacy compressor design. Both gratings are oriented with the same angle relative to the incident light and separated by a distance b. This is the 2-gratings configuration, where the beam is reflected by a plane mirror, with an angle relative to the plane zOy as to separated the input from the output. s is the size of the diffracted beam, a is the space between the minimal diffraction angle and the incident light, b is the spacing between the gratings 45
Figure 3.16 Treacy compressor design. S is the size of the diffracted beam at the reflection mirror, blue is the relative grating position associated to the incident angle, and in yellow is the space between the incident beam and the smallest diffraction optical path. 46
Figure 3.17 Evolution of the maximum power peak given the order of residual phase 47
Figure 3.18 Evolution of the input pulse in blue before the stretcher and the output pulse in red after the compressor. The input pulse has a FWHM of 100 fs while the output pulse is of 850.98 fs 49

Figure 3.19 Evolution of the input pulse in blue before the stretcher and the output pulse in green after the compressor. In this case, the residual second order spectral phase generated by the fiber was compensated by off-balancing the Treacy Compressor, generating a residual TOD of $0.00125 ps^3$. 50
Figure 3.20 Evolution of residual GDD, TOD and TOD^{GDDab} given the values of the (x_o, y_o) 53
Figure 3.21 Final output pulse expected, after evaluation of the material dispersion and compensation through off-balance and aberrations. The Pearson correlation coefficient is estimated at 0.998. 56
Figure 3.22 Evolution of the pulse half width full maximum relative to the residual order two present. The red dotted line represent respectively the initial pulse width along with the ten-time pulse width limit. 57
Figure 3.23 Evolution of the relative error given the angle's uncertainty 58
Figure 3.24 Alignement of a beam through iris. The maximum intensity detected is reach when the beam is paralel to the optical axis. 58
Figure 3.25 Normal distribution with percentile: in blue the 68.5%, in green the 95% percentile,percentile, both centered around the mean μ=0 and in yellow the 7% percentile associated to the uncertainty deviation . . . 59
Figure 3.26 In blue the evolution of the relative error made on the GDD induced by the variation on incident angle, in red the limit at 0.1%. 60
Figure 3.27 Evolution of the maximum power peak given the order of residual phase. 62
Figure 3.28 Diagram of an interferometric autocorrelator. Mirror M_1's position x_o is used as reference while M_2 mirror x varies. 64
Figure 3.29 IAC trace of the laser source in blue, in red the gaussian fit with a FWHM set at 120.02 fs 65
Figure 3.30 IAC trace of the laser source in blue, in red the gaussian fit with a FWHM set at 127 fs 66
Figure 3.31 IAC trace of the stretched/compressed pulse in blue, after prossessing to substract background 67
Figure 3.32 IAC trace of the stretched/compressed pulse in blue, in orange the signal filtered out of noise (frequency cut-off at 32.10^{11} Hz), in red the gaussian fit 67

Figure 4.1 Figure of the energy levels of an ytterbium/erbium pair. The arrows in red represent the transitions driven by the pump power, in orange the transitions driven by the signal -indirect dependence of the cross transitions through the population concentration. The arrows in blue corresponds to spontaneous emissions, with dotted lines being non radiative transitions. Green is associated with up-conversion. 72
Figure 4.2 Structure of the algorithm in steady state. Power and Constants are both classes introduced during the initialisation and called upon and updated during the loop 75
Figure 4.3 Evolution of the final output power relative to the spatial spacing (m) 79
Figure 4.4 Simulation results for initial values of signal power and available pump power. 81
Figure 4.5 Structure of the time-dependant algorithm. 88
Figure 4.6 Evolution of the electronic populations of the high energy levels of the Erbium-Ytterbium pair, relative to the position in the fiber along with the initial peak power. The values are the peak power of the pulse before entering the fiber. 89
Figure 4.7 Power evolution relative to the fiber length 90
Figure 4.8 Amplification set up, inspired from [1] 92

LIST OF SYMBOLS AND ACRONYMS

QPI	Quantitative Phase Imaging
SThM	Scanning Thermal Microscopy
SPM	Self Phase Modulation
CPA	Chirped Pulse Amplification
GVD	Group Phase dispersion
GDD	Group Delay dispersion
TOD	Third Order Dispersion
FOD	Fourth Order Dispersion
ASE	Amplified Spontaneous Emission
EDFA	Erbium doped fiber Amplifier
EYDFA	Erbium Ytterbium doped fiber Amplifier
EDF	Erbium Doped Fiber
Yf-ASE	Ytterbium Forward Amplified Spontaneous Emission
Yb-ASE	Ytterbium Backward Amplified Spontaneous Emission
Ef-ASE	Erbium Forward Amplified Spontaneous Emission
Eb-ASE	Erbium Backward Amplified Spontaneous Emission
CW	Continuous Wave
FROG	Frequency-resolved optical gating
FWHM	Full Width Half Maximum
NF	Noise Figure
SNR	Signal to Noise Ratio
ESA	Excited State Absorption
DC	Direct Current
AC	Alternating Current
ELS	Elastic Light Scattering
DLS	Dynamic light Scattering
OCT	Optical Coherence Tomography
SOA	Semiconductor Optical Amplifier
RSS	Raman Stimulated Scattering
DFA	Doped Fiber Amplifier
LIDT	Laser Induced Damage Threshold
MMDG	Metallic Multilayer Dielectric Grating
MDG	Multilayer Dielectric Gratings

TM	Transverse Magnetic
OA	Optical Amplifier
NA	Numerical Aperture
IAC	Interferometric AutoCorrelation

LIST OF APPENDICES

Appendix A Characteristics 100

CHAPTER 1 INTRODUCTION

Multiphoton microscopy opens new possibilities in terms of biomedical imaging. Indeed, since the phenomena at play necessitate high coherence and high energy, it is more localized than its equivalent one-photon microscope. As such, it allows for imaging thinner layers. Of course, the trade-off entails challenging conditions for the input signal. Firstly, as multiphoton absorption cross sections are significantly lower than their one-photon equivalent, the power must be higher. Additionally, the temporal shape of excitation light source is impacted; short pulses are necessary both to ensure high coherence between photons and to prevent significant photo-damage from taking place. Designing such a source necessitates reaching both high power and short pulse duration.

1.1 A general introduction

At the core of biological imaging lies the interaction between light and matter. Light is directed into biological tissues, where it interacts with matter depending on the properties of the layers. Therefore, from the collected light, it is possible to deduce the optical properties encountered by the light and thereby infer the composition and dynamics of the biological tissue.

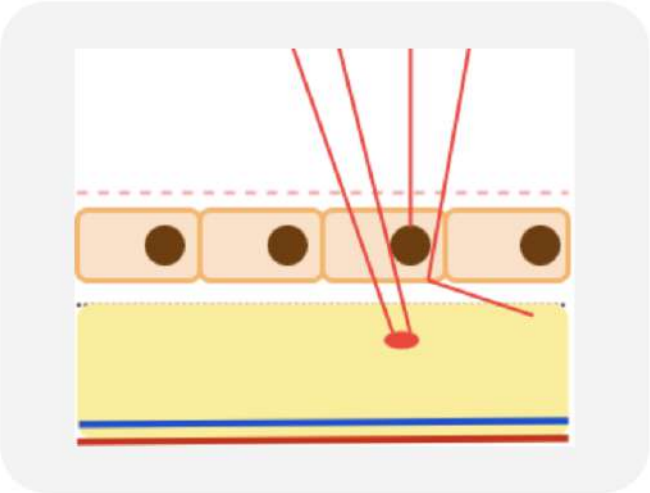

Figure 1.1 Light propagation in a biological medium. Light is either absorbed at focused length, absorbed by higher layers or scattered in another direction.

When it comes to light-matter interaction, transitions are classified in three groups:

Photon absorption at resonance: meaning the energy of the photon corresponds to the energy difference between two quantum states of the matter. In the case of multi-photon absorption -theorized by Marie Goeppert Mayer in 1930- the sum of the photons' energy corresponds to the energy difference between two quantum states of the matter.

Photon Emission at resonance: which is the equivalent phenomenon of photon absorption at resonance, meaning the emitted photon's energy corresponds to the energy difference of two quantum states of the matter. Depending on the presence or the absence of an input photon, the emission is called stimulated emission -the former- or spontaneous emission -the latter. Both dynamics are described in details in Chapter 2 (though it is done so in the context of light amplification, the principles remain the same). In bioimaging, the emission of a photon at the exact wavelength of absorption is rarely ideal. The most is bioluminescence microscopy, which is the emission of a photon at lower energy of the input light, meaning a longer wavelength. From this it is easy to differentiate the input light from the signal resulting from the light-matter interaction. The properties of the resulting light depends on the quantum states at play, whether it be in terms of energy gap or spin. Figure 1.2 is a summary of the different bioluminescent phenomena. If the re-emission takes place from a singlet, the relaxation time is within the range of nanoseconds and the transition is called fluorescence. If the re-emission takes place from a triplet, the relaxation time is within the range of seconds to minutes and the transition is called phosphorescence. In both cases, polarization and phase are lost.

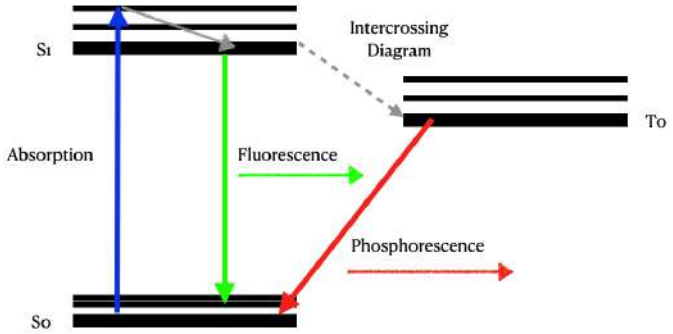

Figure 1.2 Jablonski Diagram illustrating bioluminescent mechanism. In blue the absorption in resonance, leading to in grey a non radiative transition. Either the emission of a photon (in green, fluorescence) or an intercrossing transition to a triplet leads to an emission of a photon (in red, phosphorescence). Figure inspired from [2]

Off-resonance Interaction: in which the absorption/emission does not take place at resonance, meaning virtual states are at play. There are two main source of scattering transition: Rayleigh Scattering and Raman Scattering. The former is the scattering of light by particules of smaller radius than the incident light wavelength without transfer of energy between the medium and the light beam -the transition is therefore elastic. Regarding Raman Scattering, the process is similar to the difference that there is energy transfer between the medium and the light beam through vibrational states. If the energy is transferred from light to matter, the emitted photon's wavelength is bigger than the initial one (Stokes), while the opposite transfer -from matter to light- leads to a photon with higher energy -and so smaller wavelength (Anti-Stokes). Figure 1.3 serves as a visual summary of Scattering Phenomena.

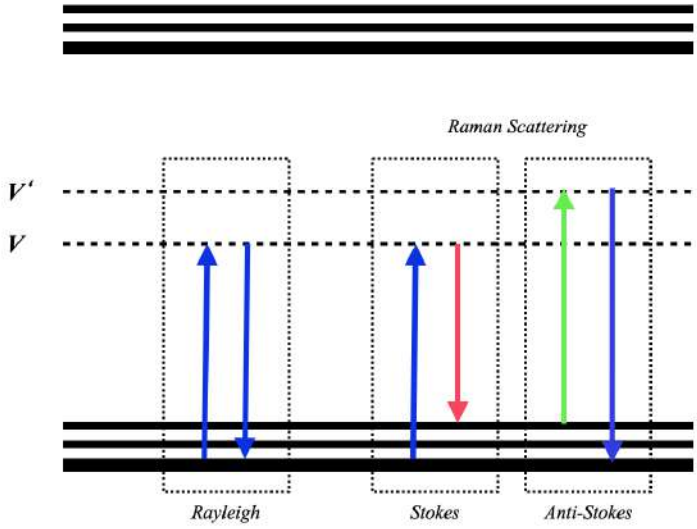

Figure 1.3 Illustration of off-resonance transitions. Virtual states are at play in the transitions. Rayleigh scattering is an elastic transition, while Raman scattering is inelastic, in both cases (smaller energy in the emission photon, aka Stokes and higher energy in the emission photon aka AntiStokes). Figure inspired from [2]

Information can be extracted from each case illustrated - Elastic Light Scattering (ELS) and Dynamic Light Scattering (DLS) are based on scattering phenomena, while Optical Coherence Tomography (OCT) and Confocal Microscopy focus on absorbed light. Designing a bioimaging tool involves selecting the information that needs to be obtained from the medium.

1.1.1 Light-Matter interaction and Photodamage

As detailed previously, the radiative transitions are at the core of microscopy fluorescence. However, as optics are tailored to target fluorophore excitation and scan the matter, in practice non radiative transitions are also expected and can lead to the degradation of the biological tissue. It is therefore paramount to evaluate the relevance of non radiative transitions and the consequences it can inflict on the tissue, so that dispositions can be taken to prevent significant alteration of the sample. As these are based on light-matter interaction, these transitions are dependant on the energy introduced in the sample and the time span of the interaction -meaning the pulse duration along with the power density and spatial confinement. The following section is a brief summary of the interactions one can expect between of the signal and the sample [2]:

1. Photochemical, continuous to 1s pulse with Power density within 10^{-3} to 10^{0} W/cm^2.
2. Photothermal 1 μs to 10^{1} s pulse with Power density within 10^{2} to 10^{6} W/cm^2.
3. Photoablative 1 ns to 1μ s pulse with Power density within 10^{8} to 10^{10} W/cm^2.
4. Photodisruptive/Photoplasmic 1 fs to 1 ns pulse with Power density within 10^{10} to 10^{14} W/cm^2.

Photochemical reactions: are dictated by continuous/long pulses -around 1 s pulse- and is due to the chemical reaction of the sample due to the radiative absorption of a photon. The following list is an enumeration of the main photochemical reactions, along with their practical applications:

1. Photodecomposition which is the dissociation of the covalent bond following the absorption of a photon.
2. Photoassociation, being the combination of two atoms, leading to the formation of a diatomic molecule (the dimerization of DNA under UV being one example).
3. Photosynthesis, being the conversation of sunlight into ATP (this process takes places in plants and provides energy).
4. Photoisomerization, being the transformation of a chemical component into another (main reaction in human vision)
5. Photoactivation, being the excitation of molecules which serve then as triggers for secondary reactions. This is the basis principle being photodynamic therapy, which is a type of cancer treatment relying on the activation of a drug in order to target the tumor cells and limit secondary effects.

Photothermal effects: as through thermal relaxation mechanism, whether it be intersystem crossing, internal conversion and relaxation through vibration. Conduction is the main factor to consider when it comes to heat dissipation -radiation being modest and convection negligeable unless the tissue is put under significant perfusion. As such in order to prevent heat deposition beyond the optical zone, light delivery must take place faster than tissue diffusivity:

$$\tau_p < \frac{r^2}{4.\kappa} \tag{1.1}$$

with r the characteristic radius of the targeted tissue, κ the thermal diffusivity and τ_p the pulse duration, with a temperature variation following:

$$\Delta T = \frac{\mu_a.F}{\rho.S} \tag{1.2}$$

where

1. μ_a is the absorption coefficient (cm^{-1})
2. E the energy deposited per volume in J/cm^3
3. S the specific heat in $J/g.^oC$.
4. F the fluence in J/cm^3

Biological tissues can withstand exposure to heat so long that the duration remains bellow a threshold value -being relative to exposure time and temperature. Under this value the photothermal effects are reversible while beyond it, the damages are permanent:

1. Hyperthermia (around 45°C) leading to cell necrosis.
2. Tissue Coagulation and loss of cell activity (50-60°C) due to the denaturation of proteins. Indeed, the shape of a protein determines its function and is ensured by hydrogen liaisons and Van den Waals bonds which are broken when excessive heat is applied on the tissue.
3. Water vaporization (100°C and above), leading to the formation of bubbles, cavity which impose stress on the medium and can lead to tissue rupture.
4. Carbonization and melting (above 300°C) in which the organic compound is reduced to carbon.

Such effects can occure at typical power density value and as such, it is paramount to evaluate the heating occuring in the sample due to light delivery. To do so:

1. Scanning Thermal Microscopy (SThM) [4], which consists in measuring temperature variations with a thermal probe. The heat transfer between the probe and the biological sample modifies the probe's properties (electrical and thermal coefficient). From the measured variation of the probe's properties the heat transfer -and so the temperature of the sample- is deduced. This technique allows to reach nanometer resolution and led to a better estimation of cell conductivity and cell necrosis in tissues.

2. Quantitative Phase Imaging (QPI), which deduces the heat variation from the retrieval of the phase [5]. As heat is induced in the sample through the light beam, the refractive index of the target area is modified relative to the temperature distribution. This variation of refractive index modify the wavefront and as such local temperature can be determined.

Photoablation: which is the destruction of a tissue through tissue vaporization, combustion or explosion. This mechanism takes place when the absorbed energy exceeds the rate at which energy can be dissipated by the tissue. One a side note, photoablation is very precise and does not induce thermal stress at the edge of the target, and as such is often used in microsurgery with the exposure to UV-Visible light.

Photodisruption: which is the effects induced by the propagation of the shock-waves (as in pressure waves) resulting from the generation of plasma. Plasma is generated when the electric field of the induced light is similar to the Coulomb field binding electrons of the biological sample. Contrary to vaporization, this does not lead to tissue rupture and as such is often used in microsurgery of transparent tissues.

1.1.2 Multiphoton Imaging

Confocal microscopy is historically the most democratized imaging technique. It often relies on fluorescence. Markers are introduced into the medium, and an optical signal is absorbed by these markers, which then emit light at a shorter wavelength.

Multiphoton absorption is similar in this regard to confocal microscopy, with the difference being that instead of a single photon absorption event bringing the electron from the ground state to the excited state, multiple photons are absorbed. Consequently, the wavelength of photons is at least two times higher than the wavelength associated with the fluorescent marker, yielding a lower scattering effect.

What's more is that the absorption is not proportional to the intensity but to the intensity power of n. In the case of two photon absorption this is intensity square:

$$I_{2P} \propto I_S^2 \tag{1.3}$$

The direct consequence of this is that the multiphoton-absorption will take place in a more localised section of the medium -as illustrated Figure 1.4. The layers imaged by multiphoton

are therefore thinner, as the parasitic contribution of out of focus areas are lower and the transverse resolution is higher than confocal's.

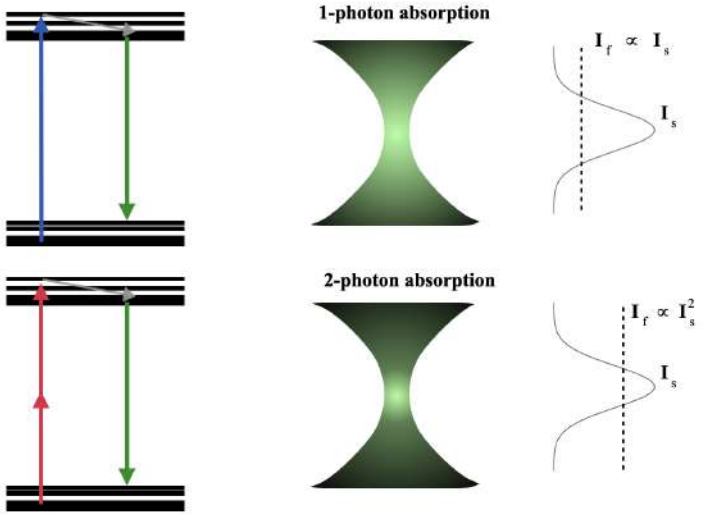

Figure 1.4 Illustration of Multi-photon microscopy and 1-photon microscopy (present case 2 photon microscopy)). Because of the proportionality between the fluorescence emission irradiance and the initial irradiance square the area where the fluorescence takes place is more limited.

Yet this low cross-section, coupled with the coherent condition of multiphoton absorption, means high powers must be reached, to levels that would lead to irreversible photodamage -as detailed previously-, should it be imposed on the medium for too long. To prevent this and ensure coherence as well, pulse's Full Width Half Maximum (FWHM) is set at 10^{-13}-10^{-14}s and the power amplified to reach 10^0 W on average.

Selection of Wavelength Another aspect that needs to be carefully evaluated is the central wavelength of the input pulse. To do so, there are two main aspects to take into account: the fluorophores -and their associated wavelength- along with the properties of the tissue, more precisely the absorption and scattering effects. Scattering effects have been briefly described in the previous section to be proportional to $\frac{1}{\lambda^4}$ and as such smaller wavelength are more prone to scattering of light, leading to a lower signal to noise ratio. Figure 1.5 is the absorption relative to the wavelength. From this diagram, a window of minimal absorption -the therapeutic window- is easily evaluated between 400 nm up to 1200nm. Given the typical wavelength of the fluorophores and the absorption properties of biological samples, two photon absorption usually takes place at 1200-1300nm while three photon absorption is tailored around 1600-1700 nm.

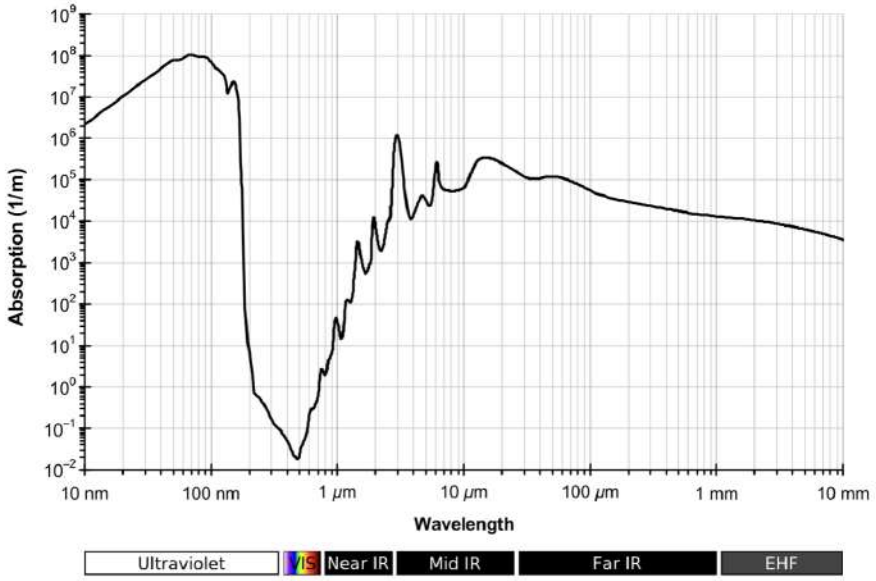

Figure 1.5 Water absorption relative to the wavelength. The data is attributed to Kebes and, under This file is licensed under the Creative Commons Attribution-Share Alike 3.0 Unported license [3].

Pulse duration and repetition frequency Because of the properties of multiphoton absorption, . This means the light beam power follows the equation:

$$P_{peak} = \frac{P_{av}}{f_{rep} . \tau_{FWHM}} \tag{1.4}$$

With P_{peak} the peak power of the pulse, P_{av} the average power of the light, f_{rep} the repetition frequency of the signal and finally τ_{FWHM} the full width at half maximum duration of the pulse. High repetition rate allow to scan matter at the expense of potential photothermal damage. What's more is at identical average power, high repetition rate yields a lower peak power. Determining the repetition rate is therefore an equilibrium between the need for more periodic measurement while yielding a high peak power and letting the tissue time to recover from thermal deposition. As of 2020, 1 MHz have been demonstrated to yield equivalent signal to noise ratio than of 80 MHz [6].

Wavefront tailoring another aspect to take into account is the shape of the wavefront as it affects the spatial resolution of the microscope. Customized beam have been extentively studied [7] by modulation of the amplitude, phase, and polarization to improve resolution and signal to noise performances, while [8] reported the use of multimod signal in order to improve the transverse resolution.

1.1.3 Optical amplification

Optical Amplification is based on population inversion between two energy levels -whether it be valance bands, atomic levels or virtual states. This is illustrated by Fig. 1.7. A pump power -in blue- is absorbed, bringing electrons from the ground level to an exited level. From this, a non radiative de-excitation to a lower level takes place -in blue doted lines. An optical signal -the pump- is absorbed by the medium, depleting the level 1 in favor of level 3. From this, two cases of figure:

1. In the case of spontaneous emission, the electron is brought back to level one, a photon is emitted.

2. In the case of stimulated emission, it is the incoming photon which triggers the transition from level 2 to 1. As a result, the emitted photon and the initial photon have the same phase.

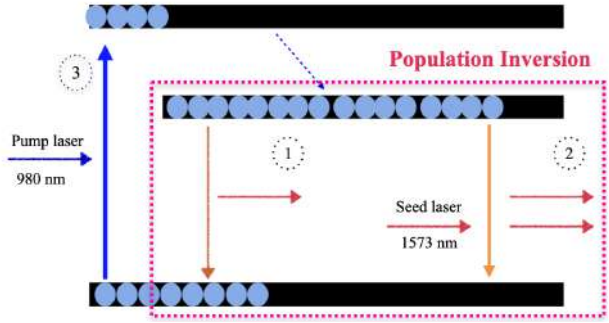

Figure 1.6 Amplification through population inversion. In dark blue the transitions associated to the pump power and in red the transitions associated to the signal.

The ideal amplification medium is a medium in which the non radiative transition is short in comparison c to the upper-state lifetime, effectively allowing for a build up of population inversion. This way, at the equilibrium, the population of the second level is higher than the population at ground level. Stimulated emission is therefore favored and the signal amplified.

The amplification of a signal is a delicate matter, directly linked to the length, the pump power but also the signal's power (this aspect is studied in chapter 5). Given this, there is a notable difference between continuous wave and pulsed light: given the FWHM at play, light-propagation in the medium is expected to generate non-linear effects.

1.1.4 Ultrafast Photonic and non-linear effects

In the case of ultrafast photonic, the master equation dictating the optical signal's propagation is the non-linear Schrödinger Equation:

$$\frac{\partial A}{\partial z} + \frac{\alpha}{2}A + \frac{i\beta_2}{2}\frac{\partial^2 A}{\partial T^2} - \frac{\beta_3}{6}\frac{\partial^3 A}{\partial T^3} = i\gamma\left(|A|^2 A + \frac{i}{\omega_0}\frac{\partial}{\partial T}(|A|^2 A) - T_R A\frac{\partial |A|^2}{\partial T}\right)$$

Figure 1.7 non-linear Schrödinger equation, in this form, the Raman effect was simplified and the associated integral reduced to a constant over the pulse bandwidth.

where:

1. α is the absorption coefficient
2. β_2 is the second order dispersion, also called the Group Velocity dispersion.
3. β_3 is third order dispersion constant.
4. γ is the non-linear coefficient.
5. ω_o is the central pulsation of the pulse
6. T_R is the Raman constant
7. z and T are respectively the normalised variable in space and time.

non-linear terms are proportional to the absolute value of the amplitude, meaning the higher the power, the smaller the characteristic length of the associated non-linear phenomena are. The peak power can be approximated by the equation:

$$P_{peak} \sim \frac{P_{av}}{f_{ceo}.\tau} \tag{1.5}$$

with f_{rep} the repetition rate of the laser source. Given the dependency to the pulse duration, for a given average power, the peak power of a 100 fs pulse will be 10^3 higher than a peak power of 100 picosecond pulse. The length upon which it is possible to discard non-linear effects is smaller for femtosecond pulse than picosecond pulses. As it is, this imposes a limit to femtosecond amplification as it limits the length of the amplification medium -on which the gain is highly dependent. Should the signal be amplified over a long amplification medium

anyway, the output's peak power won't be as high as the ideal case. Figure 1.8 illustrates the evolution of the pulse spectrum in two cases:

1. When the refractive index's dependence on the intensity becomes significant:

$$n(I) = n_0 + n_2.I$$

   This is called the Kerr effect and, when combined to the second dispersion. In the case of anomalous dispersion, this leads to the formation of optical soliton.

2. Raman effect, which is the consequence of the interaction with the medium vibrational and virtual states, hence resulting in either a smaller wavelength -Stokes Raman Scattering- or a higher one -Anti-Stokes Scattering.

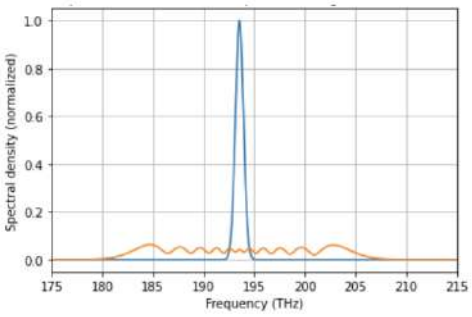

(a) Self Phase modulation (SPM) effect, in blue the initial spectrum, in orange the spectrum after a propagation in a 10cm non-linear fiber.

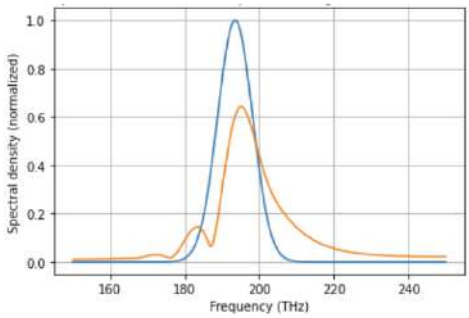

(b) Raman, in blue the initial pulse spectrum, in orange the spectrum after propagation in a 1 m non-linear fiber -SPM was discard in order to illustrate the Raman effect.

Figure 1.8 Illustration of non-linear effects. The pulse is a 100-fs with a peak power at 100mW. The figures were obtained through the implementation of a classic Split-Step Fourier Method

In any cases, non-linear effects transfer power amplification to other wavelengths than the signal's bandwidth, as well as modify the profile of the pulse. Therefore to reach the peak power needed to achieve multiphoton absorption, the pulse must be modified beforehand.

1.2 Research Objectives

This work's main goal is to design an optical source with characteristics compatible to multiphoton microscopy. To this end, an initial femtosecond source set at 100 fs, with a frequency

rate of 100 MHz and initial power of 100 mW is amplified to reach 4 W of average power. This is achieved in two steps.

1.2.1 Objective 1

The first objective is to design and implement an effective stretcher/compressor system which stretch the pulse to prevent non-linear effects in the amplification and then compress it to retrieve the initial pulse profile. The system aims to compensate for dispersion effects and optimize signal quality for subsequent amplification. Numerous setups are considered, all optics are selected to fit the requirements and finally aberrations and a slight off-balance of the stretcher-compressor are introduced to compensate dispersion taking place in the fiber.

1.2.2 Objective 2

The second objective is to design a suitable amplifier for the generated optical pulses. This involves implementing numerical simulations to evaluate the amplifier's performance in steady-state, which is then used to implement a time dependant model of the amplification. Numerical results are then compared to experimentation.

1.3 Thesis outline

This thesis is structured in three sections. Initially a comprehensive review of the existing literature lays the foundation of general concepts and the different optimizations developed over the past few years.The goal of this section is to provide relevant theories, methodologies and provide a comprehensive understanding of the historical context and current state-of-the-art.

Following the literature review, the focus shifts toward the stretcher/compressor. A detailed examination of chirp generation in pulse is used as a base for designing both setups. To this end, three structures are considered and compared to reach a system yielding a chirped signal without impacting either the bandwidth or the temporal profile of the final output pulse. The outcome is installment of the stretcher and compressor.

Lastly focus is directed toward the design of the optical amplification through an EYDFA. Doped fiber amplifiers are intricate systems that require careful balancing as they can generate counter intuitive signals. To address this issue, numerical studies in steady state are conducted on erbium-ytterbium doped fibers. These results serve as a foundation for esti-

mating pulsed amplification. Finally, Amplified Spontaneous Emission (ASE) generation is discussed and experimental data are compared to numerical results.

CHAPTER 2 LITERATURE REVIEW

With the democratization of MultiPhoton Microscopy comes the need for ultrafast high power lasers. The development of such sources comes with its set of hurdles as non linear behaviour arises from short pulse with high peak power. These setbacks were solved in 1985 with the development of Chirped Pulse Amplification (CPA) [9], which earned them the 2018 Physic Nobel Price . In this chapter, the two aspects of CPA are reviewed: optical amplification and pulse stretch/compression.

2.1 Optical amplifiers

Light Amplification was first studied and theorized in the 60s (Schawlow and Townes, 1958) which led to the emergence of various approaches: Semiconductor Optical Amplifier (SOA), Raman Stimulated Scattering Amplifier (RSS) and Doped Fiber Amplifer (DFA).

Light amplification are all based on population inversion, whether it be between two atomic energy levels (DFAs), two electronic bands (the valence and conduction band for SOA), or virtual states and vibrational states (RSS). Each amplifier's type has their advantages and inconveniences : RSS generate lower noise but require higher power pump to generate 20 dB gain, while SOA's gain are reported to be higher, the trade-off being a higher noise level.

DFAs have become the most common light amplifiers due to their properties and extensive research. Indeed rare earth luminescence has been under study since the beginning of the twentieth century, which laid grounds for the study of rare earth doped fiber. Over time many active dopants have been considered, from Europium [10], Ytterbium [11], and finally Erbium [12]. Erbium Doped Fibers Amplifiers (EDFA) have been the subject of extensive studies [13] as erbium enables gain in the C- and L-band (1530–1565 nm and 1565 nm to 1625 nm respectively), two bands of interest in telecommunications. A first theoretical approach on Erbium Doped fiber was published in 1991 [14] and paved the way for EDFA commercialisation (1992).

Over the past thirty years, EDFA designs have been improved following two directions: increasing the fiber's amplification capacity by raising the erbium concentration and tuning the design to the desired gain. Strategies such as pumping the fiber in a forward and backward configurations have been experimentally studied [15], along with increasing the number

of passes made in the fiber [12].
While such designs increase the gain, they tend to raise the contribution of the Amplified Spontaneous Emission (ASE) [16] and Stimulated Brillouin Scattering, and so raising the Noise Figure (NF) of the beam [17]. As for the concentration of erbium dopant, it is mainly limited by the quenching phenomena -Erbium ions forming pairs and raising the global ASE contribution while lowering the luminescence of the system. As such EDFAs with typical noise figure of 3 to 5 dB have been reported to yield gain from 20 to 40dB -depending on the structure of the amplifier.

Doping Erbium Doped Fiber (EDF) with another ion has become the most democratized solution for amplifying a signal above 40dB without increasing the Noise Figure. To this end, ytterbium ion are the go-to choice, and as of today, different configurations have achieved a gain of 45 dB in the C-band [18] while S.Z. Muhd-Yasssin et al. reported a gain of 56dB with a noise figure under 5dB [19], though this value was reached through co-doping along with a combined architecture of DFA and Raman Stimulated Scattering Amplifier. When it comes to simulations, EYDFA's models in steady states have been implemented [20], [21].

2.2 Stretcher-Compressor

With ultrafast photonics comes the following conundrum: amplifying a short pulse, and as such, reaching a Peak Power likely to generate non linear effects in the amplifier. This hindered the development of pulsed laser and as such pulse peak power stagnated under the gigawatt mark until the first CPA setup was designed by the Rochester group (Strickland 1985), producing a 2 ps pulse with a millijoule energy at 800nm central wavelength. Chirped Pulse Amplification consists of stretching the pulse before entering the optical fiber and re-compressing it afterwards. This way, while the input energy remains the same, the Peak Power is significantly lowered in the fiber and non linear effects are prevented. The first CPA setup considered of a pair of parallel gratings, first presented by Treacy in 1969 [22] inducing a negative Group Delay Dispersion (GDD) acting as a pulse compressor along with a positive group delay dispersion fiber acting as a stretcher. CPA opened a new area of pulsed laser development, with zettawatt-equivalent lasers being currently under development [23].

While the first CPA setup enabled to effectively increase the peak power by a factor 100, the missmatched between the stretcher and the compressor led to third order deformation of the output pulse. From this point, the field has been divided on the approach to adopt: either compensate the high orders missmatch post-amplification or searching for the ideal

stretcher/compressor pair. Considering the later, the equivalent stretcher of the Treacy grating pair was widely investigated and found in 1987 by Martinez [24].

With the increase of stretch ratio coefficient from thousands to hundred of thousands [25] arose another issue regarding the free-space CPA: optical aberrations. As such the focus of stretcher/compressor shifted from the ideal match to the design of aberration-free stretcher and compressor [26]. Such designs were investigated until methodology to suppress optical missmatch and obtain ideal setup up were found [25] (This will be developed in a dedicated section).

While free space stretcher/compressor design allow for perfect match and suppression of optical aberration, the size of the required optics along with their position is all the more significant as the signal's bandwidth. As such great focus was put on reducing the required size of the setup by investigating compact versions of existing designs [27].

With the generation of shorter pulses, the dispersion taking place in the fiber becomes significant. To ensure the conservation of the input profile this effect must be properly compensated, and so included in the design of the stretcher/compressor. The focus shifted once more from ideal compensation between the two ideal setup to investigate methods to compensate higher order in the fiber. To this day, robust methodologies enabling the perfect match between aberration free set up, to the third order dispersion have been investigated [28]. Suppressing fourth and fifth order has become necessary as pulse amplification has reached sub-100 fs pulses. To do so, acousto-optic temporal phase correction have been introduced [29], along with the use of optical aberrations [30], [31] to generate the needed missmatch and compensate fiber dispersion up to order 4 for a 40 fs pulse at central wavelength 800 nm.

CHAPTER 3 STRETCHER AND COMPRESSOR DESIGN

The development of laser source has always been driven by the aim of generating shorter pulse at higher peak power, whether it be for non-linear imaging, telecommunication or the study of matter. This development has been far from linear. Indeed, with the shortening of pulses and the increase of average power came the uncontrolled generation of non linear effects. These effects have hindered the development of laser source as they not only modify the spectral bandwidth of the beam but also effectively put a limit to the maximum peak power (non linear effects are described in length in the Chapter Pulse Amplification). In effect, the pulse duration was limited to 100 ps until a solution was developed by Donna Strickland (1985): Chirped Pulse Amplification (CPA) [9] , which consists of introducing a spectral phase in order to modify the temporal profile of the pulse and as such effectively lower the peak power. With this method, amplifying pulses shorter than 1 ps has become possible in doped-fiber.

Over the past forty years, CPA has been perfected to impose a better control on the chirping and the quality of the output beam. The stretching of a pulse and the reverse operation is a delicate operation, especially in free space, as it involves diffracting optics and as such introduce very easily high order spectral phase, aberration and bandwidth clipping.

This chapter is centered around the stretcher and the compressor. After a summary of the theory of pulse chirping, the focus is set on the design of both set ups, from the parameters to the optics characteristics. While in practice the process is iterative, the selection of the grating, the configuration and the residual phase will be studied separately. Finally, the system's precision requirement and the experimental results will be presented.

3.1 General Theory of Pulse Chirp

A pulse is qualified as chirped when the instantaneous frequency is not constant across the duration of the pulse. The pulse can acquire a chirp -and so a non monotonous instantaneous frequency- while propagating in a medium in which the chromatic dispersion, non linear effects or refractive index variation over the bandwidth are significant enough over the propagation length. As such it is often observed when pulses are short enough -and so pulse spectrum wide enough- for a significant difference to take place between the maximum and minimum frequency.

This section develops the two main aspects of chirp-pulse theory: the conventions along with the exact mathematical development and consequences it generates.

3.1.1 Definition and conventions

As stated before, a chirp is a variation of frequency across the pulse and the consequence of a phase acquired during propagation. This phase is either temporal or spectral, depending on which profile is to be modified.

Temporal chirp

Given the previous definition, a temporal chirp is the variation of the frequency relative to time and the application of a temporal phase. A gaussian-shaped pulse is taken as example to illustrate the principles and properties. The electrical field is given the expression:

$$E(t) = E_o.e^{-a.t^2}.e^{2.\pi.i.\nu_o.t} \tag{3.1}$$

With:

1. Amplitude of E_o.
2. A gaussian shaped profile of constant a.
3. A central frequency of ν_o and the angular frequency $\omega_o = \nu_o/2\pi$

A chirp arises from the application of a phase to the pulse. In this context, a phase function $\phi(t)$:

$$E(t) = E_o.e^{-a.t^2}.e^{i\omega_o.t+i.\phi(t)} \tag{3.2}$$

While the intensity is not modified, the application of a phase impacts the beam, more precisely the instantaneous frequency. To evaluate to what extent, the pulse duration is considered to be short enough so that the phase can be approximated by a Taylor development:

$$\phi(t) = \sum_{n=0}^{\infty} \frac{P^{(n)}(0)}{n!}.(t)^n \tag{3.3}$$

The constant term and the first order of this development can be disregarded through a change of variable (leading to respectively a temporal shift and a frequential shift, both constant):

$$\phi(t) = \sum_{n=2}^{\infty} \frac{P^{(n)}(0)}{n!}.(t)^n \tag{3.4}$$

Which can be re-arranged as:

$$\phi(t) = (\sum_{n=2}^{\infty} \frac{P^{(n)}(0)}{n!}.(t)^{n-1}).t = b(t).t \tag{3.5}$$

It is therefore possible to express the electrical field as:

$$E(t) = E_o.e^{-a.t^2}.e^{i.(\omega_o - b(t)).t} \tag{3.6}$$

This expression introduces the notion of a an instantaneous frequency:

$$\nu(t) = \nu_o + 2.\pi.b(t) \tag{3.7}$$

The perceived frequency is not constant for the duration of the pulse and as such will impact the pulse spectrum. While one could in theory design a non-monotonous b function, in practice, b(t) is considered either increasing (up-chirp) or decreasing (down-chirp).

Applying such phase in order to modify the pulse spectrum is a well-developed technique and is one of the point of focus in the generation of ultrashort pulse. Quadratic temporal phase modulation can be used to successfully generate femtosecond pulses from continuous lasers [32], though the translation of a quadratic temporal phase to a quadratic spectral phase is never perfect and leads to aberration [33].

Frequency domain

Given the reverse properties of the Fourier Transform, the previous development can be applied all the same in spectral domain:

$$\phi(\nu) = \sum_{n=0}^{\infty} \frac{P^{(n)}(\nu_o)}{n!}.(\nu - \nu_o)^n$$

Similar conclusions emerge, such as unchanged spectral power density and modulated intensity, given the introduction of:

$$t(\nu) = t_o + 2.\pi.b(\nu) \tag{3.8}$$

The perceived time becomes dependant on the mode and behaves differently in time domain. Modes undergo reorganization, resulting in a non-constant instantaneous frequency over time.

The introduction of spectral phase is at the core of pulse amplification. This section provides a detailed description of the variations one can achieve through this method.

3.1.2 Mathematical development and pulse modulation

Introducing a phase in one domain lead to a modulation of the square amplitude in the reciprocal domain -providing a careful tailoring of the applied phase. It is therefore crucial to establish the various families of spectral phases and the properties they impart on the intensity. Given the objective of amplifying the beam without altering its spectrum, the focus will be on introducing spectral phase. Consequently, the subsequent mathematical development will be conducted in this domain. It should be noted that similar conclusions can be drawn when conducting this study in the time-domain.

To this extent, a gaussian shaped pulse is taken as a base, upon which a spectral phase function is applied to:

$$E(\nu) = E_o.e^{-a^2.\nu^2+i.\phi(\nu)} \tag{3.9}$$

with

$$a = \frac{1}{2.\sigma_t} \tag{3.10}$$

The pulse bandwidth is assumed to be narrow compared to the variation of the phase so that the function $\phi(\nu)$ can be approximated by its Taylor development:

$$\phi(\nu) = \sum_{n=0}^{\infty} \frac{P^{(n)}(\nu_o)}{n!}.(\nu - \nu_o)^n$$

With this mathematical description of the phase function, terms can be studied separately:

1. Constant term ϕ_o: by definition of the Fourier Transform operation, a constant term in frequency domain leads to the same constant in time domain. Because of this, a constant phase won't lead to any modulation of the profile. From this point, the constant term is considered null.

2. Linear term ϕ_1: the spectral phase term being in the shape of $\phi_1 = b_1.(\nu - \nu_o)$, it leads to a translation in time and in a similar fashion as the constant term, a simple change of variables suppresses the term from the phase expression.

3. Terms of 2 and higher order: Even terms affects evenly the frequencies ($\nu_o - \nu$, $\nu_o + \nu$) and as such the symmetry of the pulse is preserved, unlike odd terms. For this reason,

even and odd orders are studied separately.

Even orders

Because of the symmetry relative to the central frequency of the beam, even orders don't breach the symmetry of the pulse. In this case, the focus lies on the quadratic term for two reasons: first the higher the order of a term, the less significant its effect, then A quadratic spectral phase, being a Gaussian function, maintains symmetry (provided that the initial shape of the beam is compatible with the axis of symmetry of a Gaussian function, such as a constant beam or a Gaussian beam [33]). In practice, a quadratic phase is commonly utilized as it allows for tuning the pulse full width at half maximum (FWHM) without introducing temporal aberrations.

To evaluate the variation in FWHM caused by a quadratic phase, let's examine a Gaussian pulse with a quadratic phase:

$$E(\nu) = E_o.e^{-a^2.(\nu-\nu_o)^2+i.b.(\nu-\nu_o)^2} \tag{3.11}$$

where

$$a = \frac{1}{2.\sigma_t}$$

A small rearrangement leads to:

$$E(\nu) = \frac{E_o}{\sqrt{a}}.e^{-(a^2+ib).(\nu-\nu_o)^2} \tag{3.12}$$

which leads to:

$$E(t) = \frac{E_o}{\sqrt{a-ib}}.e^{-\frac{t^2}{4.(\sigma_{tp}^2)}} \tag{3.13}$$

with

$$\sigma_{tp}^2 = \frac{1}{a^2+ib_2}$$

Given this, the intensity is given by:

$$I(t) = I_o.e^{-\frac{(t-t_o)^2}{(2.\sigma')^2}} \tag{3.14}$$

and the standard deviation:

$$\sigma' = \sqrt{\sigma^2 + \frac{b^2}{\sigma^2}} \tag{3.15}$$

From this expression, it becomes clear that applying a quadratic spectral phase to a gaussian

pulse does not break the gaussian symmetry. Moreover, for a given spectrum, the shortest pulse duration is achieved in the absence of chirp, which is equivalent to a constant instantaneous frequency and constant spectral phase.

Note: Higher order introduce a breach of the gaussian symmetry for limited contribution of to the pulse stretching.

Odd orders

Given the expression of odd orders, a breach of symmetry is expected, leading a a deformation of the pulse in time-domain. For this reason, odd orders, -third order most than all- are often avoided/compensated.

Applying a spectral phase function to a beam allows to modify the shape of the pulse in temporal phase without modifying the pulse spectrum. In the case of a gaussian pulse, even orders broaden the pulse while odd orders break the symmetry. This process is reversible by applying the opposite phase function. The pulse can therefore be stretched and as such, the peak power being lowered, in a reversible process, paving the way to amplification without any undesirable non linear effects.

3.1.3 Return to physics

As it has been established, pulse-chirping allows for a modification of the temporal profile of the pulse without any filtering. What's more is that it is in theory possible to apply the opposite phase at the output of the amplification fiber to retrieve the initial profile of the pulse. A quadratic spectral phase is typically generated when it comes to CPA, as its symmetry does not compromise the symmetry of the -generally- gaussian pulse. As such pulse-chirped amplification allows for amplification of pulses shorter than 1 ps to energy as high as 1 mJ . The main focus is now to design a set up that will introduce a quadratic spectral phase Φ and its opposite $-\Phi$. To this date, there are two main options:

- Chirped Fiber Bragg grating: this consists of a fiber with a periodic modification of the refractive index of the core. This variation introduces reflection, depending on the wavelength and as such a variation on the effective optical path.
- Diffraction Grating being the equivalent in free space: the periodicity of the grating leads to a refracted/reflected angle dependant on the incoming wavelength.

Free space stretcher/compressor are quite delicate to design as they introduce a great number of free parameters. However it is this great flexibility of the design that makes them appealing. Indeed, when generating a chirp, whether it be free space or in a medium, high orders are bound to be generated. A pure quadratic phase can only be generated at great expense. Whether the high orders must be taken into account depends on the signal.

Table 3.1 Pulse characteristic of the seed laser source (NKT Photonics)

parameter	τ_{FWHM}	f_{rep}	P_s	λ_0	$\Delta\lambda$
value	100 fs	100 MHz	100 mW	1573.3nm	38.9 nm

Table 3.1 is a summary of the pulse characteristics. Given the pulse duration and bandwidth, the impact of high orders is expected to significantly impact the pulse shape. If a fiber was to be used, high orders would need to be compensated by an additional setup. On the other hand free space stretcher/compressors' great number of parameters offer the possibility to counteract these effect within the initial setup. For this reason the free space option was preferred in this work.

3.2 Theory of Pulse Chirp in Free Space

The mathematical principles and the method of pulse stretch/compression been established, it's time to dive in the theory of free space pulse chirping. As mentioned before, this is achieved through a diffracting component: an optical grating. This section is focused on the different types of gratings available, the principle of light diffraction and the mathematical description of the chirp in free space.

3.2.1 A brief review on gratings

Applying a chirp in a pulse is no easy task, as it is necessary to introduce a difference in optical path dependent on the wavelength. In free space, this is achieved through a grating and as one can expect in such case, the properties of the optics will determine the limits on power along with the chirp and the bandwidth of the input pulse. As such gratings have been thoroughly studied and related technologies improved to fit precise applications. As of today three main types of gratings have been developed.

The oldest type is the Metallic Grating -Au-coated [34] . Indeed it allows for a high bandwidth, up to 100 nm and can be easily found for a wide variety of central wavelength. This

flexibility in terms of wavelength, a wide bandwidth based on more than three decades of development contributes to making this type of grating the most widely used technology when it comes to chirping a pulse. However the downsides remain significant: metallic gratings tend to have 'high' energy absorption. This leads to relatively low transmission/reflection coefficient (ranging from 85% to 95% on average) and a lower Laser Induced Damage Threshold (LIDT). While a transmission coefficient of 85% can at first sight appear reasonable, it must be put into perspective as beams interact with grating at the very least 4 times, and so a 85% transmission lowers the global efficiency to $(0.85)^4 = 52\%$ -without taking into account the other optics, and so these relatively low transmission coefficient lead to significant power loss.

To improve the efficiency of the chirping setup, Multilayer Dielectric Gratings (MDG) have been developed. The main advantage of using a dielectric material is that is absorbs significantly less than a metal and as such both the transmission coefficient along with the LIDT are higher. Coefficient can reach as high as 98% for the first order. However these gains have been achieved in detriment to the possible bandwidth. Because of this, MDG are more commonly used for picosecond signals.

The ideal case would be a grating allowing for a high bandwidth while limiting undesirable absorption. To this end a new type of grating is being developed: The Metallic Multilayer Dielectric Grating (MMDG). This new type of grating is currently under development and study, and while wavelength compatibility is as of today quite limited to 1000nm, promising results have been published regarding bandwidth and transmission coefficient.

3.2.2 Grating Diffraction Theory

With the types of grating reviewed, this section presents the main basis of grating theory and angular selection.

A diffraction grating -also calling optical grating- is an optical component which separate light in space according to its wavelength. This is achieved through a periodic surface as showed Fig 3.1. In that case, the refracted angle follows the equation:

$$\theta_c = \arcsin\left(\frac{m.\lambda}{d_g} - \sin\theta_i\right) \tag{3.16}$$

where:

1. m is the order of diffraction (dimensionless). For m=0, the grating acts as a mirror,

otherwise the angle is dependant on the wavelength.

2. λ is the wavelength in meter.

3. d_g is the grating step in meter, inversely proportional to the line density.

4. θ_i is the angle of incidence of the beam.

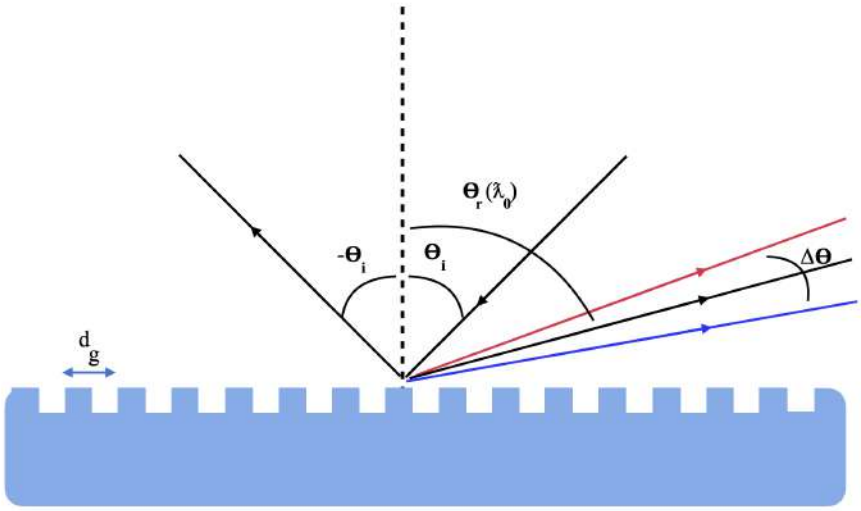

Figure 3.1 Dispersion of light under a reflecting grating. By convention, diffraction orders on the same side of the incident light are negative. In this case, only the order -1 is represented, along with the order 0 (pure reflection without diffraction).

Note: In practice a specific surface structure is used called blazed gratings. These gratings' surface are not symmetric which selects a specific order of diffraction. The other orders are extinguished and power leakage is prevented. Gratings in this case also select a polarization -in this case the Transverse Magnetic mode (TM-1).

The most important parameter to select is the line density, as it determines the maximum angular variation the grating imposes on a given bandwidth. In practice, the line density is selected through an iterative process, in parallel to the design of the stretcher and the compressor as other parameters must be taken into account -mainly the angle of incidence, high order residual phase. For clarity's sake, all parameters other than the grating properties, are set to their final values.

The angular variation is at the core of the design of CPA, as it is the difference of angle between the lower and higher wavelength, effectively determining the difference of optical path within the bandwidth, and so the chirp. The higher the angular variation, the bigger the chirp. What's more is the line density determines the maximum wavelength refracted by the grating, and above which all signal will be reflected back to order 0:

$$\lambda_{cut-off} = \frac{d_g}{m}.(1 + \sin(\theta_i)) \tag{3.17}$$

The wavelength cut-off is one of the main criteria to be taken into account while selecting the grating line density and incident angle as it determines whether a portion of the spectrum will be filtered out of the setup.

3.2.3 Grating Chirp Generation

When it comes to CPA, the main goal is to prevent any modification of the pulse shape between the input and the output through non linear effects. Therefore balancing spectral phases of the stretcher, the compressor along with the material dispersion is one of the main concerns of ultrafast amplification. Designs of stretchers/compressor have been thoroughly studied in the 1970s, from which the Martinez stretcher/compressor (1967), the Treacy compressor (1969), Banks (1970) and the Offner setup(1971) are derived. While the setup allow to tune the spectral phase to a target value, perfect matching is not always achieved. Higher order can lead to slight change in the stretcher/compressor ratio. The remaining spectral phase can be minimized, up to the order 5 [35], otherwise higher-order corrections must be implemented, like acousto-optic time phase corrector [36].

Designing a compressor/stretcher pair requires balancing the power absorption of the gratings and optics, generating the target GDD value while limiting the higher order phase. The condition to generate an output signal identical from the input is:

$$\phi_{stretcher}(\omega) + \phi_{compressor}(\omega) + \phi_{materials}(\omega) = 0 \tag{3.18}$$

It is paramount to determine the GDD and high order generated in all components (the term associated with the material is studied in Chapter 4). A pulse entering a stretcher setup or a compressor follows the equation [37]:

$$\frac{\partial A}{\partial z} - \frac{i.\beta_2}{2}.\frac{\partial^2 A}{\partial t^2} - \frac{\beta_3}{6}.\frac{\partial^3 A}{\partial t^3} + \frac{i.\beta_4}{24}.\frac{\partial^4 A}{\partial t^4} = 0 \tag{3.19}$$

where the coefficients β_2, β_3, β_4 are respectively the Group Delay Dispersion (GVD), the Third Order Dispersion (TOD) and the Fourth Order dispersion (FOD):

- $$\beta \frac{2.\pi}{\lambda} \tag{3.20}$$
- $$\beta_2 = \frac{\partial^2 \beta}{\partial \omega^2} \tag{3.21}$$
- $$\beta_3 = \frac{\partial^3 \beta}{\partial \omega^3} + \frac{\partial^2 \beta}{\partial \omega^2}.\frac{\partial \beta}{\partial \omega}.\frac{3}{\beta} \tag{3.22}$$
- $$\beta_4 = \frac{\partial^4 \beta}{\partial \omega^4} + \frac{\partial^2 \beta}{\partial \omega^2}.\frac{\partial \beta}{\partial \omega}.\frac{4}{\beta} + \frac{3}{\beta}.(\frac{\partial^2 \beta}{\partial \omega^2})^2 \tag{3.23}$$

The expression of these coefficient have been well studied over the past decade, leading to these expressions [38]:

- $$\beta \frac{2.\pi}{\lambda} \tag{3.24}$$
- $$\beta_2 = \frac{m^2.\lambda_o^3}{2.\pi.c^2.d^2.\cos(\theta_r)^2} \tag{3.25}$$
- $$\beta_3 = -3.\beta_2.\frac{\lambda}{2\pi c}.[1 + \frac{m.\lambda}{d}.\frac{\sin\theta_r)}{\cos(\theta_r)^2}] \tag{3.26}$$
- $$\beta_4 = -\beta_3.\frac{3\lambda^2}{4\pi^2 c^2}.[4 + 8.\frac{m.\lambda}{d}.\frac{\sin(\theta_r)}{\cos(\theta_r)^2} + \frac{\lambda^2}{d^2}.[1 + \tan(\theta_r)^2.(6 + 5\tan(\theta_r)^2)]] \tag{3.27}$$

Since the pulse propagates through an effective length L, the value of the Group Delay Dispersion is easily deduced:

$$GDD = \beta_2.L \tag{3.28}$$

Given the relation between β_2 and higher orders, all coefficient are proportional to the effective length L.

The chirp of a pulse generated by a grating is directly linked to the characteristics of the

grating, along with the incident angle and the characteristic length. The design of a CPA setup consists in optimizing all parameters to ensure the target pulse duration and so without generating residual spectral phase.

3.3 Ideal Configuration Design

In this section, the focus is first on the design of an ideal stretcher/compressor pair, meaning any dispersion occurring in the fiber is discarded -this will be tackled in the following section. This is achieved in three steps: first determining the needed pulse duration to prevent non linear effects along with the associated chirp target, then the selection of the grating, and finally the selection of the configurations for both setups along with the characteristics of all optics involved.

3.3.1 Theoretical target

Pulse stretch

First of all, the minimal chirp target preventing non linear effects in the amplification fiber must be determined. This chirp needs to be minimal, as it lowers the peak power of the pulse and so not only increases the relative noise generated in the amplification fiber but also lowers the efficiency of the pulse amplification relative to spontaneous emission -this will be discussed in details in the next chapter. Besides higher order are expected to follow the increase of chirp imposed on the beam. While higher orders will be countered without additional optics, the deformation of the pulse shape in the amplification fiber might cause exotic effects in terms of gain flatness. The minimal value is expressed as:

$$\tau_{stretch} = \frac{L_{eff}.E_{max}.\gamma}{\Delta\Phi} \tag{3.29}$$

where :

- L_{eff} is the effective length of the fiber
- E_{max} is the energy of the pulse.
- γ is the non linear constant of the fiber.
- $\Delta\Phi$ is the dephasing of a gaussian beam, estimated to 20%

Given the properties of the beam and an estimation of the characteristics of the fiber amplification setup, the minimal pulse duration is set at 317 ps.

Chirp target

As established in the first section of this chapter, the second order term is driving the pulse FWHM. The chirp is therefore estimated by applying a perfect quadratic spectral phase. The pulse duration is therefore given by the equation:

$$\tau = \delta t_o . \sqrt{1 + (4.ln(2).\frac{GDD}{\Delta t_o^2})^2} \tag{3.30}$$

As a result, the Group delay dispersion is given by:

$$GDD = \frac{\Delta t_o^2}{4.ln(2)} . \sqrt{(\frac{\Delta t}{\Delta t_o})^2 - 1} \tag{3.31}$$

Knowing the pulse characteristics and the target pulse width, the GDD is estimated at 11.44 ps^2.

Note: this expression of the pulse duration and the associated chirp does not take into account the higher order of dispersion. In the case of free space stretcher compressor third order is generated and as such the pulse shape is greatly impacted and is in effect shorter than the predicted value of 317 ps. However this shortening of the pulse target also comes with a significantly lower amplitude and as such the goal of preventing non linear effects in the fiber is still achieved.

Now that the necessary chirp is determined, it is time to select all optics involved in the stretcher/compressor setups.

3.3.2 Grating selection

As presented before, the selection of a grating relies on the characteristics of the pulse. Given the characteristics of the beam, a Metallic Au-coated grating was chosen. As detailed before, the main focus is to prevent spectrum clipping and to determine the maximal line density allowing the diffraction of the entire bandwidth. To determine this limit, the evolution of the cut-off wavelength is calculated over a large range of line density values Fig 3.2:

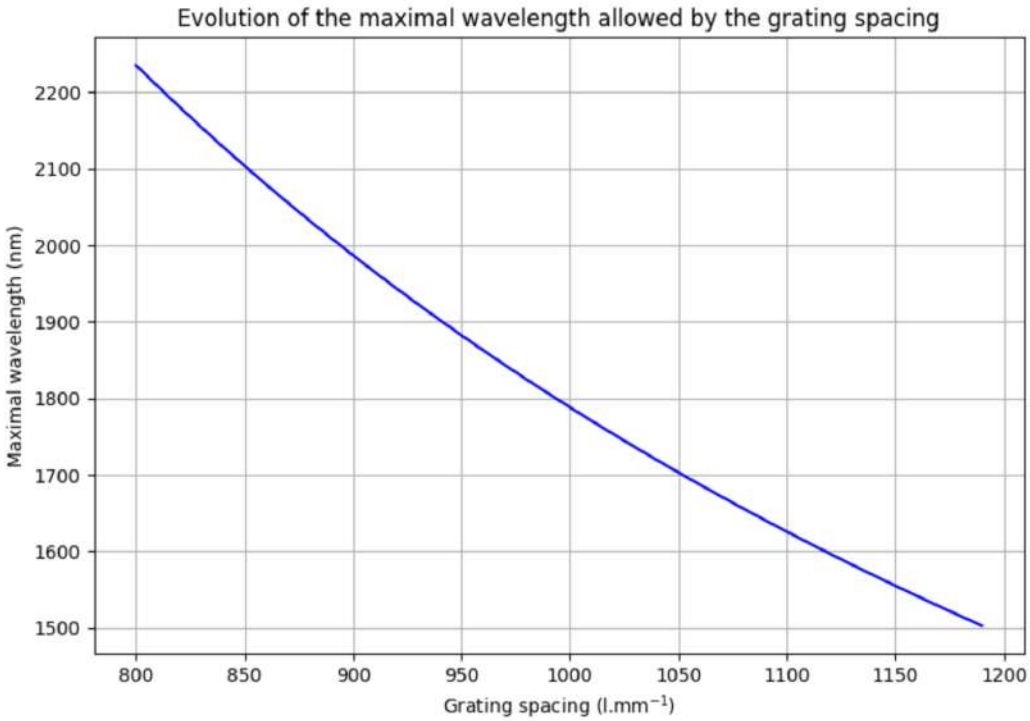

Figure 3.2 Evolution of the bandwidth cut-off imposed by the grating. The incident angle is 52°, which is the result of the iterative process of conception of both the stretcher and the compressor for the first diffraction order.

The characteristics of the pulse imposes for the line density to be under 1150 l.mm^{-1}.

Now that this limit has been determined, the focus is set back on the angular variation. To this end, the refracted angle is calculated over the interval: [1550, 1620] nm, which is larger than the bandwidth of the pulse and so prevents the possibility of unfortunate clipping:

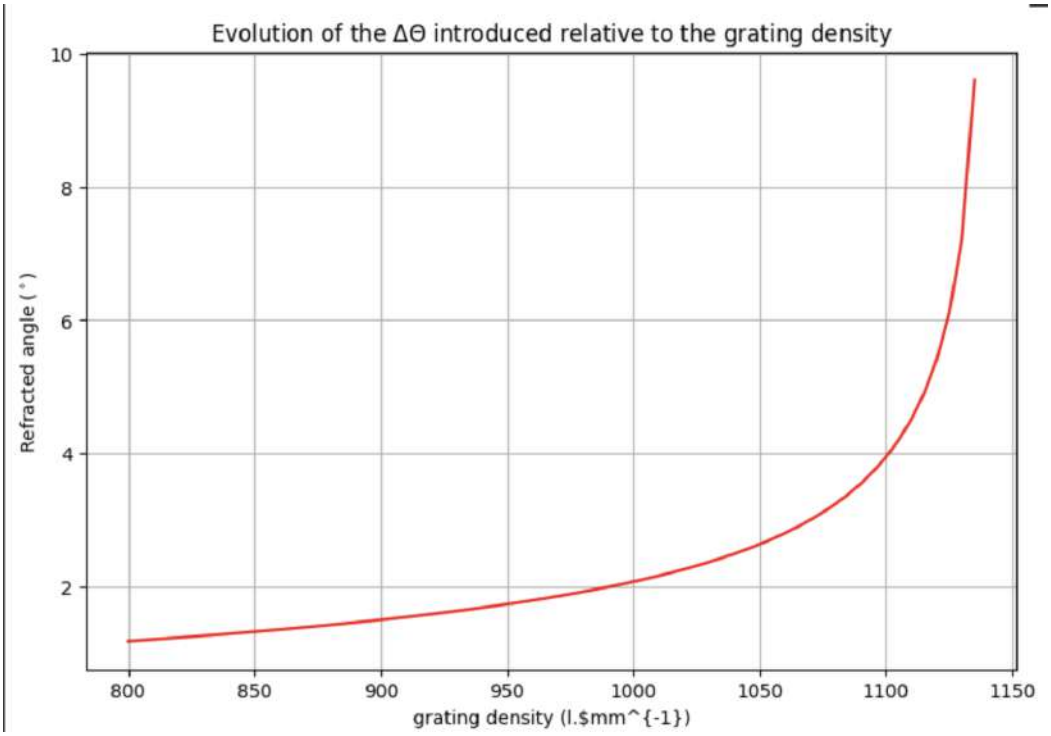

Figure 3.3 Evolution of variation of angle introduced relative to the grating spacing. The selected bandwidth is the interval [1550,1620]nm, with an incident angle of 52° -the choice value of the incident angle will be detailed later in this chapter

The higher the grating density, the higher$\Delta\theta$ is. The ideal grating being the one offering the greatest interval of possible angular variation, the grating density is selected at the point of inflection: 1100 line.mm^{-1}.

With the parameters selected, the interval in which the incident angle must be set to prevent clipping is calculated, through the extreme case of the refracted angle is 90°. Given the grating equation, the angle limit of incidence is expressed by the equation:

$$\theta_{lim} = \arcsin\left(\frac{m.\lambda}{d_g} - 1\right) \tag{3.32}$$

The results are presented in the Fig 3.4:

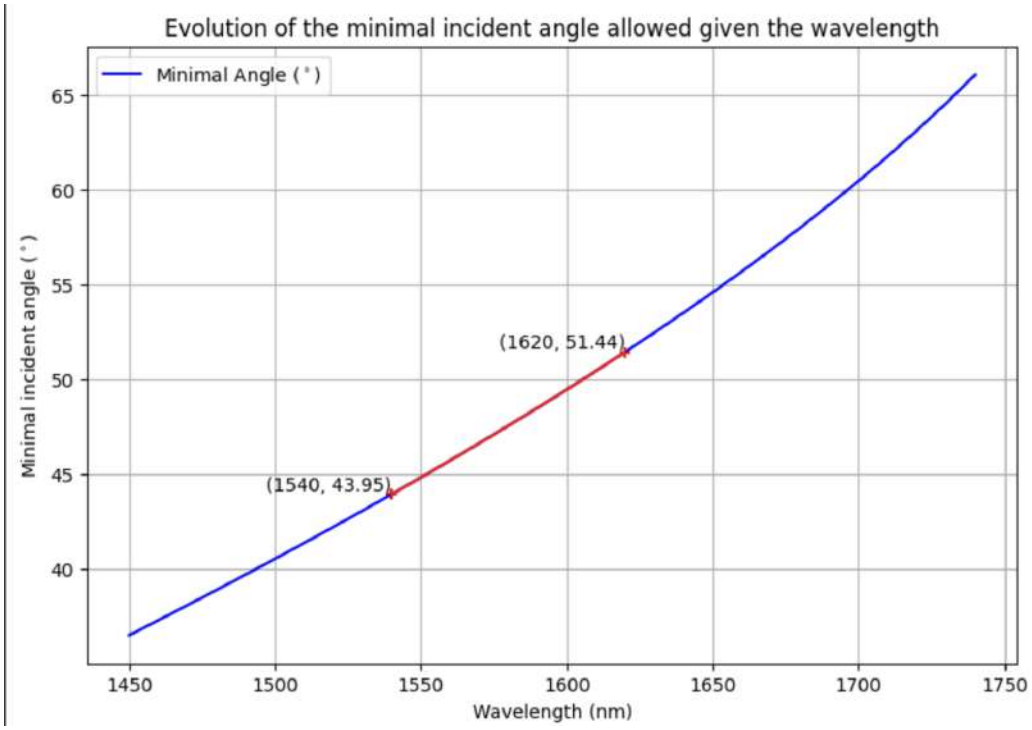

Figure 3.4 Evolution of the minimal angle allowed by the grating given the wavelength. The section is red is the area of interest: the beam has a central wavelength of 1573 nm and a bandwidth of 38.9 nm.

The limit here is imposed by the mode with the smallest wavelength. Since the pulse is centered at 1573nm with a FWHM of 38.9nm, the total $1/e^2$ halfwidth is 66 nm, leading to a wavelength of 1540-1610 nm. To prevent any clipping, the incidence angle will be selected within the interval [51.45,90].

3.3.3 Configuration study

With the main principle of chirp pair design presented previously, this section of the chapter is focused on the selection of:

1. The configuration.
2. The parameters of all optics.
3. The relative position of all optics.

Once more, it goes without saying that this selection is an iterative process and while stretcher and compressor setups are studied separately, in practice this must be done in parallel. Three

configurations are here studied: The Martinez and Offner configuration for the stretcher design, and the Treacy grating pair configuration for the compressor. Each configurations is evaluated through three criteria:

- Power Efficiency: which is the ratio between the input and output power, expected to be bellow 100% as optics are not ideal.
- Stretch ratio: which is the maximal achievable ratio between the output and input pulse duration.
- The Chirp itself, and the feasability of the configuration, determined through ABCD matrix.

Martinez configuration

When it comes to stretching a pulse in free space, the setup of reference is without a doubt the double-pair grating developed by Martinez (1967). This of course is not without reason: not only this setup allows for both positive and negative GDD, has limited optical aberrations, but it easily goes in pair with its equivalent: the Treacy compressor (1969). This setup is composed of a pair of gratings, a pair of lens along with a plane mirror to ensure the spatial recombination of the modes:

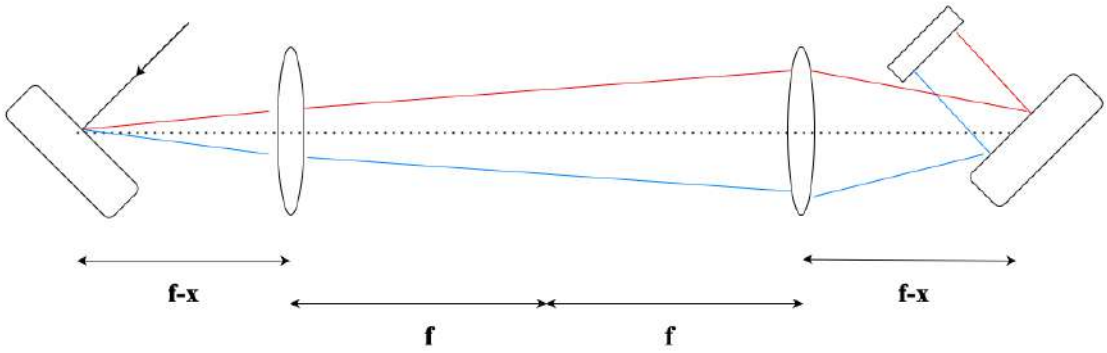

Figure 3.5 The Martinez Grating pair in its symmetric configuration (both lens are identical). Because of this, it is possible to reduce this setup's size by placing a plane mirror in the plane of focus common to both lens. While this simplifies the setup and prevent potential missmatch between the two lens and the two grating, it also leads to chromatic aberrations. f is the focal length of the lens, x is the relative position of the grating to the focal point.

One of the pros of using a pair grating is its expression of the effective path L=2(2.f-2.x), a

linear dependency, yielding the expression of Group Delay Dispersion:

$$GDD = \frac{\lambda_o^3.4.(f-x)}{2.\pi.c^2.d^2.\cos(\theta_r)^2} \tag{3.33}$$

The Martinez pair grating can therefore be used both in stretching configuration (x≥0) and in compressing configuration (x<0).

Power efficiency Given the optics, the power efficiency of this setup is given by the expression:

$$P = R_{grating}^4.T_{lens}^4.R_{Mirror1}^2.R_{Mirror2} \tag{3.34}$$

With R the reflection coefficient of the optics and T the transmission coefficient of the optic. Given the characteristics of the optics (Annex A), this efficiency is estimated at 66%.

Stretch ratio Before diving further into the selection of the parameters, it is necessary to evaluate the stretch ratio this configuration can generate. Indeed the target value of the stretched pulse is 317 ps, meaning that the duration of the 100fs pulse needs to be stretched $3.17.10^3$-fold, defining the stretch ratio of the grating compressor. To do so, the maximum ratio a Martinez setup can deliver will be evaluated: assuming the relative path to be maximum, meaning L=4f (the grating is positioned at the focal of the lens) and the maximal refracted angle (corresponding to the minimal incident angle).θ_i=51.44°):

$$\theta_{min} = \arcsin\left(\frac{m.\lambda}{d_g} - \sin(\theta_{imin})\right) \tag{3.35}$$

which yields a value of 71.11°. From this it becomes possible to calculate the maximum GDD -and so the FWHM of the beam- depending of the focal of the lens:

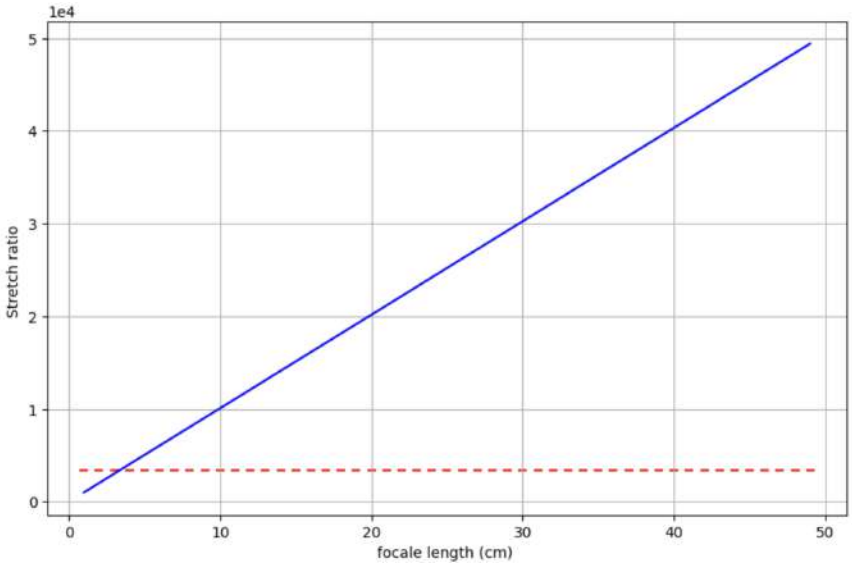

Figure 3.6 Evolution of the stretch ratio given the focal length of the lens. In blue the maximum stretch ratio the system can yield, relative to the focal length of the lens, in red the stretch ratio required by the system and so the minimum stretch ratio expected of the setup

With this result, it is possible to determine an interval for the focal length of the lens. Indeed the minimum ratio required eliminating focal lengths under 3.5cm while considering values above 40cm appears unnecessary. From now on, only focal lengths in the interval [10,40]cm will be considered -the minimum focal was tripled as safety measure.

Chirp Generation Now, whether the targeted GDD can be generated with a Martinez stretcher is determined. In the case of a Martinez configuration, three parameters need to be determined: the focal length f, the incident angle θ_i, and the position of the grating x. There are two scenarios to consider: the grating is in focus or out of focus. Ideally, being in the case where the grating is in focus is preferred as it simplifies the alignment process and minimizes the size of the optics.

To do so, x is assumed to be null. It becomes therefore possible to express the value of the focal length relative to the refracted angle:

$$f = \frac{\pi.c^2.d^2.\cos{\theta_r}^2.GDD}{2.\lambda^3} \tag{3.36}$$

The interval of focal length is evaluated over the interval of possible incident angles:

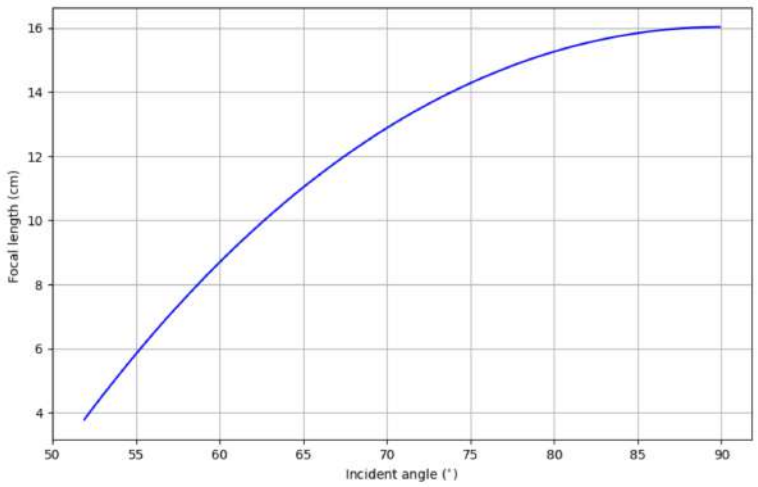

Figure 3.7 Evolution of focal length of the lens needed to achieve a GDD of 11.44 ps^2, relative to the incident angle.

As Fig 3.7 demonstrates, focal lengths must be set within the interval [4,16]cm. Then, estimating the minimal size of the optics needed to prevent clipping the spectrum becomes necessary. Indeed, as the grating is reflective, the spacing between the input beam and the output is limited and as such there is a risk of clipping the incident pulse with the optics sets. To avoid this scenario, the size of the diffracted beam at the position of the lens is first calculated, followed by an estimation of the size of optics required. Finally, the position of the beam is subtracted from the calculated size of the lens. The size at the lens is given by the formula:

$$S_{lens} = f.\sin(\frac{\pi}{2} - \theta_r) \tag{3.37}$$

The space between the incident beam and the size of the diffracted beam in the setup is now calculated:

$$R_{lens} = f.(\sin(\frac{\pi}{2} - \theta_i) - \sin(\frac{\pi}{2} - \theta_r)) - \frac{d}{2} \tag{3.38}$$

where d is the diameter of the incident pulse, f the focal length, θ_i the incident angle of the pulse in the referential of the grating, and θ_r the refracted angle of the pulse in the same referential.

Given the negative sign of the function under the focal length of 7.25cm, this section of the interval is discarded. Considering the pulse characteristics, a in-focus configuration of the stretcher is not possible. Therefore the grating is from now on considered to be out of focus of the lens. In this case, three parameters set the chirp of the output pulse: (f,θ_i,x) leading

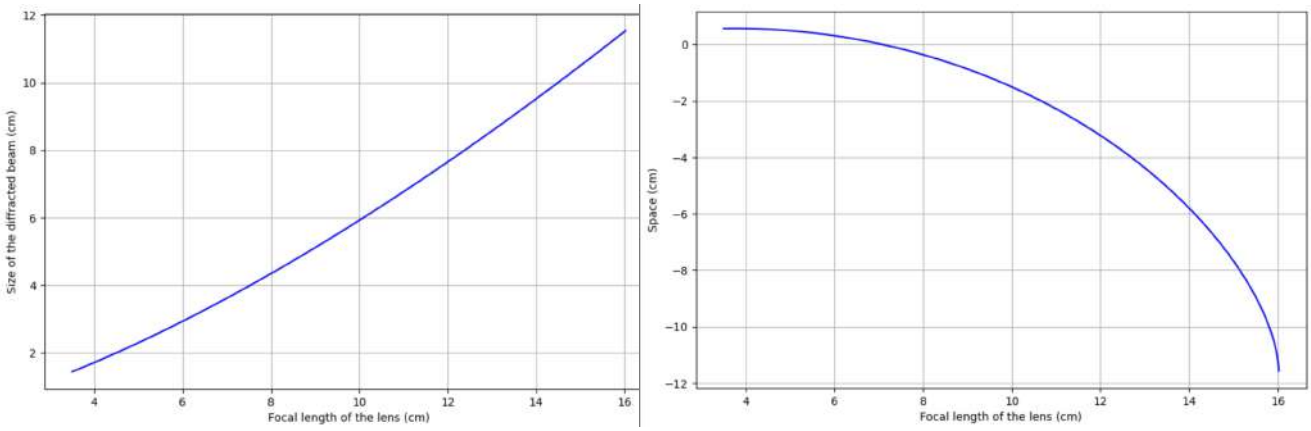

(a) Evolution of the size of the diffracted beam at the lens, relative to the focal length selected -and so the incident angle. Given the minimum value of the size of the diffraction, at the very least consider a 1-inch diameter lens much be considered

(b) Evolution of the interval between the incident pulse and the diffracted beam in the setup.

Figure 3.8 Evolution of available configuration.

to a GDD of 11.44 ps^2:

$$x = f - \frac{\pi.c^2.d^2.\cos\theta_r{}^2.GDD}{2.\lambda^3} \tag{3.39}$$

As established before, given the pulse spectrum the incident angle must be within the range of [51.44,90]°. As for the focal length, three representative values in accordance to the stretch ratio are selected: 10cm, 20cm and 40cm, leading to the results Fig 3.9:

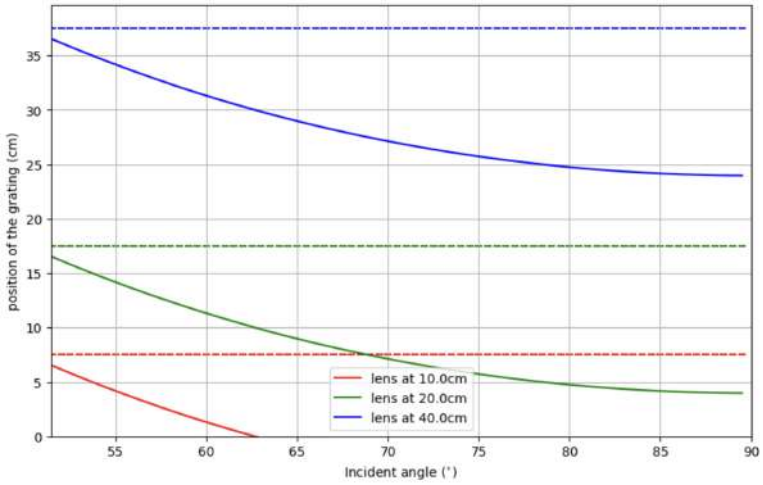

Figure 3.9 Evolution of the grating position given the incident angle of the input pulse. Each color corresponds to a different focal length: in red a focal length of 10cm, in green a focal length of 20cm and in blue a focal length of 40cm. The dotted lines represent the maximum value the grating position can take (stemming from the definition of the grating position along with physical constraint the grating is putting on the setup)

From this, intervals of incident angles can be associated to focal length, which is only limited for the smallest focal length value. The diameter of the lens is then calculated in the three cases to prevent clipping. In the precedent case, as the grating was in focus, the size of the diffracted beam at the lens position remains identical, regardless of the propagation direction. This is not the case anymore as the grating is within the interval of [-f,0] and as such the resulting image after one passing is expected to be bigger than the input object. To prevent any under-evaluation of the size of the diffracted figure, the size after all back and forth is calculated:

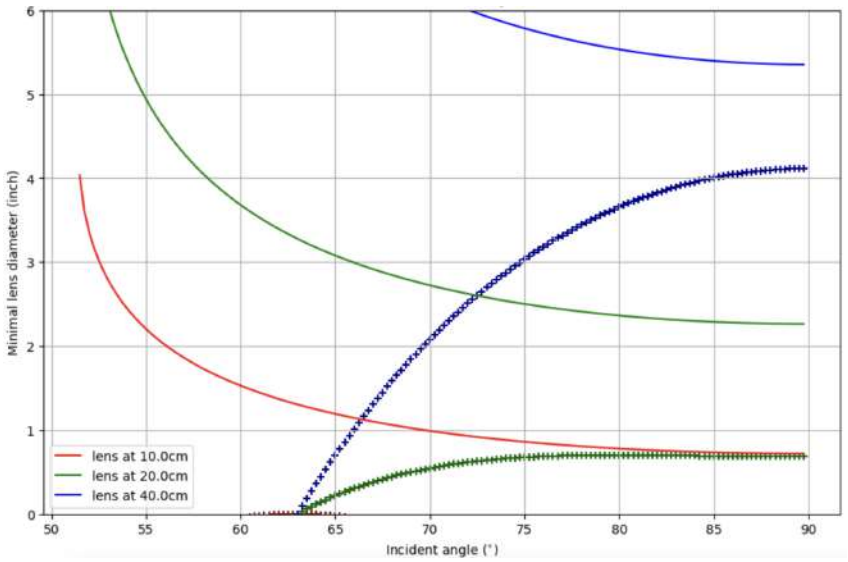

Figure 3.10 Evolution of the minimum lens diameter relative to the incident angle. Once again each color corresponds to a focal length of 10, 20 and 40 cm for the red, green and blue respectively. Straight lines correspond to the minimum diameter in inch while the dotted lines correspond to the available space between the incident ray optical path of the highest wavelength of the pulse spectrum.

In all three cases the minimum diameter for the lens needed to prevent clipping of the spectrum is superior to the available space between the incident beam and the divergent beam in the setup. To prevent this, one could either introduce a vertical angle -at the risk of generating angular dispersion and aberration in the orthogonal plane- or redesign the relative position of the optics. However both options do not lead to satisfactory results, whether it be in terms of pulse profile quality or reachable chirp.

Offner configuration

As demonstrated, the Martinez two-grating pair is not compatible with either the pulse characteristics and target. Another solution must be investigated. Once again it would be possible to use a fiber with the opposite GDD of the compressor. However this solution faces two hurdles: the pulse is at the frontier of the L-Band and the C-band, an affordable option complying both bands has yet to be found, and Higher orders mismatch would need to be compensated later in the setup.

Given this, the goal is from this point to build an equivalent setup to Martinez's. A good candidate to this end is the Offner setup. The appeal to the Offner setup is that it is not composed of transmission optics but of a concave Mirror M_1 of radius of curvature $-R_1$

and a convex Mirror M_2 of radius of curvature R_2. Finally, the expression of the effective

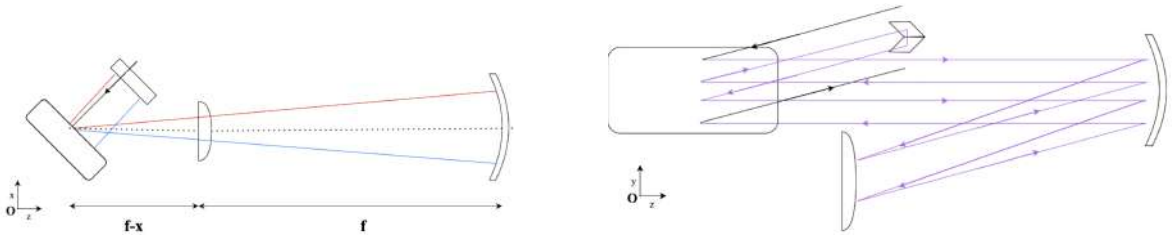

(a) Offner setup (from above).The convex mirror is positioned in the focus of the concave Mirror

(b) Offner setup (from side). All optics must be aligned to limit aberrations and angular dispersion

Figure 3.11 Caption Offner setup (from above and side)

path(calculated with ABCD matrix) is linear to the position of the grating and the radius of curvature of the mirrors -of course providing the conditions stated above are respected :

$$L = 2.(2.R_1 - 2.x) \tag{3.40}$$

With x the position of the grating relative to the concave mirror.

Power efficiency : Given the optics, the power efficiency is given by the equation:

$$P = R^4_{grating}.R^2_{Mconv}.R^4_{Mconc}.R_{Mirror} \tag{3.41}$$

Given the characteristics of the optics, this efficiency is estimated at 51.6%.

Stretch ratio : once more, before diving into Offner configuration, it is necessary to evaluate the Stretch Ratio. In a similar manner as before, the grating is placed at the focal length of the mirror, leading to an effective length of $\frac{R_1}{2}$:

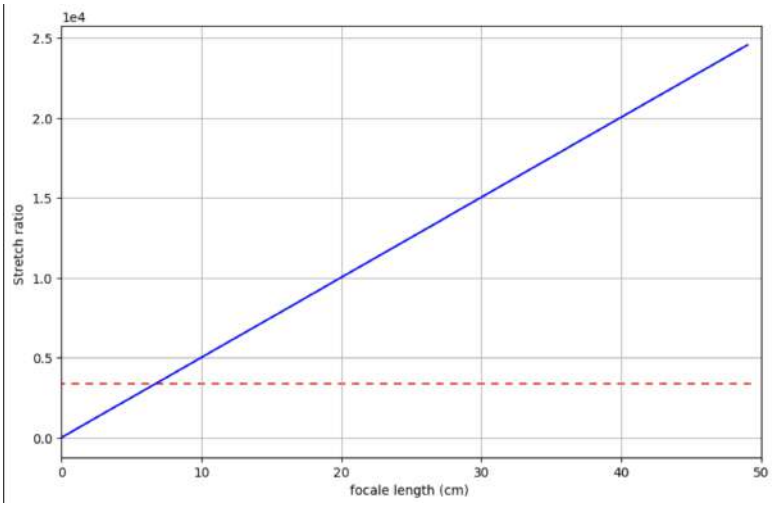

Figure 3.12 Evolution of the Stretch Ratio relative to the focal length of the mirror R1, in blue the stretch ratio obtain for an incident angle of 51.44°, the red dotted line in the minimal stretch required.

Unlike precedent cases and due to the configuration of this setup, reaching the maximum stretch ratio is not attainable -it would mean superposing the grating along with the convex mirror. Focal lengths higher than 10cm are considered.

Chirp : The intervals of (θ_i, R_1, x) yielding the targeted GDD value are determined as before. Given the expression of the GDD and the expression of the effective length:

$$GDD = \frac{\lambda_o^3.2.(2.f - x)}{2.\pi.c^2.d^2.\cos(\theta_r)^2} \tag{3.42}$$

The position of the grating is:

$$x = 2.f - \frac{2.\pi.c^2.d^2.\cos\theta_r{}^2.GDD}{2.\lambda^3} \tag{3.43}$$

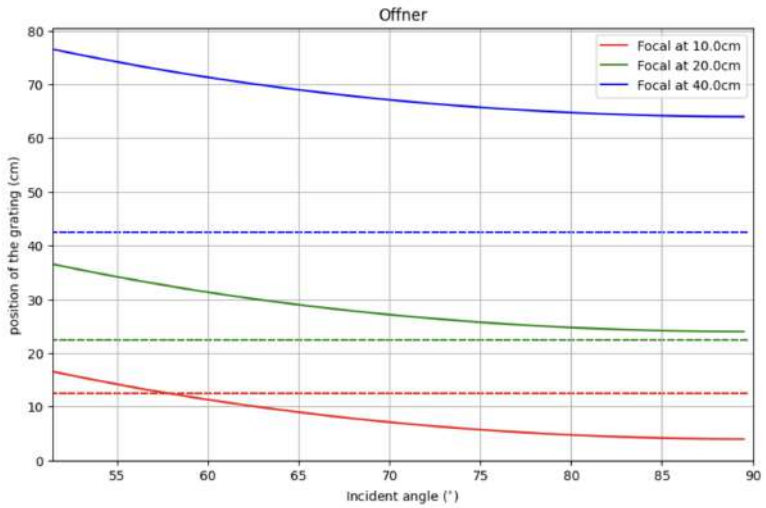

Figure 3.13 Evolution of the position of the grating relative to the incident line. One color is used per focal length -blue, green and red for respectively a focal of 10, 2-, and 4cm. The dotted line represent the minimum value taken by the grating.

Focal lengths under 10cm are discarded, as it would require to position the grating between the concave and the convex mirror, a design that would generate a great deal of angular dispersion and optical aberration -this issue will be tackled in a later section. From this, the feasability of the setup must be evaluated. Given the design, clipping the incident beam at the convex mirror is not possible. All that needs to be evaluated is the minimal size of the optics required by the design to prevent clipping at M_1. To this end, the 10% interval of wavelength [1540nm,1620nm] which is an overestimation of the beam size but will ensure clipping of the spectrum is avoided:

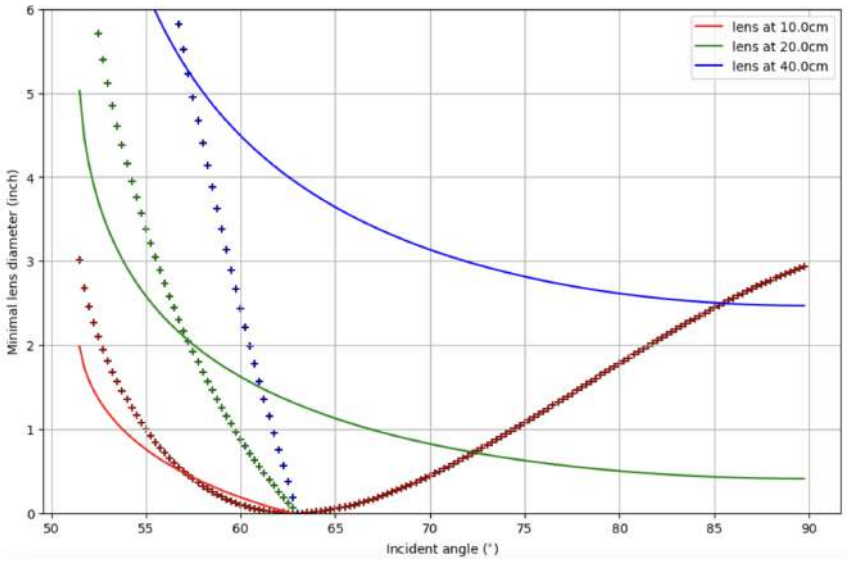

Figure 3.14 Evolution of the minimum diameter of the concave mirror M_1 required given the interval of wavelength. The dotted lines represent the space available between the incident beam and the diffracted beam.

Given the results Fig 3.14, any mirror with a focal length above 20cm cannot be considered as it would not only require unrealistic mirror diameter, and would also generate significant wavefront distortion -this will be tackled in a later section. As for focal length under 20cm, the available incident angle are too restrictive and as such the setup would lack flexibility. Considering a focal of 20cm would require the incident angle to be under 56.5°.

As such, the configuration is selected: (x, R, θ_i)=(36.15cm, 40cm, 52.00°).

Treacy configuration

One of -if not the- key setup to compress a pulse is the Treacy-pair grating (1969).

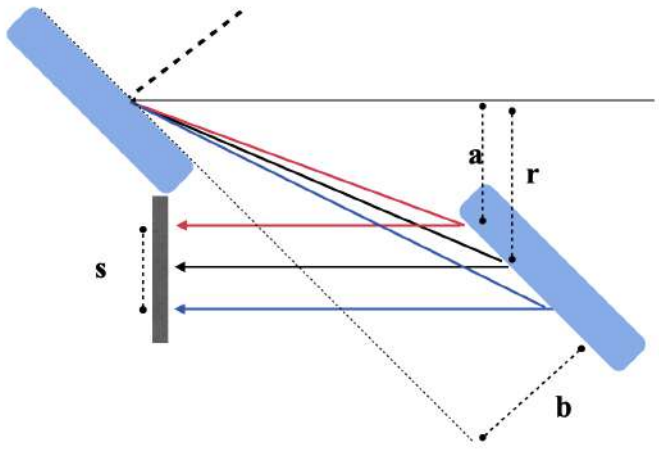

Figure 3.15 Treacy compressor design. Both gratings are oriented with the same angle relative to the incident light and separated by a distance b. This is the 2-gratings configuration, where the beam is reflected by a plane mirror, with an angle relative to the plane zOy as to separated the input from the output. s is the size of the diffracted beam, a is the space between the minimal diffraction angle and the incident light, b is the spacing between the gratings

Power efficiency Given the optics, the power efficiency of this setup is given by the expression:

$$P = R_{grating}^4 . R_{Mirror1} \tag{3.44}$$

Given the characteristics of the optics, this efficiency is estimated at 70.9%.

Chirp: The Treacy-pair compressor is the perfect equivalent of the Martinez -and so the Offner stretcher. Therefore the GDD's expression is given by the expression:

$$GDD = \frac{\lambda_o^3 . L}{2.\pi . c^2 . d^2 . \cos(\theta_r)^2} \tag{3.45}$$

With L the characteristic length of the optical path, given by:

$$L = 2.b. \cos(\theta_r) \tag{3.46}$$

Given the previous relations between GDD and the optical path: the characteristic length of the Treacy compressor is set to:

In order to determine the parameter's pairs (x, θ_i) generating the targeted GDD, L is ex-

pressed as followed:

$$L = GDD.(\frac{\lambda_o^3}{2.\pi.c^2.d^2.\cos(\theta_r)^2})^{-1} \tag{3.47}$$

L is then evaluated over the range of angle [51.44,90] °.

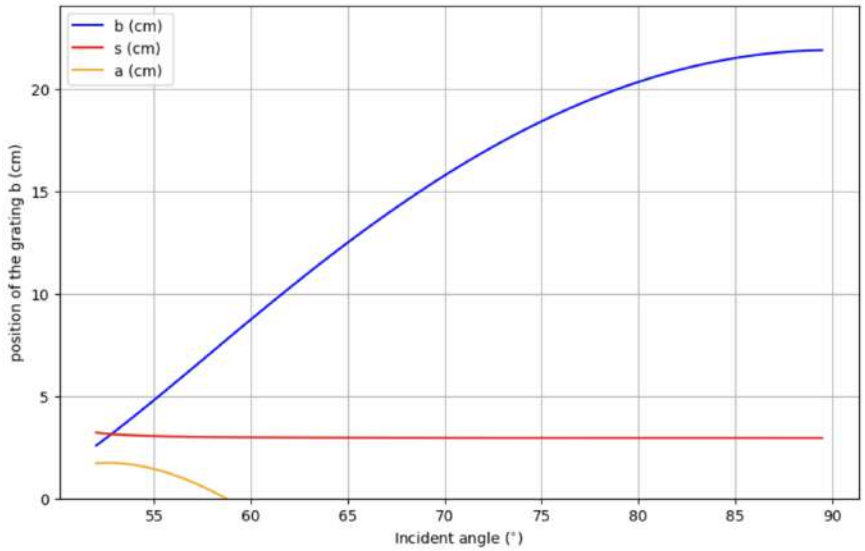

Figure 3.16 Treacy compressor design. S is the size of the diffracted beam at the reflection mirror, blue is the relative grating position associated to the incident angle, and in yellow is the space between the incident beam and the smallest diffraction optical path.

While selecting the parameters of the Treacy compressor, being the distance between gratings and the incident angle, one must take into account two limitations of the system:

1. The size of the beam s. Indeed, the reflected angle is positioned perpendicular to the interception between the incident light and the grating, and as such the size of the reflection mirror is limited. What's more is the gratings length also poses a limitation to the diffracted light.

2. The distance a, between the shortest diffraction path and the incident light. Indeed, should a be inferior to the grating thickness and the beam radius, the signal will be clipped which lead to significant power loss.

As the clipping of the pulse must be prevented, providing the grating's thickness and beam radius, the incident angle is set on the interval: [51.44, 54], as such the separation between the gratings is set between 2.1cm and 4.1cm. The final parameters are (x,θ_i)=(2.577 cm, 52°). With these parameters, the size of the diffracted pulse at the mirror is expected to be

1.41 inch.

In this section, the focus was on achieving an ideal stretcher/compressor pair. With the parameters determined comes the time to determine the impact of the fiber dispersion on the final output, and how to modify the parameters to compensate it.

3.4 Residual spectral phase

Up to this point, the stretcher/compressor pair was designed to be ideally matched. The dispersion taking place in the fiber was not included in the spectral phase generated. This approximation is valid so long that the pulse duration is over 1 ps. Since this is not the present case, residual spectral phase is bound to appear and its effects will impact the shape of the pulse. In order to mitigate the said effects, it is necessary to estimate the sensitivity of the system to high orders, the generated GDD and TOD contributions from the fiber and adapt the design.

3.4.1 High Order and pulse sensitivity

Before diving into the phase generated by the medium and the optics, it is necessary to study the sensitivity of the pulse given a residual phase. This way, a limit under which each residual order won't impact the pulse shape can be established: Given the value of the

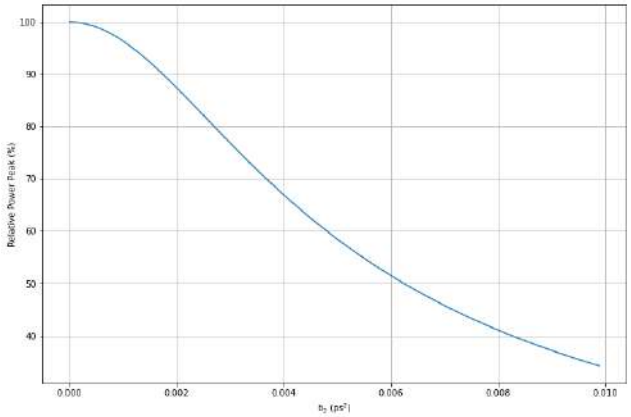

(a) Evolution of the maximum power peak relative to the residual GDD. The power peak is relative to the initial power (in percentage).

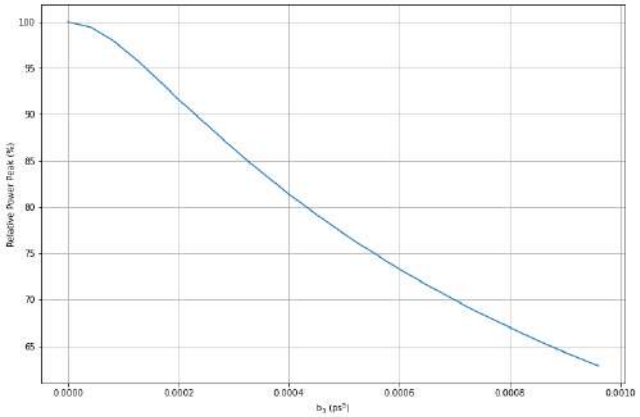

(b) Evolution of the maximum power peak relative to the residual TOD. The power peak is relative to the initial power (in percentage).

Figure 3.17 Evolution of the maximum power peak given the order of residual phase

pulse duration residual spectral phase will impact the pulse profile and more importantly the maximum amplitude. Figures 3.17a and 3.17b enables to establish the sensitivity of the system: in order to retrieve 90% of the amplitude of the Fourier Transform limit of the pulse, the maximum order 2 residual spectral phase is set at 0.0017 ps^2 while the maximum order 3 residual spectral phase is set at 2.3 10^{-4} ps^3.

3.4.2 Fiber dispersion

With the sensitivity of the pulse to residual phase being established, the spectral phase induced by the material is taken into account and compared to the limits. The data table 3.2 is a summary of the GDD and TOD generated in the fiber [1]: While TOD is under the

Table 3.2 Fiber dispersion values (from [1])

height	2^{nd} (fs^2)	3^{rd} (fs^3)
Fiber	30480.0	67500

limit, this is not the case for the second order. Should this not be compensated accordingly, the output would have the profile Fig 3.18:

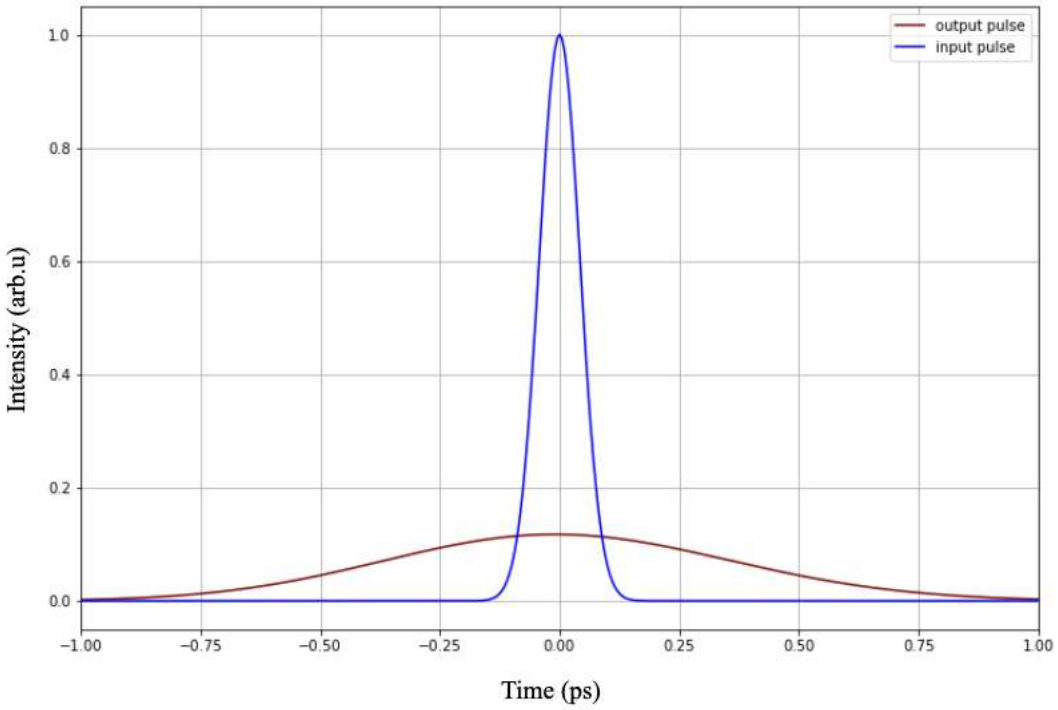

Figure 3.18 Evolution of the input pulse in blue before the stretcher and the output pulse in red after the compressor. The input pulse has a FWHM of 100 fs while the output pulse is of 850.98 fs

Given the residual second order, the output pulse would be almost 9 times wider than the inital pulse and the power peak be at 12% of the equivalent Fourier Transform profile. It is therefore paramount to compensate it in the setup. To do so, three options can be considered. A first approach would be to off-balance the Treacy'S configuration to compensate the second order. In this scenario, the GDD of the Treacy compressor is reevaluated at -11.47 ps^2. However, this slight off-balance between the stretcher and the compressor generates a residual TOD of 0.00125 ps^3. However as shown in Figure 3.19 this residual spectral phase shapes significantly the output pulse but also lowers the peak power by a 2/3 factor. In order to reach for the necessary peak power, a section to the setup would need to be added.

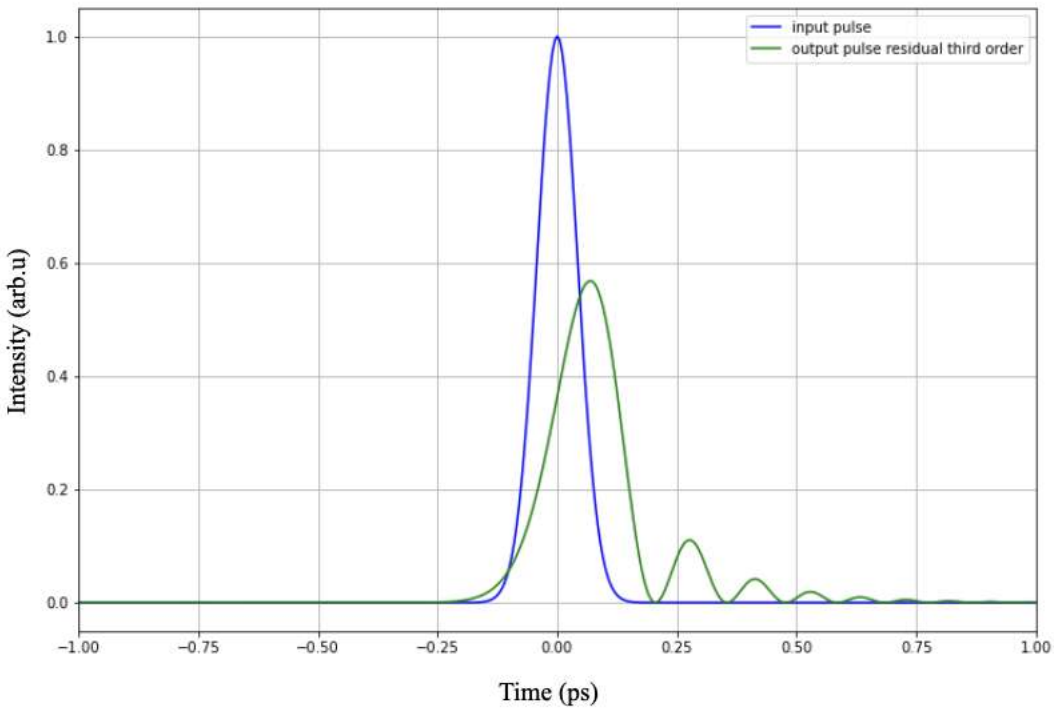

Figure 3.19 Evolution of the input pulse in blue before the stretcher and the output pulse in green after the compressor. In this case, the residual second order spectral phase generated by the fiber was compensated by off-balancing the Treacy Compressor, generating a residual TOD of 0.00125ps^3.

The second possibility is to compensate both the second and third order by detunning the incident angle θ_i and the grating spacing b of the compressor [29]. This method is standard when it comes to compensate second and third order for sub-picosecond pulses but requires for the stretcher and the compressor to be aberration free. As mentioned before, while the Treacy compressor is considered to be in an aberration free configuration, this is not the

case for the stretcher. Aberrations are expected. While this discard optimization through conventional method, this generation of aberration paves the way for a third approach to fiber dispersion compensation.

3.4.3 Aberrations generation

Aberration are more often than not a hurdle to compensate as it can lead to significant distortion of the wavefront. This case is no exception as the pulse is diffracted over a large section and is all the more sensible to distortion that impacts the spectral phase and so, the pulse shape. This section is dedicated to the evaluation of aberrations generated in the Offner setup and its use to compensate fiber dispersion.

Theory

Before diving into design's optimisation, it is necessary to present, if only briefly, the fundamentals on aberration generation. Up until this point, an ideal gaussian beam along with ideal optics were considered. In practice however this hypothesis can be challenged, because of two sources of deformations:

1. Chromatic aberrations due to the slight variation of refractive index of the optic's material , which can be limited with a specific coating.
2. Geometrical aberrations due to the structure of the optic. Under paraxial approximation such geometrical aberrations are negligeable.

Chromatic aberrations can be prevented with an appropriate choice of coated optics. This is not the case of geometrical aberrations, as the beam is diffracted at [-5°,13°] and as such, the inaccuracy is evaluated at [0.1%, 0.85%]. Given the sensitivity of the system geometrical aberrations and their impact on the GDD and the TOD of the stretcher must be considered. To do so, the Taylor development of the sinus and cosinus functions is extented to the order 3. From this mathematical development arises the five Seidel's coefficients:

1. Spherical Aberration B, which is due to the variation of the reflective/refractive index given the height on the optics.
2. Astigmatism C, leading to multiple images
3. The Field of Curvature D, the inability of a flat object to be focused on a flat screen (also called the Petzval effect)

4. The Field distortion E

5. The Coma coefficient F, caused by the optic's imperfection and leading to the image of a point object being a spot instead of a point.

From this third order development of the gaussian beam propagation, the variation of GDD and TOD are obtained [31]:

$$GDD^{abb} = 2(x_o^2(2B + D + F) + y_o^2(6B + C + D + 3F)).s^2.\frac{m^2.N^2.(2\pi)^2.c}{w_o^3.cos^2(\beta_o)} \tag{3.48}$$

and

$$TOD^{ab} = 6.y_o(4B + F).s^3.\frac{m^3.N^3.(2\pi)^3.c^2}{w_o^5.cos^3(\beta_o)} \tag{3.49}$$

Offner design

In the case of the Offner design, the Seidel coefficient are given by the expression [30] :

Table 3.3 Seidel's coefficients formula in the case of an Offner stretcher

coefficient	B	C	D	F
Expression	$\frac{(R_1-s)^4}{1.R_1^3.s^4}$	$2.\frac{(R1-s)^2}{R_1.s^4}$	$\frac{(R_1-s)^2}{R_1.s^4}$	$\frac{-2.(R_1-s^3)}{R_1^2.s^4}$

Given the characteristics of the Offner setup, the range of GDD and TOD generated by aberrations are estimated:

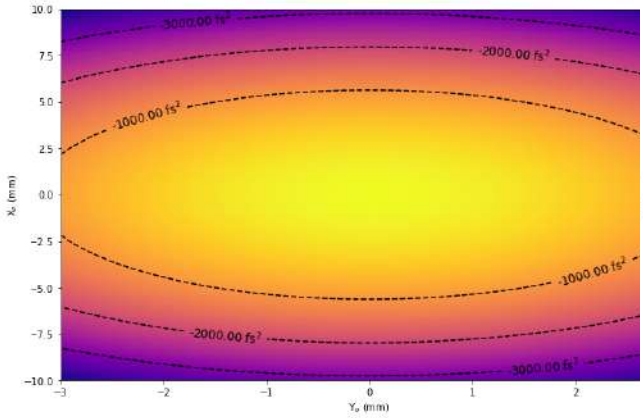

(a) Evolution of the GDD generated by geometric aberrations, the dot lines corresponds to typical values

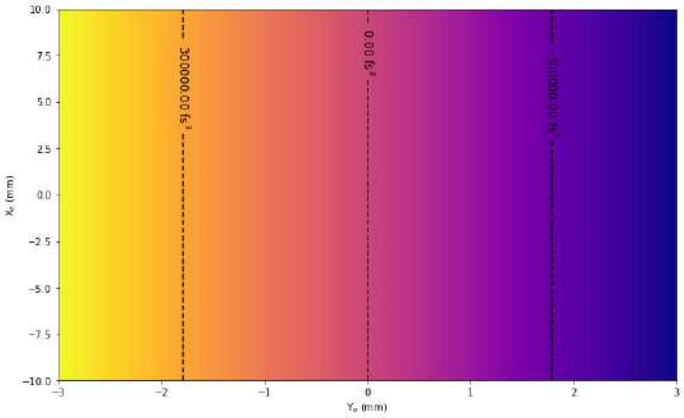

(b) Evolution of the TOD generated by geometric aberrations, the dot lines corresponds to typical values

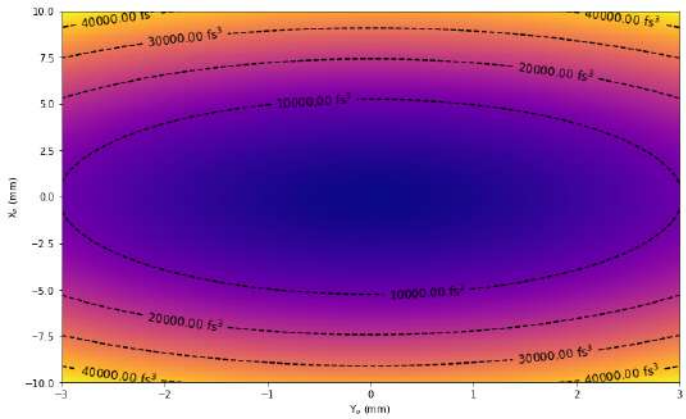

(c) Evolution of the TOD generated through the GDD^{abb}

Figure 3.20 Evolution of residual GDD, TOD and TOD^{GDDab} given the values of the (x_o, y_o)

The calculations reveal the following observations:

1. GDD$_{ab}$ is symmetrically dependent on the offset x and y. The order of magnitude is set at 10^3 fs^2.

2. TOD$_{ab}$ does not depend on the height x_o, which could have been easily predicted. While perfectly aligned, the symmetry of the setup and of the pulse spectrum coincide. Introducing a vertical offset keeps the plane symmetry while an horizontal breaks the

symmetry of the spectrum regarding the setup. The order of magnitude is estimated at 10^4 ps^3.

3. The modification of GDD_{ab} induces modified TOD, with similar symmetries and within the range of 10^4 ps^3.

Given the calculated values, aberrations don't allow for a complete compensation of the fiber's dispersion, all the more that offsets (x_0, y_0) must be selected within reasonable range of values, otherwise there is a risk of generating either a clip or -worse- departing from the model to the point that taking into account the Third Order of Seidel's approximation becomes necessary -which would introduce another set of seven parameters. To this end, both x_o and y_o must be selected under 1 cm.

Dispersion compensation

The final characteristics of the system are determined through the methodology:

1. Off-balance the incident angle of the Treacy Compressor to a fraction y. This enables to lower the disparity between TOD^{Treacy} and TOD^{Offner}.

2. Establish a fraction x of the GDD generated by the fiber to be compensated by the Treacy compressor. As established previously, the GDD generated through aberration is negative, with a maximum absolute value of 3000 fs^2. Combined with the limit of 1700 fs^2 tolerated, the compensation ranges in [25 780; 32 180] fs^2.

3. Determine the new relative position of the gratings in the compressor to obtain a system with a residual GDD of (1-x).GDD^{fiber}.

4. Minimize the residual TOD with aberrations in the Offner stretcher.

5. Minimize the residual GDD with aberrations

6. Reevaluate the residual TOD with the contribution of the GDD^{abb}.

This methodology is an iterative process and is repeated until residual GDD and TOD are set under the values defined in the previous section, with achievable (x_o,y_o) parameters. The updated parameters are summarized in Table 3.4:

Table 3.4 Final compressor parameters and aberration generation

parameters	x_{Treacy}	$\theta_{iTreacy}$	$x_{oOffner}$	$y_{oOffner}$
Initial value	2.577 cm	52	0	0
Modified value	2.598 cm	52.02°	4 mm	2 mm

The final dispersion phases are calculated accordingly, yielding the results in Table 3.5:

Table 3.5 Calculated values of GDD and TOD in all sections of the setup

Section	Compressor	Stretcher ideal	Stretcher aberrations	Material	total
GDD (ps^2)	-11.459	11.44	- 890.10^{-6}	30480.10^{-6}	24.10^{-6}
TOD (ps^3)	0.4444	-0.4448	-378460.10^{-9}	67000.10^{-9}	-32 612 fs^3

With these parameters, the residual GDD is estimated at 24 fs^2 while the residual TOD is estimated at -32 612 fs^3, leading to the output pulse Fig 3.21:

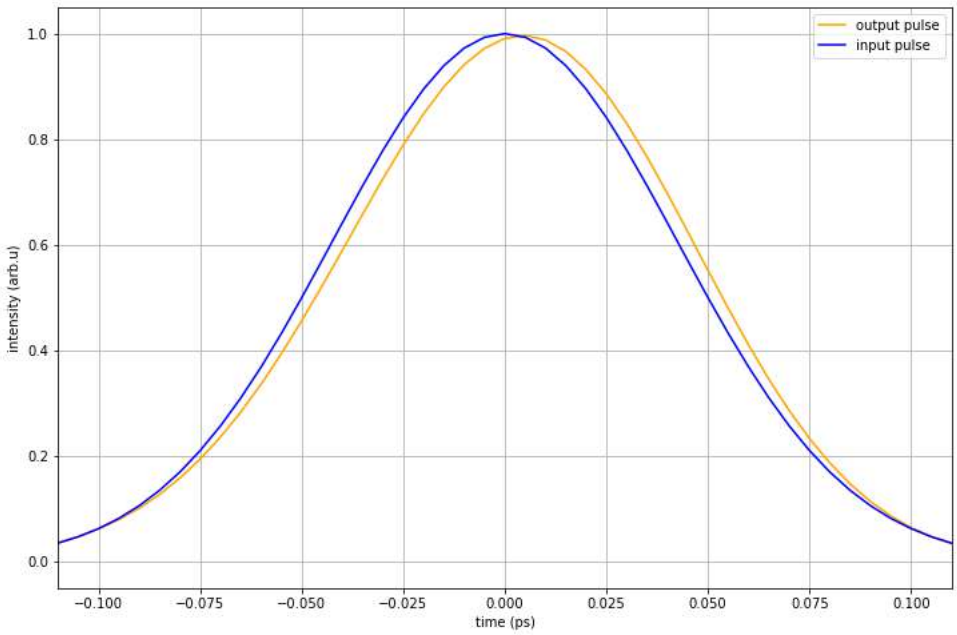

Figure 3.21 Final output pulse expected, after evaluation of the material dispersion and compensation through off-balance and aberrations. The Pearson correlation coefficient is estimated at 0.998.

In order to estimate the impact of the residual GDD and TOD on the pulse output, the Pearson correlation coefficient between the input and the output is calculated, yielding a value of 0.998. The impact of the residual phases can therefore be deemed negligible.

3.5 Experimental results

With all parameters determined, the installation of the setup can take place. This is done in two steps: first the sensitivity of the system is estimated in order to lower the uncertainty of the result as best as possible, secondly the output pulse of both the stretcher and the compressor is characterized.

3.5.1 System precision

In order to plan the installation of the setup, the sensitivity of the system must be established. This way the precision on the measurement can be evaluated, then limited.As detailed before in the theoretical section, the pulse duration reach its minimum in the absence of pulse. A

residual GDD will therefore increase the pulse duration:

$$\tau_{FWHM} = \sqrt{8.\log 2}\sqrt{\sigma^2 + \frac{b_r^2}{2!^2.\sigma^2}} \tag{3.50}$$

leading to the linear evolution of the pulse width Fig 3.22:

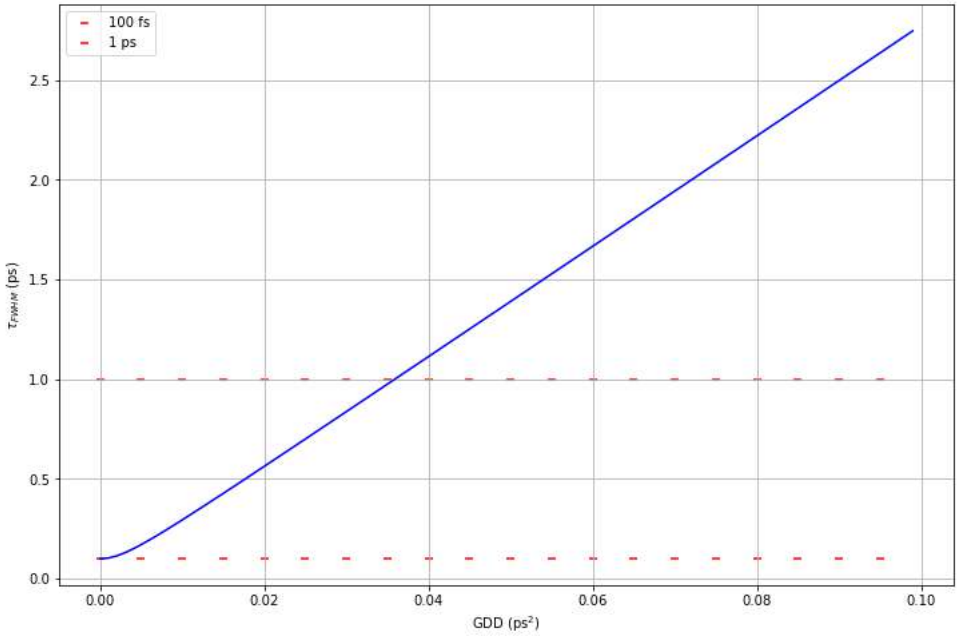

Figure 3.22 Evolution of the pulse half width full maximum relative to the residual order two present. The red dotted line represent respectively the initial pulse width along with the ten-time pulse width limit.

The evolution of the pulse width becomes quickly significant, as a mere missmatch of 20 000 fs^2 yields an output pulse width six time bigger than the initial value. This is considered to be the tolerable limit imposed on the system and from this point, the maximum uncertainty imposed on both the stretcher and the compressor is set to 10 000 fs^2. The uncertainty on the GDD is therefore estimated to 0.1% per stretcher/compressor.

Given this parameter, the tolerance on the angle of incidence/the relative angle of the gratings, their relative positions is evaluated.

Angle tolerance

By introducing an uncertainty $\Delta\theta_i$ on the system, the divergence on the GDD value are evaluated:

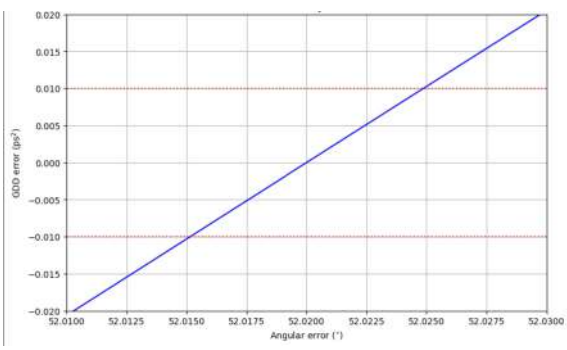

(a) In blue the evolution of the error made on the GDD induced by the variation on incident angle, in red the limit at 0.1%.

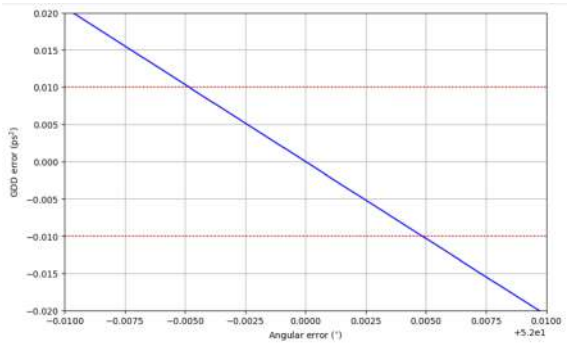

(b) In blue the evolution of the error made on the GDD induced by the variation on incident angle, in red the limit at 0.1%.

Figure 3.23 Evolution of the relative error given the angle's uncertainty

In order to remain within the uncertainty interval of the GDD, the precision of 52.02 ± 0.005 ° must be achieved. To do so, irises are used as reference points and power is measured after each. As illustrated by Fig 3.24, maximum is reached at both irises when the beam is aligned with the optical axis.

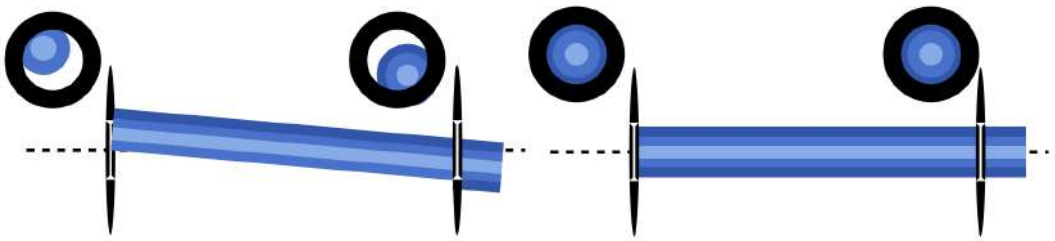

Figure 3.24 Alignement of a beam through iris. The maximum intensity detected is reach when the beam is paralel to the optical axis.

The irises are positioned at 75cm from one another. Over this distance a deviation of 0.005 ° yields a deviation of 0.065mm from the optical axis.

The beam's diameter is 3.4mm. Providing a spatial gaussian distribution Fig 3.25, the

standard deviation is estimated at:

$$\sigma \sim 0.85mm \tag{3.51}$$

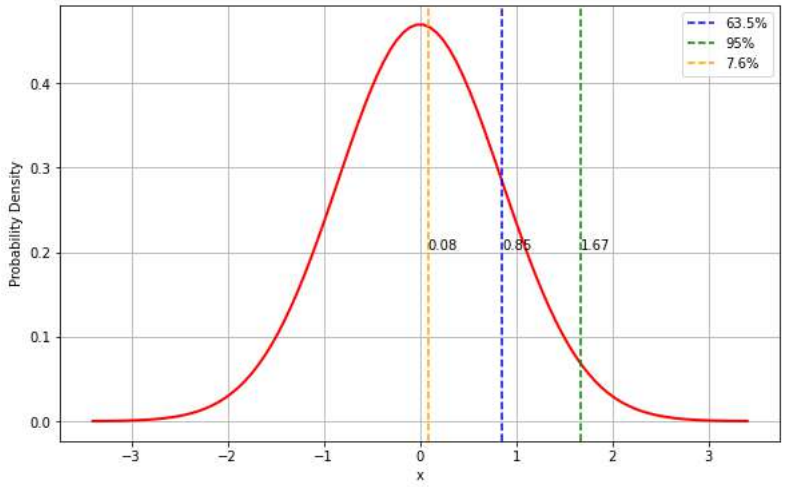

Figure 3.25 Normal distribution with percentile: in blue the 68.5%, in green the 95% percentile,percentile, both centered around the mean μ=0 and in yellow the 7% percentile associated to the uncertainty deviation

The irises' diameter is then lowered until 5% of the input power is detected by the power meter. Given the normal distribution Fig 3.25 this corresponds to a diameter of 0.06 mm. The uncertainty of the central position of the beam is therefore set at 0.06 mm and the angle's uncertainty is evaluated under 0.005°

All angles are aligned through this mean.

Gratings

In a similar fashion, an uncertainty over the grating position and the angle is introduced, and the divergence from the target GDD evaluated.

Position The minimal grating position precision is now evaluated for both the Offner and the Treacy setups:

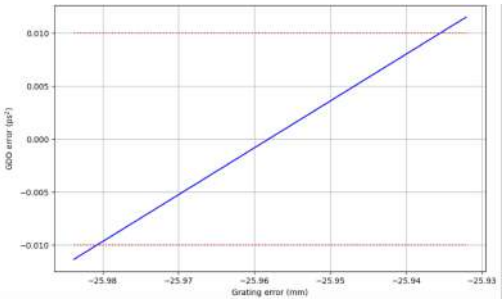

(a) In blue the evolution of the relative error made on the GDD induced by the variation on incident angle, in red the limit at 0.1%.

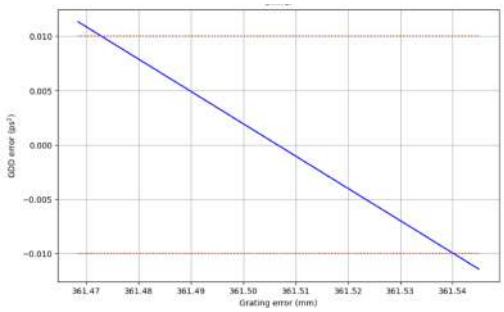

(b) In blue the evolution of the relative error made on the GDD induced by the variation on grating position, in red the limit at 0.1%.

Figure 3.26 In blue the evolution of the relative error made on the GDD induced by the variation on incident angle, in red the limit at 0.1%.

To remain within the tolerable values of 0.1 mm, the strategies are set:

1. Regarding Offner configuration, the precision of 0.1mm is not achieved through the angle. Since the precision on the angle is set at 0.05°, the position of the grating is adapted so that the beam reaches the grating at a point of reference, yielding a variation of mirror cavity-grating distance to be set between 361.47 and 361.54 mm.

2. Regarding the Treacy configuration, the precision of the on the separation between the two grating is 0.1mm Once more, the the precision over the distance is induced through the precision of the angle.

Angle The relative angle of the grating is likely to lead to uncertainty similar to the one induced by incidence angle. To mitigate this and lower the angular uncertainty under the set value, the polarisation of the beam is set so that the reflected light -order 0- is favored over order one which is then used as a reference axis.

3.5.2 The power efficiency

The output power of the compressor and the stretcher were measured with a power-meter. The output power of both the compressor and the stretcher was measured using a power meter. The power input of the stretcher being 65.7 mW and the output power being measured at 30.15mW, the power efficiency is 45.89%. Regarding the compressor, a power input of 30.15mW yields a power output of 20 mW, corresponding to a power efficiency of 66.33%.

Achieving these power efficiencies, when compared to their respective theoretical values of 70.9% and 51.6%, serves as a robust indicator that significant clipping was avoided and no oversights occurred during the conception of both setups. This 6% discrepancy must be investigated to ensure this is caused by clipping of the pulse or -worse- the clipping of the spectrum.
During the evaluation of the maximum power efficiency of both setups, it was assumed that the gratings would behave ideally, except for the 8% power absorption. That is the selection of the order of diffraction was assumed to be ideal, with 100% of the non-absorbed power being directed into the order -1. This was investigated to determine whether the gratings might account for the 4% margin observed in the experimental results. The orders of diffraction most likely to retrieve a small fraction of the input signal are adjacent orders, 0 and 2. Nevertheless, as mentioned earlier, the diffraction orders of the grating are governed by the grating master equation. The characteristics of the optical setup and the central wavelength of the pulse makes it impossible to generate order-2 diffraction. However, the same does not hold for order 0.

At maximum attenuation, the reflected beam's power was adjusted to 1% of the input power. Consequently, given the initial power, the efficiency of order 1 selection is reassessed to be 1%, leading to theoretical power efficiency values of 67.8% and 49.9% respectively. The designed system aims to reach 97.8% and 91.9% of the theoretical power, respectively.

3.5.3 Chirping of the pulse

With the power efficiency measured, the chirp must be characterized in each section of the setup. A first solution to do so is to realise a Frequency-resolved optical gating (FROG) measurement as it yields a better precision on the measurement. However the available range of the FROG setup in laboratory is set well under 100 ps, the pulse cannot be measured in its integrity. Another option would be to combine both setups to measure the output pulse at the end of the setup. However, the expected resulting power is set at 24 mW. While a signal could be measured, it would be faint, and would not ensure that the pulse fed to the amplification fiber is at the desired effective pulse duration.

For all these reasons, the pulse is characterized with an Ultrafast Oscilloscope, with a sampling rate set at 40 GSA/s (yielding a precision of 2.5 10^{-11}s). To ensure a statistical deviation under 5%, the signal is recorded and averaged over 15 iterations. Fig 3.27a and Fig 3.27b are the respective averaged profiles.

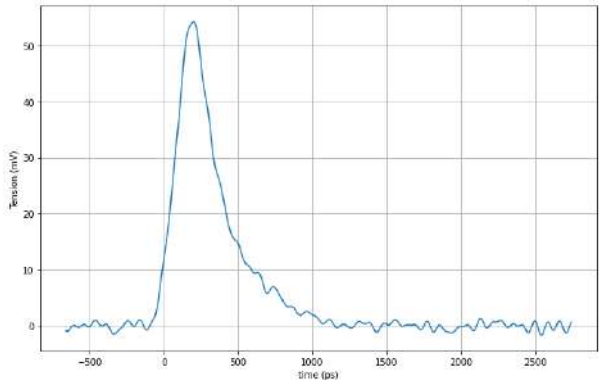

(a) Measured profile of the Offner output (averaged over 15 profiles). The FWHM of the beam is measured at 291ps

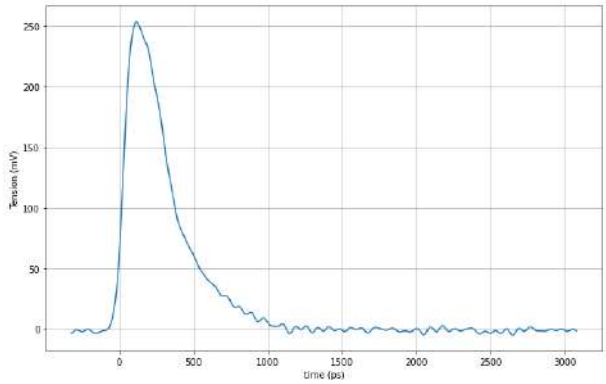

(b) Measured profile of the Treacy output (averaged over 15 profiles).The FWHM of the beam is measured at 306 ps

Figure 3.27 Evolution of the maximum power peak given the order of residual phase.

According to the simulations, this corresponds to a GDD of -11.76 ps^2 for the compressor and 11.47 ps^2 for the stretcher. Indeed, after subtraction of the dispersion generated in the fiber set at 30 480 ps^2, the discrepancy between the the $GDD_{compressor}$ and $GDD_{stretcher}$ is set at 0.26 ps^2. The resulting FWHM of the output signal is therefore estimated at 7.2 ps.

Indeed, the variation of stretched length is estimated at 0.63%, meaning the amplification of the pulse is similar to the theoretical value. However the output pulse is 7200 longer than the input pulse. The peak power is therefore impacted as well:

$$P_{peak} = \frac{P_{av}}{f_{ceo}.\tau} \tag{3.52}$$

The impact this discrepancy has on the system is first estimated in the case of 2-photon-absorption [2]:

$$P_f^{(2p)} = \eta^{(2p)}\sigma_a^{(2p)}.\frac{\nu_f}{2.\nu_a}.\frac{P_{av}^2}{A_{eff}}.\frac{g_p}{\tau_p.f_{ceo}} \tag{3.53}$$

with:

1. $\eta^{(2p)}$ the quantum efficiency.
2. $\sigma_a^{(2p)}$ the cross section absorption.
3. τ_p the pulse duration, estimated at the FWHM.
4. f_{ceo} the repetition frequency.

5. g_p the pulse shape coefficient.

6. the ν_a the frequency of the photons absorbed.

7. the ν_a the frequency of the photon emitted by fluorescence.

Given the dependency on the pulse duration, to obtain the same power generated with a 100 fs pulse, the irradiance must be increased:

$$\frac{A_{eff2}}{A_{eff1}} = \frac{\tau_1}{\tau_2} \tag{3.54}$$

$$\frac{r_{eff2}}{r_{eff1}} = \sqrt{\frac{\tau_1}{\tau_2}} \sim 11.78\% \tag{3.55}$$

Multiphoton Microscopy remains therefore possible, providing a modified irradiance compared to the initial 100 fs pulse. Nevertheless the residual phase introduces a variation of g_p compared to the gaussian case and will introduce parasitic effects while propagating in the biological tissue. Both setup needs to be realigned in order to better fit the target.

3.5.4 Interferometric autocorrelator

As mentioned in a previous section, the expected pulse duration after the stretcher and compressor in the targeted configuration, in the absence of fiber, is expected to be 858 fs, and 100 fs with the propagation in the fiber. This time characteristic is far below the response time of electric devices such as photodiodes. In order to characterize the signal output, an interferometric autocorrelator setup is used.

Theory

The setup of an interferometric autocorrelator -Fig 3.28- is very similar to the Michelson's: a beamsplitter divides the input light in two perpendicular paths. Each path includes a mirror one is fixed -M_1- and the other's position is adjustable -M_2. After reflection the two beams are recombined on the beam-splitter before being focus on a non linear crystal to generate second harmonic.

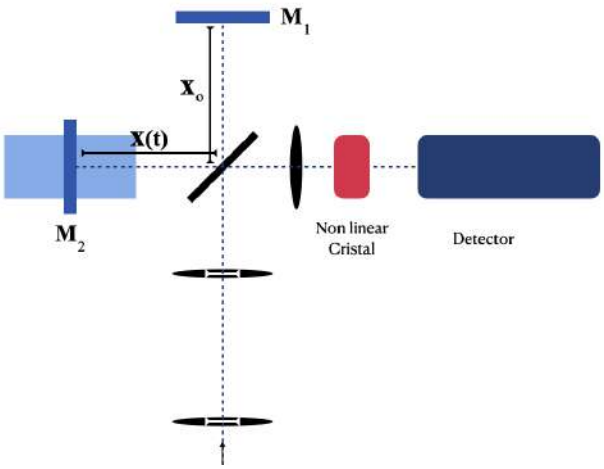

Figure 3.28 Diagram of an interferometric autocorrelator. Mirror M_1's position x_o is used as reference while M_2 mirror x varies.

Note that in the case of an interferometric autocorrelator, the detector records the following intensity :

$$I_{ac}(\tau) = \int |E(t+\tau) + E(t)|^4 . dt \tag{3.56}$$

which can be developed as follows:

$$I_{ac}(\tau) = \int |E(t+\tau) + E(t)|^2 |E^*(t+\tau) + E^*(t)|^2 . dt \tag{3.57}$$

and so:

$$\begin{aligned} I_{ac}(\tau) = & \int I^2(t+\tau) + I^2(t)\, dt \\ & + 4 \int I(t+\tau) \cdot I(t)\, dt \\ & + 2 \int (I(t+\tau) + I(t)) \cdot E(t) \cdot E^*(t+\tau)\, dt \\ & + \int E^{2*}(t+\tau) . E^2(t)\, dt \end{aligned} \tag{3.58}$$

with in order:

1. The Constant term.
2. The intensity autocorrelation term.
3. The interferogram of E(t) term, oscillating at ω.
4. The interferogram of the second harmonic, oscillating at 2ω.

It is important to define two different time characteristics: the pulse duration - self-explanatory - and the coherence time, which is the duration during which interferences are observed. In the absence of chirp, the front and the back of the pulse can interfere, so the coherence time of the interferogram equals the pulse duration, implying that the FWHM is retrieved through the maximum envelope of the IAC trace. However, in the case of a chirped pulse, interference between the front and the back of the pulse is not guaranteed along the entire pulse: the pulse duration is greater than the coherence time. Therefore, in the case of a chirped pulse, retrieving the FWHM of the trace itself would lead to an underestimation of the actual pulse duration. The easiest way is to retrieve the intensity correlation from the trace by filtering the ω and 2ω terms of the trace [39], [40]. After subtracting the constant background, the intensity autocorrelation can be retrieved. After assuming a pulse shape, a fit is carried out, yielding the FWHM of the intensity trace. In the case of a Gaussian shape, the FWHM of the pulse is determined by dividing the FWHM of the intensity trace by a factor $2^{1/2}$.

Laser Output

In order to better characterize the chirped pulse, it is necessary to have a good initial guess of the un-chirped pulse shape. The hypothesis is that the un-chirped profile does not change drastically between the source output and the system output. Major change could occur due to spectrum clipping. Given the power efficiency, frequency clipping is expected to be minimal if not absent and no major change are expected between the source and the final output.

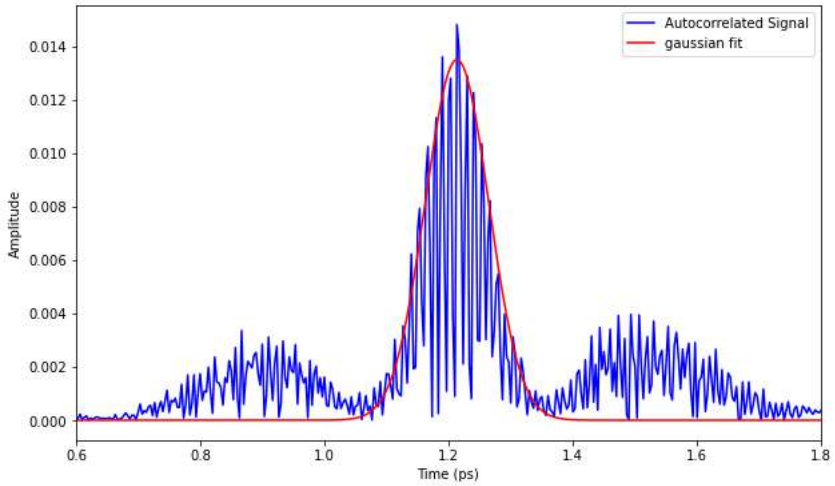

Figure 3.29 IAC trace of the laser source in blue, in red the gaussian fit with a FWHM set at 120.02 fs

The trace is filtered to remove the noise:

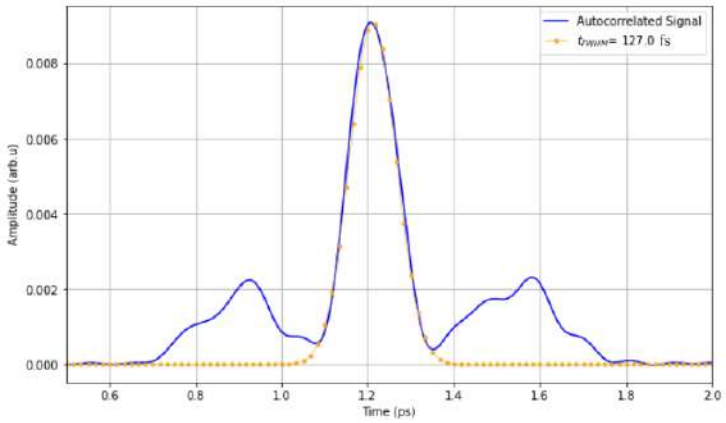

Figure 3.30 IAC trace of the laser source in blue, in red the gaussian fit with a FWHM set at 127 fs

From Fig 3.30, the gaussien fit FWHM is set at 127 fs, yielding an equivalent pulse duration of 90 fs. However the shape of the pulse is not gaussian, with the presence of two tertiary lobes. The first initial guess could be to attribute this to TOD, inherent in the laser cavity. However this would be unlikely for the following reasons:

1. The traces filtered respectively at high and low frequency have the same profile, as such no linear chirp takes place. The generation of TOD without GDD seems unlikely.

2. The Time bandwidth product of the pulse is specified to be set at 0.43, which is all but equal to the theoretical value of pure gaussian beam.

It seems more likely that the shape of the trace is due to a lingering dispersive wave occurring in the laser cavity.

Stretcher/compressor output

With the source signal being characterized, focus is shifted to the resulting signal output of the stretcher/compressor. First, data acquisition time is realized in the absence of fiber Fig 3.32:

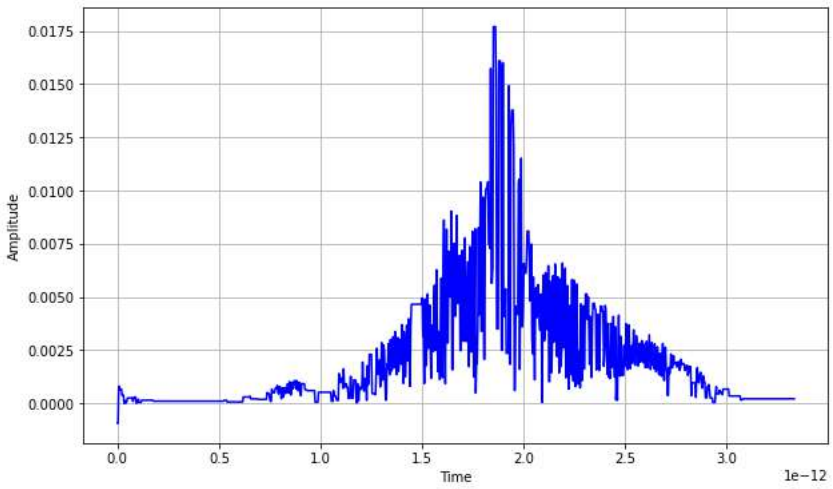

Figure 3.31 IAC trace of the stretched/compressed pulse in blue, after prossessing to substract background

As expected, the noise contribution is much higher after the stretcher/compressor than it is at the initial source output. Indeed while the laser yields an average power of 100 mW, the stretcher/compressor yields an average power of 20 mW.

First the τ_{FWHM} of the IAC trace is measured at 343.63 fs, yielding an equivalent pulse duration of 240 fs. This provides a first estimation of the pulse duration, though this value is underestimated. In order to improve the estimation of the pulse duration, high frequencies are filtered and a gaussian fit is realised Fig 3.32:

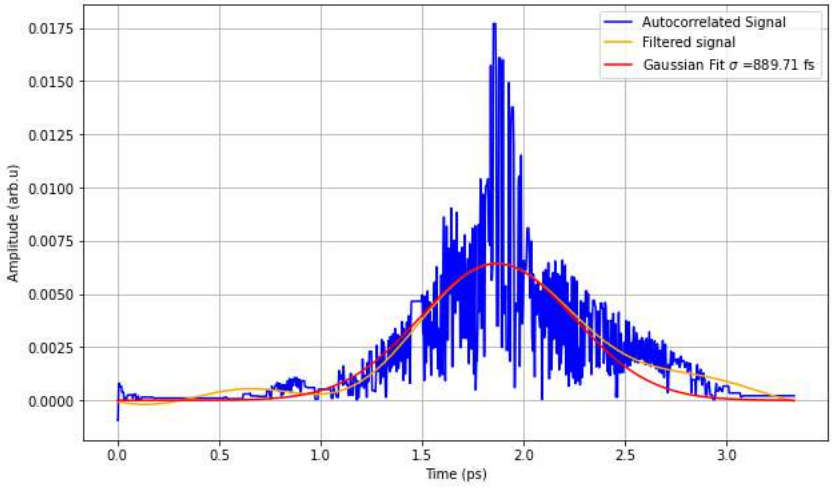

Figure 3.32 IAC trace of the stretched/compressed pulse in blue, in orange the signal filtered out of noise (frequency cut-off at 32.10^{11} Hz), in red the gaussian fit

With the gaussian fit, the FWHM is estimated at 889.71 fs, which corresponds to a duration of 631 fs of the pulse, and an absolute GDD of 22 490 fs^2. Providing that the GDD generated is negative, after the fiber, the final output width is therefore expected to reach 243 fs, which is within the boundaries established beforehand. Should the GDD be positive, however, this would lead to the output FWHM to reach 1.47 ps. Given previous measurements and considering that the alignment corrections were minimal, one can reasonably expect the residual GDD to be negative and the final output FWHM be set around 243 fs. This value is well within the tolerance established previously.

Discussion

The realignment of the setup seems to have resulted in a smaller discrepancy between the stretcher and the compressor, leading to an expected FWHM of 243 fs at the output of the setup, which is well within the established tolerance limit in terms of GDD. That being said, while IAC provides information on pulse duration and relative chirp, it delivers ambiguous pulse profiles and does not provide information regarding the spectral phase on the entire bandwidth. While a Gaussian profile was assumed here, multiple effects must be taken into account. First of all, the noise contribution is quite high, which inevitably impacts the signal processing. Furthermore, in order to determine the GDD, the absence of TOD was assumed.

Given the fact that the exact values of GDD were not reached—otherwise, the pulse duration would have been 858 fs according to the IAC trace—high orders may have relatively higher contributions to the trace. In that case, the most problematic would be the TOD, which would lead to the apparition of multiple tertiary pulses. However, should this be the case, tertiary IAC traces would have appeared on each side. Either the or the noise level is too high to detect them. This needs to be confirmed; first, an IAC trace of the stretcher/fiber/compressor setup and a FROG measurement which will better characterize the spectral phase.

Another source of issues regarding this IAC trace is the dispersive wave. In the case of the initial seed source trace, the separation between the pulse and the dispersive wave was easy to determine, mostly due to the low noise level. However, in the case of the stretcher/compressor, not only is the noise level higher, but the dispersive wave was chirped as well. Providing a similar but different central wavelength and bandwidth, it would be able to propagate through the setup along with the pulse but would experience different chirp values and aberrations. Once more, this needs to be confirmed through the IAC trace of the entire setup and a FROG measurement

CHAPTER 4 ERBIUM YTTERBIUM CO-DOPED AMPLIFICATION

Rare earth ion luminescence has been under study since the beginning of the twentieth century, and its applications vary from CRT phosphors to solid state lasers and of course, optical amplifiers. This is mainly due to the structure of the rare earth elements: the 4f structure leads to a localised electronic cloud and causes the resulting spectrum line to be thin.

Over the past decades erbium has become a subject of focus as it spectrum are located in one of the two loss windows of silica: 1200-1350nm and 1450-1600 nm (also known as the ultra-loss window). Interest in multiphoton imaging has been growing, designing high power source at 1500-1600 nm became paramount and as mentioned before, erbium doped derived fibers has been the go-to solution to achieve this. However erbium doped fibers, while highly efficient and offering low noise solutions, remain limited in terms of output power to 20dB with limited noise figures of 3dB. To increase the possible gain while maintaining Noise Figures below 7 dB, erbium ytterbium doped fibers have been increasingly used.

This chapter is dedicated to the design of the optical amplifier, in terms of length, pump source, ion concentration and offers a first characterization on gain and noise generation. Given the non-linearity of the system, the numerical resolution is first achieved and characterised in steady state, to be used to estimate gain in time-dependant signal.

4.1 Amplification theory

The principle of an Optical Amplifier (OA) is to transfer power from a pump signal at a given wavelength λ_p to the signal at wavelength λ_s. In the case of doped fibers amplifiers (DFA), this is achieved through a population inversion in the medium. This section focus is set on setting the definitions and parameters necessary to the conception of an optimized DFA.

4.1.1 Definition and principles

There are three main focus when designing an amplifier: reach high output power with minimal pump power, all of which achieved without significantly lowering the Signal to Noise Ratio (SNR). In order to quantify the quality of the amplifier regarding each parameters, the parameters are defined:

Gain value G assesses the efficiency of the amplifier to increase the signal's power. It is defined as:

$$G = 10.\log_{10}(\frac{P_{out}}{P_{in}}) \text{ dB} \tag{4.1}$$

Noise figure : While spontaneous emission has a minimal contribution, it can however trigger stimulated emission and as such, a fraction of the pump power is redirected toward the amplification of a parasitic signal: the Amplified Spontaneous Emission (ASE). This impacts both the gain and the SNR as well. The contribution of ASE is evaluated through the Noise Figure (NF):

$$NF(\lambda) = (\frac{\rho_{ase}(\lambda)}{h.\nu} + 1).\frac{1}{G(\lambda)} \tag{4.2}$$

With G the gain, ρ_{ASE} the spectral density of ASE at a given wavelength, h the Planck's constant and ν the frequency of the signal.

In the case of high gain amplifiers, NF can be simplified to:

$$NF(\lambda) \simeq 2.N_{sp} \tag{4.3}$$

where N_{sp} is the spontaneous emission factor. Let's consider two energy levels, with the respective electronic populations n_1 and n_2 and the cross sections σ_{12} and σ_{21}. The spontaneous emission factor is the ratio between the spontaneous emission and the stimulated emission population transition :

$$N_{sp} = \frac{\sigma_{21}.n_2}{\sigma_{21}.n_2 - \sigma_{12}.n_1} \tag{4.4}$$

In the ideal case -being a perfect population inversion- the spontaneous and the stimulated emission have equal efficiency. N_{sp} is therefore equal to one and NF equals 3 dB. In reality the population inversion cannot be perfect and as such NF is superior to 3 dB.

Pump efficiency η_p: . The pump efficiency enables to evaluate the achieved gain relative to the pump increase:

$$\eta_p = P_{sat}.\frac{\partial G}{\partial P} \tag{4.5}$$

with P_{sat} the maximum output power the medium can yield.

4.1.2 Choice of Dopant

Lanthanides are a premium choice of dopant when it comes to optical amplification through doped fiber as their electronic structure paves the way for thin spectrum lines (the 4f structure being localised). The main criteria to select an element is the time characteristic of the spontaneous relaxation. Indeed, this value directly influences the quality -and feasibility- of the population inversion: the longer the time characteristic, the less likely are the electrons from transitioning to ground level. What's more is spontaneous relaxation value also guides the generation of noise in the system. Indeed the amplification system is an equilibrium between stimulated emission and spontaneous emission -which as it will described in more details in this chapter, ultimately leads to noise and can even tip the system toward the amplification of unwanted wavelength. This equilibrium is dependant on the relative time characteristics of both phenomena, meaning a longer spontaneous time relaxation leads to less constraining conditions to achieve stimulated amplification. In the case of erbium, the transitions of interest are between the levels ${}^4I_{13/2} - {}^4I_{15/2}$ and ${}^4I_{11/2} - {}^4I_{13/2}$, with the time characteristic of spontaneous relaxation is estimated at 10 ms while the non radiative's order of magnitude is set at 1 ns. This means the inversion of population between the levels ${}^4I_{13/2}$ and ${}^4I_{15/2}$ is possible -under precise pump power and wavelength properties of course.

Apart from its time characteristics, another argument in favor of erbium is its electronic diagram: the relaxations between higher levels are mainly non-radiative, meaning the Excited State Absorption (ESA) is limited but also the relaxation between the levels ${}^4I_{11/2}$ and ${}^4I_{13/2}$ yields a phonon and as such, cannot lead to amplification spontaneous emission. Finally, the cross section absorption and emission are high, allowing to accumulate significant energy in the material, all of which reachable through different pump power, from 532nm to the more democratized ones: 980nm and 1480nm. It goes without saying however that each pump wavelength comes with a precise application.

Co-doping a fiber with Ytterbium ions presents many advantages. First of all it significantly reduces the formation of ion quenching and as such increases the effective ion concentration. What's more is Ytterbium's cross section absorption is higher than Erbium's, meaning the pump power is absorbed over a smaller fiber's length. However this increase of Gain is made in detriment to the noise figure, and significant ASE signals are to be expected.

4.1.3 Rate and Propagation equations

In this section, the rate equations of the electronic levels along with the propagation of power intensity are established. Fig 4.3 is used as reference for all notations regarding electronic populations and transition coefficients:

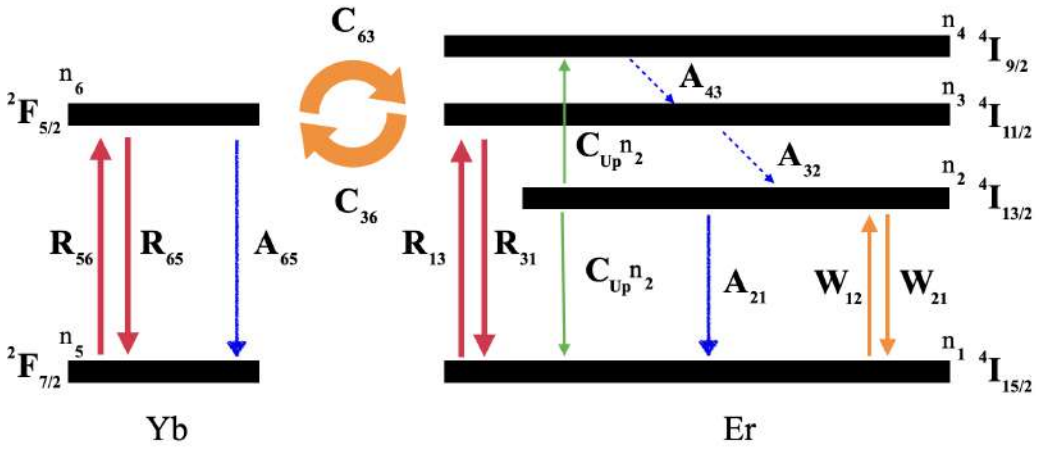

Figure 4.1 Figure of the energy levels of an ytterbium/erbium pair. The arrows in red represent the transitions driven by the pump power, in orange the transitions driven by the signal -indirect dependence of the cross transitions through the population concentration. The arrows in blue corresponds to spontaneous emissions, with dotted lines being non radiative transitions. Green is associated with up-conversion.

Where:

1. Wij and Wji represent respectively the stimulated transition rate emission and the stimulated transition rate absorption between the levels i and j.
2. A_{ji}^{NR} is the non radiative spontaneous time decay.
3. A_{ij} the radiative spontaneous emission.
4. C_{up} is the up-conversion coefficient
5. R_{36} and R_{63} are the cross transfer rate respectively between the levels 6 to 1 and 3 to 5.

From this, the variation of electronic populations can be established through conservation laws, yielding the rate equations [21]:

$$\frac{\partial n_1}{\partial t} = -(W_{12} + R_{13})n_1 + (W_{12} + A_{21}^{NR})n_2 + R_{31}n_3 + C_{36}n_3n_5 - C_{63}n_6n_1 + C_{\text{up}}n_2^2 \tag{4.6}$$

$$\frac{\partial n_2}{\partial t} = W_{12}n_1 - (W_{21} + A_{21}^{NR})n_2 + A_{32}n_3 - 2C_{\text{up}}n_2^2 \tag{4.7}$$

$$\frac{\partial n_3}{\partial t} = R_{13}n_1 - (R_{31} + A_{32})n_3 + \frac{1}{\tau_{43}}n_4 - C_{36}n_3n_5 + C_{63}n_1n_6 \tag{4.8}$$

$$\frac{\partial n_4}{\partial t} = -A_{43}n_4 + C_{\text{up}}n_2^2 \tag{4.9}$$

$$\frac{\partial n_5}{\partial t} = -W_{56}n_5 + (W_{65} + A_{65})n_6 - C_{36}n_3n_5 + C_{63}n_1n_6 \tag{4.10}$$

$$\frac{\partial n_6}{\partial t} = -(-W_{56}n_5 + (W_{65} + A_{65})n_6 - C_{36}n_3n_5 + C_{63}n_1n_6) \tag{4.11}$$

W_{ij} and R_{ij} represent the probability of an electron to interact with a photon with respect of time and as such are expressed as:

$$W_{ij} = \frac{\sigma_{ij}.\Gamma_s.(P_s + P_{ASE}^{+} + P_{ASE}^{-})}{h.\nu_s.A_{eff}} \tag{4.12}$$

$$R_{ij} = \frac{\sigma_{ij}.\Gamma_p.P_p}{h.\nu_p.A_{eff}} \tag{4.13}$$

where :

1. σ_{ij} is the cross section absorption/emission depending on the energy levels i and j.
2. $$\Gamma(\lambda) = 1 - e^{-\frac{2.b^2}{w}} \tag{4.14}$$
3. where w is given by the McCumber relation:
$$w = a(0.761 + \frac{1.237}{V^{1.5}} + \frac{1.429}{V^6}) \tag{4.15}$$
where a is the core radius, V the normalised frequency of the fiber $V = \frac{2.\pi.a.NA}{\lambda}$ and NA the numerical aperture of the fiber.

Combined with this rate equation system is the propagation system [20]:

$$\frac{dP_p^{\pm}}{dz} = \pm P_{pi}^{\pm}.(\Gamma_{pi}.(\sigma_{pi}^{e}.n_2 - \sigma_{pi}^{a}.n_1) - \alpha_{pi}) \tag{4.16}$$

$$\frac{dP_s}{dz} = P_s.(\Gamma_s.(\sigma_s^{e}.n_2 - \sigma_s^{a}.n_1) - \alpha_s) \tag{4.17}$$

$$\frac{dP_{YtASE}^{\pm}}{dz} = \pm P_{YtASE}^{\pm}.(\Gamma_s.(\sigma_s^{e}.n_2 - \sigma_s^{a}.n_1) - \alpha_s) \pm h.\nu.\sigma_e^{Yb}.\Delta f.n_6 \tag{4.18}$$

$$\frac{dP_{ErASE}^{\pm}}{dz} = \pm P_{ErASE}^{\pm}.(\Gamma_s.(\sigma_s^{e}.N_2 - \sigma_s^{a}.n_1) - \alpha_s) \pm h.\nu.\sigma_e^{Er}.\Delta f.n_2 \tag{4.19}$$

The coupled equations allow to estimate both the population inversion as a function of the power of the signals at play, along with a contribution of the noise and the the Gain. Solving this system is costly in resources.

4.2 Steady State Amplification

When implementing an Erbium-Ytterbium Fiber Amplifier, conducting a numerical simulation under steady state conditions is the first step to take. Establishing a reliable steady-state framework yields a first approximation to the behaviour of the system along with laying the foundation for time-dependence implementation.

4.2.1 Algorithm structure

The resolution of the rate equation system along with the coupled Power equation is implemented as described in Fig 4.2:

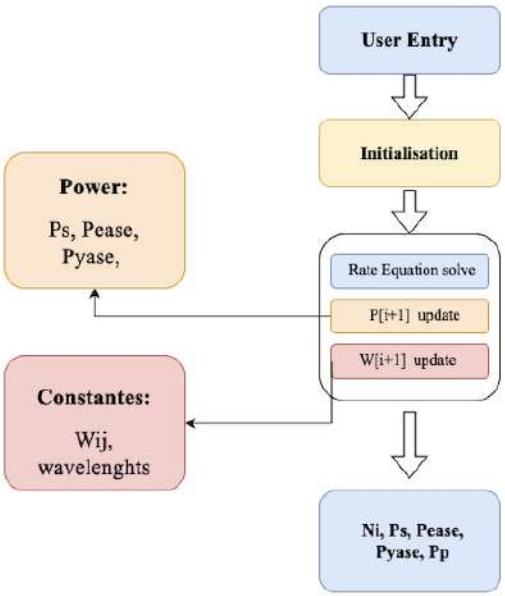

Figure 4.2 Structure of the algorithm in steady state. Power and Constants are both classes introduced during the initialisation and called upon and updated during the loop

Rate equations: are set in steady state. Since the resolution is set in steady state and given the conservation of the respective erbium electronic populations and ytterbium electronic populations, the system is reduced to:

$$f_1 = W_{12}(N_{Er} - N[0] - N[1] - N[2]) - (W_{21} + A_{21}^{NR})N[0] + A_{32}N[1] - 2C_{\text{up}}N[0]^2 \quad (4.20)$$

$$f_2 = R_{13}(N_{Er} - N[0] - N[1] - N[2]) - (R_{31} + A_{32})N[1] + \frac{1}{\tau_{43}}N[2] - C_{36}N[1](f_{cyb}N_{Yb} - N[3]) + C_{63}(N_{Er} - N[0] - N[1] - N[2]N[3]) \quad (4.21)$$

$$f_3 = -A_{43}N[2] + C_{\text{up}}N[0]^2 \quad (4.22)$$

$$f_4 = -(-W_{56}(f_{cyb}N_{Yb} - N[3]) + (W_{65} + A_{65})N[3] - C_{36}N[1](f_{cyb}N_{Yb} - N[3]) + C_{63}N[3](N_{Er} - N[0] - N[1] - N[2])) \quad (4.23)$$

with $\mathrm{N} = \begin{pmatrix} n_2 \\ n_3 \\ n_4 \\ n_6 \end{pmatrix}$ Given the non-linearity of the system, the function fsolve from the scipy library is used, with the convergence method 'hybrid' to ensure both a rapid convergence toward the solution.

Power equation system: in the present case, the power at step i+1 are determined considering the power at step i through the explicit Euler method:

$$\frac{\partial P_{type}}{\partial z} = \frac{P_{type}(z+dz) - P_{type}(z)}{dz} \tag{4.24}$$

leading to:

$$\frac{\partial P_{type}}{\partial z} = \frac{P_{type}[i+1] - P_{type}[i]}{dz} \tag{4.25}$$

and so:

$$P_p[i+1]^{\pm} = P_{pi}[i]^{\pm}(1 \pm dz.(\Gamma_{pi}.(\sigma^e_{pi}.N[i][0] - \sigma^a_{pi}.(N_{Er} - N[i][0] - N[i][1] - N[i][2])) - \alpha_{pi})) \tag{4.26}$$

$$P_s[i+1] = P_s[i](1 \pm dz.(\Gamma_{si}.(\sigma^e_{si}.N[i][0] - \sigma^a_{si}.(N_{Er} - N[i][0] - N[i][1] - N[i][2])) - \alpha_{si})) \tag{4.27}$$

$$P_{YtASE}[i+1] = P_{YtASE}[i]^{\pm}(1 \pm dz.(\Gamma_{yase}.(\sigma^e_{Yase}.N[3] - \sigma_{Yase}.(N_{Yb}.f_{yb} - N[3]) - \sigma_{Er}.(N_{Er} - N[i][0] - N[i][1] - N[i][2])) - \alpha_s)) \pm h.\nu.\sigma^{Yb}_e.\Delta f.N[3] \tag{4.28}$$

$$P_{ErASE}[i+1]^{\pm} = P_{ErASE}[i]^{\pm}(1 \pm dz.(\Gamma_s ease.(\sigma^e_{ease}.N[i][0] - \sigma^a_{ease}.(N_{Er} - N[i][0] - N[i][1] - N[i][2])) - \alpha_s)) \pm h.\nu.\sigma^{Er}_e.\Delta f.N[i][0] \tag{4.29}$$

$$\tag{4.30}$$

From this resolution's structure, the backward propagation, whether it be ASE or pump, is an issue, as the initial parameters are given at the entry of the fiber. What's more is coefficient of the rate equation, and so the electronic populations cannot be calculated at the end of the fiber without precise knowledge of the pulse profile. That's why, while the backward solutions are calculated through iterative convergence with the conditions:

1. $P_{pump}(x = L)$=30W
2. P^-_{ASE}(x=L)=$P^+_{ASE}(x = 0)$

4.2.2 Constant Estimation

Before evaluating the numerical performances of the simulation, it is necessary to evaluate some parameters of the fiber.

Effective N_{Er} concentration: while some companies specify the erbium concentration in the technical files of the fiber, this is not the case here and as a result, an estimation of the erbium ion concentration must be made. Providing a homogeneous concentration of the ion of interest in the fiber, the concentration is obtained through the absorption value at 1535nm:

$$\alpha_{1535} = \Gamma_s.\sigma_s^a.N_{Er} \tag{4.31}$$

with Γ_s defined as before, σ the absorption coefficient of erbium at 1535nm. As a result, he effective concentration of Erbium ion is therefore estimated at $3.58.10^{25}$ ion/m^3.

Effective N_{Yb} concentration: in a similar fashion the Ytterbium concentration is estimated, this time from the absorption coefficient at 976nm. Since the absorption value in the cladding was provided, the absorption follows the expression:

$$\alpha_{976} = (1 - \Gamma_p).(\sigma_{Ybp}^a.N_{Yb} + \sigma_{Erp}^a.N_{Er}) \tag{4.32}$$

The effective concentration of ytterbium ion is therefore estimated at $1{,}56.10^{26}$ ion/m^3.

Coupled Erbium/Erbium fraction: with relative high ion concentration, the risk of the formation of an erbium-pair system increases. As mentioned before, the quenching phenomenon increases with the erbium concentration and can significantly impair the performances of the amplifier. In a simple erbium doped fiber, a concentration of $3{,}58.10^{25}$ ion/m^3 would lead to a fraction of clustering of $\sim 7\%$. However as the fiber is co-doped with Ytterbium ions, which lowers significantly the formation of erbium ion pair, the formation of cluster is neglected.

Coupled Ytterbium-Erbium fraction: with the respective concentration being properly evaluated comes the necessity to determine the fraction of coupled Ytterbium/Erbium pairs. Indeed recent studies on the subject [21] tend to demonstrate that not all Ytterbium ions, being in higher concentration than their erbium counterpart, are not all paired to Erbium. The ratio of Ytterbium/Erbium is reported to be set at 2.5. Given the previous estimation of ion concentration, 57.3% of Ytterbium ion is considered coupled to Erbium ions.

Up conversion constant C_{up}: In order to determine an order of magnitude of the Up-conversion constant, this coefficient is dependant on the concentration of erbium ion [41]:

$$C_{up} = \frac{4.\pi}{3}.\frac{R_o^6}{R_{E/E}^3.\tau_{21}} \tag{4.33}$$

with R_o being the critical interaction distance and $R_{E/E}$ the average separation between uniformly distributed erbium ions. R_o is estimated at:

$$R_o = (N_{Er})^{-1/3} \sim 3nm \tag{4.34}$$

As for $R_{E/E}$, as ion clustering is not considered, one can estimate that:

$$N_{Er} = \frac{4\pi}{3}.R_{E/E}^3/m^3 \tag{4.35}$$

The constant's expression is therefore:

$$C_{up} = \frac{16\pi^2}{9}.\frac{R_o^6.N_{Er}}{\tau_{21}} \sim 4.1.10^{-23}m^3.s^{-1} \tag{4.36}$$

The Cross relaxation coefficient C_{cr}: similarly as the Up conversion constant, C_{cr} is given by the expression:

$$C_{cr} = \frac{4\pi}{3}.\frac{R_o^6}{R_{Y/E}^3.\tau_{65}}m^3.s^{-1} \tag{4.37}$$

Given the concentrations, $R_{Y/E}$ is estimated at 0.416 nm, leading to a coefficient value of $3.3.10^{-20}$ $m^3.s^{-1}$.

4.2.3 Numerical precision evaluation

Before evaluating the gain in steady state, the performances of the algorithm are evaluated through two criteria:

Spatial resolution:

indeed as the spatial path increases, so will the execution time. To do so, all parameters -Length, power, signal. Final output is calculated numerically for a interval of dz values:

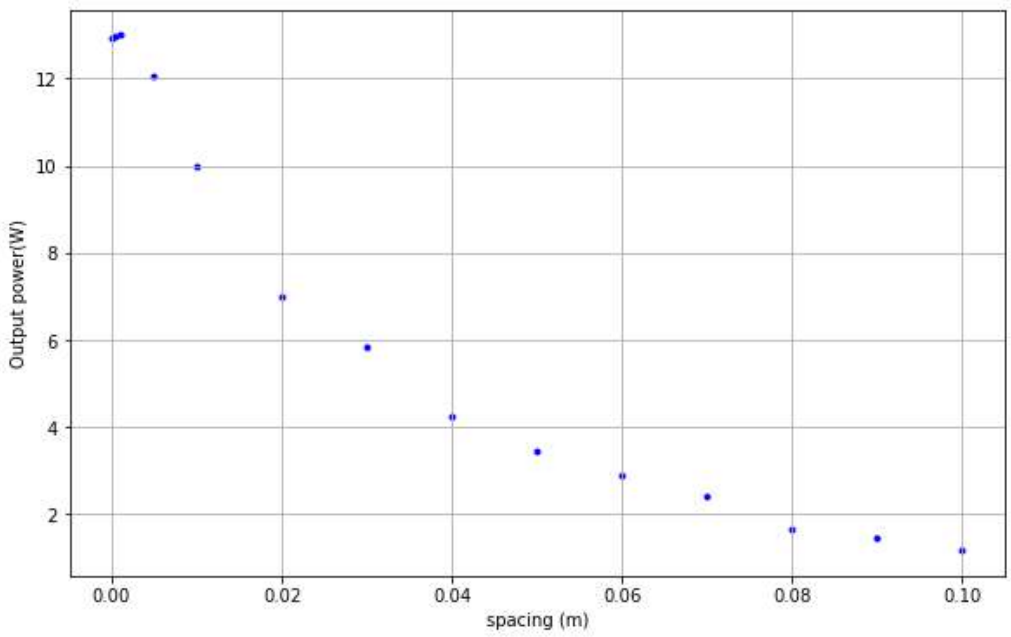

Figure 4.3 Evolution of the final output power relative to the spatial spacing (m)

The evolution of power and as such gain is highly dependant to the elementary spacing of the fiber, and not without reason. Indeed along a length of dz, the electronic populations are constant, and as such a high dz lowers the sensibility of the system the mitigates the electronic population equilibrium. In this case of figure, the system reaches convergence for dz=0.01 m.

Initial solution:

Given the non linear structure of the system, local extrema are expected. Not only would this yield a different final gain from experimental data but this could also causes divergences point.

Nevertheless, the initial situation can easily be evaluated through the time constant of respective transitions. Indeed, given the cross section absorption of both Ytterbium and Erbium, the former are expected to bear the brunt of photon absorption, and as the pump wavelength is set at 976 nm, the cross section emission and absorption are equal. Two cases of figure arises:

1. In forward configuration, as the pump power is high with a low signal, the electronic levels are expected to be set in low gain, and one can therefore reasonably consider the initial fraction of Ytterbium to be set around $0{,}5.\mathrm{N}_{Yt}.\mathrm{f}_{Yb}$

2. In backward configuration, as the pump power is low with a low signal, so long that the pump power is superior to the threshold value, the electronic levels are expected to be set in low gain, and one can therefore reasonably consider the initial fraction of Ytterbium to be set around 0,5.N_{Yt}.f_{Yb}.

4.2.4 Amplifier Optimization

Simulation

For the first estimation of gain, the input signal is considered continuous with the initial power set to be the average value measured while designing the stretcher. Table 4.1 is a recapitulation of all parameters:

Table 4.1 Numerical parameters of the steady state simulation of EYDFA

parameters	dz (m)	$P_s(W)$	$P_{pump}(W)$	T (K)
value	0.001	0.038	30	300

While the maximum pump power is set at 30W, the configuration remains to be determined. The pump power can be propagated in the same direction as the signal -forward configuration-, opposite -backward configuration- or both -bidirectional. It is generally accepted that backward configuration yield a higher gain, and as such, higher ASE signals.

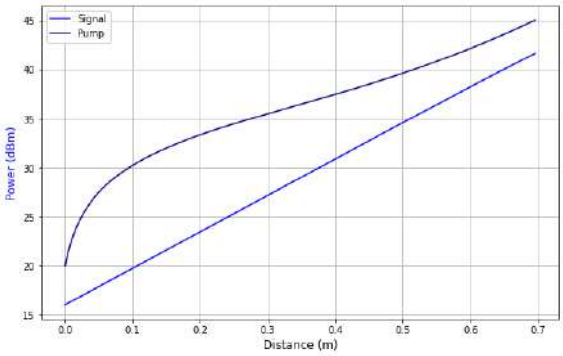

(a) Signal (in blue) and pump (in black)gain evolution over the fiber's length.

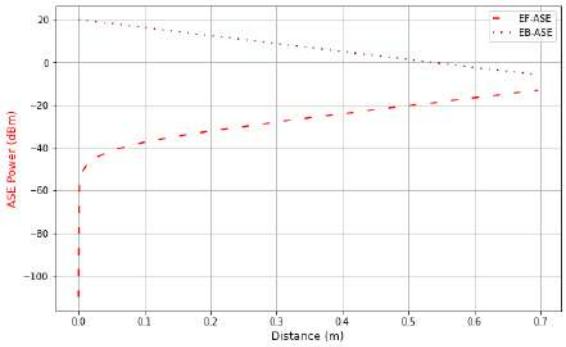

(b) Evolution of the gain of the stimulated spontaneous emission generated by erbium ion (estimated at 1573nm).

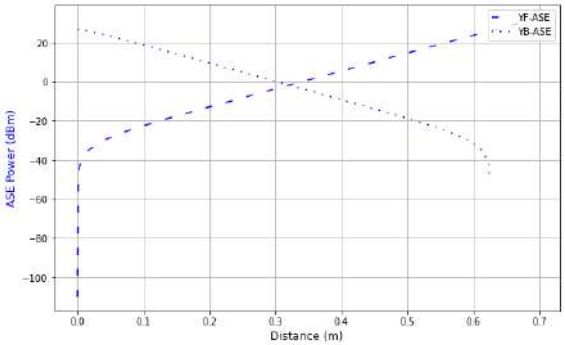

(c) Evolution of the gain of the stimulated spontaneous emission generated by ytterbium ion (estimated at 1030 nm).

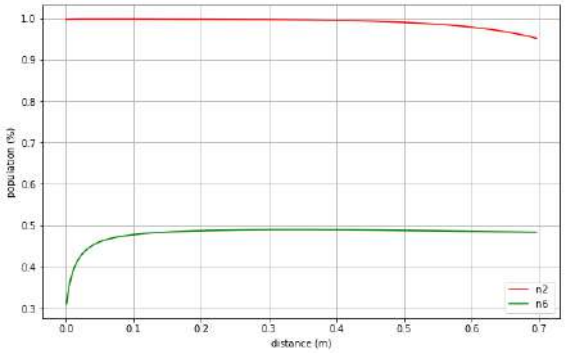

(d) Evolutuon of the n_2 and n_6 electronic populations (normalized to total erbiun and ytterbium concentration, respectively)

Figure 4.4 Simulation results for initial values of signal power and available pump power.

All in all the system yield the results Tab 4.2:

Table 4.2 powers of both signal, pump, and ASE noises, in a forward an backward configuration

parameters	L (m)	$P_s(W)$	Ef-ASE (W)	Eb-ASE (W)	Yf-ASE (W)	Yb-ASE (W)
forward	0.698	13.14	4.29e-05	0.4e-5	0.28	1.48
backward	0.685	13.67	4.456e-05	1.e-4	1.33	0.5

Achieving an output power of 13.67 W in continuous wave operation corresponds to setting the gain at 25.33 dB, with a pump efficiency of 45.5%. In terms of signal quality, the noise figure (NF) is estimated to average at 5 dB given the average electronic populations of the levels 2 and 6.

Discussion

While steady-state analysis may not accurately depict the amplification of a picosecond pulse signal, it does offer an initial estimate of the maximum output power achievable from the system. Pulsed signal amplification is less efficient as the system lacks the time to reach maximum power output from its electronic population.

However, one crucial aspect overlooked in the simulation is the transmission at the fiber ends, considered so far to be ideal. In practical applications, this assumption does not hold true. This reflection imposes limitations on the system. Not only does the reflection yield a seed for increased ASE, but it also has the undesirable effect of raising the temperature, dedicate more pump power to a different wavelength from the signal, thereby reducing the system's efficiency.

To mitigate the risk of catastrophic lasing at 1030nm, one solution involves virtually reducing the reflection coefficient of the input fiber by increasing the length of the fiber. This may appear counter-intuitive, a longer fiber yielding less ASE and therefore spontaneous light can propagate on a longer distance. However, since the pump power remains at the same level, the characteristic pump absorption length remains at the same value as well and all signals propagate through a medium in which a great majority of electron are set at ground state. In this configuration, optical signals are absorbed by the medium and two cases of figure arises:

1. 1030nm-signal is absorbed by a ytterbium ion. Either the ion is coupled to an erbium ion and cross-transition is likely to occur, or the ion isn't and the absorption will eventually

lead to a spontaneous emission or will contribute to the ASE signal at another time. Either way, the ASE signal is decreased.

2. 1573nm signal is absorbed by erbium ion, either leading to a stimulated emission at a later time or spontaneous emission

The signal at 1573nm is therefore bound to be attenuated, if only slightly. However, as Ytterbium ion's concentration is higher by 22%, associated with higher cross-sections, 1030nm signals are expected to be far more attenuated than the 1573nm-signal. This will be reviewed in more details in the next section, as the optimal length of the pulsed-signal amplifier is determined.

Another approximation was made during the numerical evaluation of the steady state amplification. As determined in the previous section, only a fraction of the Ytterbium ions have formed pairs with erbium ion -this being the reason on why erbium clustering is significantly lowered. This means the medium presents Ytterbium ion unaccounted for. It has been implicitly assumed for the light to be absorbed and re-emitted at the same wavelength. Yet as demonstrated while calculating the ASE noise generated by Ytterbium ion, the system demonstrates quasi-three up to four-level system behaviour. This means Ytterbium ions are likely to generate ASE noise as well.

4.3 Pulse amplification

In this section, a numerical modelling of EYDFA systems in steady state was successfully implemented, leading to a reliable evaluation of P_{out} and ASE contributions in steady state. The immediate step would be to introduce time dependency in the system in order to evaluate the power output of the pulse.

4.3.1 Initial Time dependant simulation

While implementing the time-dependency in the previous system would yield the amplification of the signal, this would require as it is tremendous numerical ressources. Before doing so, let's consider simplifying the system:

1. Discard the up-conversion.

2. Discard the n_3 population.

3. Discard the transfer rate C_{36} and C_{63}, meaning the transfer of electron from level 3 to 6 and 6 to 3 to be instantaneous.

While neglecting the up-conversion and the n_3 population would only lead to minimal numerical error, well under 5% given the characteristics of the system, discarding the cross transfer rate leads to catastrophic numerical drift.

As it is, the system of rate equations remains highly non-linear and the implementation of a time-dependant system would require significant numerical resources, all the more that all time evaluations were realised in a forward configuration. In a backward configuration, as mentioned before, photons are propagated back and forth until convergence of a solution, which can multiply ten-fold the time of simulation, depending on the precision of the initial guess.

4.3.2 Time dependant evaluation

As mentioned early in this chapter, the characteristics response time of the EYDFA is ~ 100 μs. This is four order of magnitude the time between the propagation of two pulses. Consequently, the electronic states cannot significantly recover between successive pulse propagation and as such the system is bound to reach, if not a steady-state, an equilibrium between the electronic depletion due to pulse amplification and its recovery. The goal of this section is to determine this equilibrium.

Modified Rate equation system

As state in the previous section, any estimation cannot be applied to the rate equation system as it is without significant numerical ressources. Simplifications must be made in order to reach a first estimation of gain. To do so, let's assess an order of magnitude of all transition time characteristics Table 4.3:

Table 4.3 Time characteristics of electronic transitions, estimated in magnitude.

Transition	τ_{56st}	τ_{65st}	τ_{65sp}	τ_{13st}	τ_{31st}	τ_{12st}	τ_{21st}	τ_{21sp}	τ_{Up}	τ_{Cross}	τ_{32}
O.d.M (μs)	4	4	11000	40	inf	50	25	10000	1000	10^0	0.001

In light of the values obtained here, the approximations are made:

Spontaneous transitions: are neglected in the time span of a pulse propagation. This approximation entirely discard the possible generation of spontaneous light and so neglects

the ASE generation. This step is necessary to reach a first estimation of gain but comes at the risk of designing an amplifier crippled with parasitic Y-ASE lasing. To prevent this, an estimation of ASE generation will be discussed later in the chapter.

Up-conversion: is neglected, as it was expected given the results of the previous section.

n_3 population: The transition from level 3 to 2 takes place within 1 ns. This is highly favorable the present analysis. Indeed this time characteristic exceeds the duration of the pulse by a factor 100, as such the variations of n_3 relative to the pulse's referential can be neglected and n_3 is considered constant within the time frame of the pulse. What's more is it is as well significantly shorter than the pulse propagation time, meaning a great majority of electrons at level 3 transitioned toward level 2 by the time the pulse is propagating through the medium. Consequently, the population n_3 can be considered null. As a result, electrons in levels 6 are considered to directly transition toward level 2.

Cross-ion transition: as one can expect, approximations done regarding the R_{36} and R_{63} is to be tackled with great care. Regarding the Ytterbium to Erbium transition, as it is relative to the n_1 population and is superior to 0.9 μs (corresponding to the case of figure where all electrons are set at ground state). So long that the ground state population is superior to $0.045N_{Er}$ the cross ion transition isn't discarded. This however, has a displeasing consequence, given the fact the n_3 population was neglected. By considering the Ytterbium-Erbium cross-transition by neglecting the equivalent operation, a current of charge appears in the medium and as magnetic field arises from the pair. In the absence of the signal, the pump power is considered constant and as such the symmetry of the problem ensures the generation of an opposing magnetic field. Without a sudden variation of electromagnetic field, breaking the symmetry of the problem, cross-transition cannot take place. For this reason, the cross-ion transition Ytterbium-Erbium is only considered within the pulse propagation.

With the approximations, the rate equation system of the electronic populations become:

$$\frac{\partial n_1}{\partial t} = -\frac{\partial n_2}{\partial t} \tag{4.38}$$

$$\frac{\partial n_2}{\partial t} = W_{12}n_1 - (W_{21})n_2 + C_{63}n_1n_6 \tag{4.39}$$

$$\frac{\partial n_5}{\partial t} = -\frac{\partial n_6}{\partial t} \tag{4.40}$$

$$\frac{\partial n_6}{\partial t} = -(-W_{56}n_5 + (W_{65})n_6 + C_{63}n_1n_6) \tag{4.41}$$

Leading to the rate equations:

$$\frac{\partial n_2}{\partial t} = W_{12}N_{Er} - (W_{21} + W_{12})n_2 + C_{63}n_1n_6 \tag{4.42}$$

$$\frac{\partial n_6}{\partial t} = W_{56}N_{Yb} - (W_{65} + W_{56})n_6 - C_{63}n_1n_6 \tag{4.43}$$

As it stands, the system could be solved via numerical simulation. However, given the parameters of the problems, additional approximations can be made to decrease the complexity of the system without compromising the reliability of the solution.

One of the key hypothesis of this resolution is that all electronic populations slightly varies around an equilibrium. As such, the variation of electronic populations are approximated as followed:

$$n_i(t) = n_{i0}.(1 - e^{-t/\tau_{ij}}) \tag{4.44}$$

with τ_{ij} the characteristic time of the transition at play. Given the rate equations established in this chapter, τ_{ij} can easily be expressed as a function of wavelength and power. From this point and for the sake of clarity, the convention is established :

$$n_i(t) = n_{i0}.y_{ij}(\lambda, P, t) \tag{4.45}$$

Since the central wavelength and the pump power wavelength are the only to wavelength considered in this estimation, the notation is simplified to:

$$n_i(t) = n_{i0}.y_{ij}(P, t) \tag{4.46}$$

As for the cross-ion transition, its expression differs from intra-ion transition. However a similar expression is considered:

$$y_{cross} = (1 - e^{-t/\tau_{cross}}) \tag{4.47}$$

with

$$\tau_{cross} = \frac{1}{N_{er}.(1 - x_2).C_{36}} \tag{4.48}$$

In a similar fashion, the simplified notation is considered:

$$y_{cross} = y_{cross}(x_2, t) \tag{4.49}$$

Last but not least, the pulse's shape is approximated to rectangular. With this and the

notation in mind, the integration of the rate system yields:

$$0 = (1 - 2.x_6).y_{56}.(P_p, \tau_{recover}) - y_{cross}(x_2, \tau_{pulse}).x_6 \tag{4.50}$$

$$0 = y_{cross}(x_2, \tau_{pulse}).x_6.f_{yb}.N_{Yb} - (x_2.y_{21}(P_s, \tau_{pulse}) - (1 - x_2).y_{12}(P_s, \tau_{pulse}).N_{Er} \tag{4.51}$$

Numerical resolution

The initial rate system has been reduced to two equations with two unknown variables. The conservation of energy leads to the expression of the :

$$P_s(x + dx) = P_s(x) + ((y_{em}.x_2 - y_{abs}.x_1).dx.\pi.r^2.N_{Er})\frac{h.\nu}{\tau_{pulse}} \tag{4.52}$$

As for the pump power, set in a backward configuration as per the study realised in steady state :

$$P_{pump}(x) = P_0.e^{-\Gamma_p.(\sigma_{aYb}.(1-2.x_6).N_{Yb}+N_{Er}.x_1.\sigma_{sEr}).(L-x)} \tag{4.53}$$

Given the value of the cross section absorption of Erbium, along with the ratio of Ytterbium population coupled to the erbium ion, the expression can be simplified to:

$$P_{pump}(x) = P_0.e^{-\Gamma_p.\sigma_{aYb}.(1-2.x_6).N_{Yb}.(L-x)} \tag{4.54}$$

All that remains now is to implement the numerical resolution of the system, with the algorithms structure described Fig 4.5:

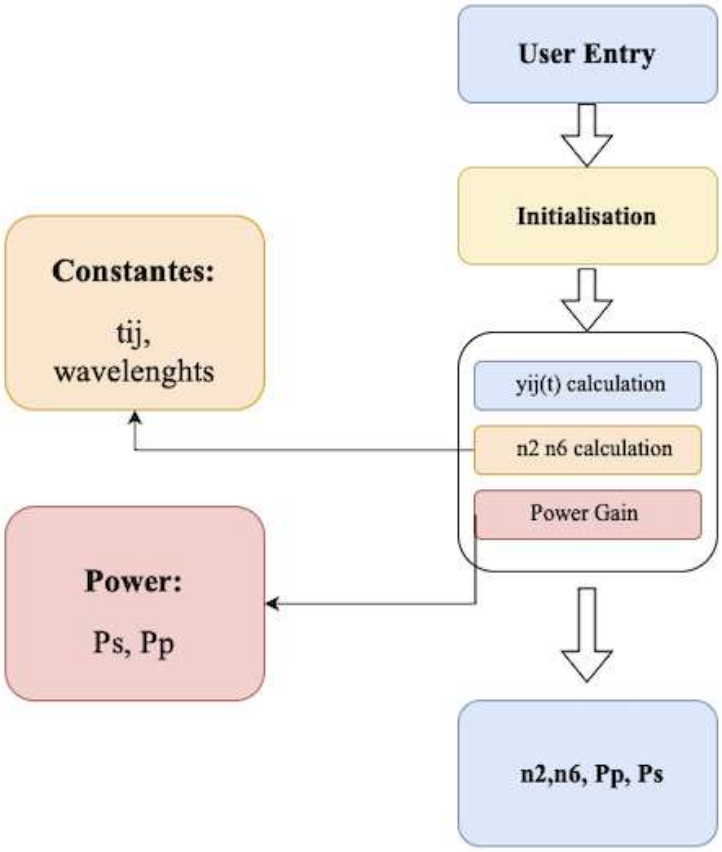

Figure 4.5 Structure of the time-dependant algorithm.

Note: To ensure an accurate evaluation of the gain, great care must be put in the predetermination of:

1. The initial guess of the solutions, as detailed before while solving non linear systems, the performance of the fsolve function from the scipy library (python), whether it be in terms of time execution and convergence speed, is strongly linked to the accuracy of the initial proposition. Given the ratio $\tau_{pulse}/\tau_{propagation}$, this initial guess is assumed to be the steady-state populations determined previously.

2. The length of the fiber. Indeed, as defined above, the pump power is directly linked to the fraction of electron in the n_6 level. Should the fraction reach . There is as such a risk of having the pump power reach 0 while the system estimate the fraction of n_6 to be maximal (0.5 of Ytterbium electron population). The expression along with the system is relevant so long that the pump power is superior to the power threshold -and guarantees the minimal population inversion. To prevent any overestimation of the

gain, the maximum length of the fiber corresponds to the length at which the pump power is above the power threshold. According to the previous study in steady state, this limit is estimated at 51 mW. The optimal length determined in steady state is set as an initial guess.

3. reflection coefficient of the fibers' ends as it determined the input's peak power along with the final out peak power:

$$R = \left| \frac{n_1 \cos(\theta_i) - n_2 \cos(\theta_t)}{n_1 \cos(\theta_i) + n_2 \cos(\theta_t)} \right|^2 \tag{4.55}$$

As the interface is set between air and silica (this being an approximation, as Erbium and Ytterbium are respectively under 1000 ppm and 45000ppm) with an angle of $\sim 8°$, it is therefore estimated at 3.25%.

The gain and electronic populations are evaluated for initial peak power ranging from 0.5 W to 4.25W.

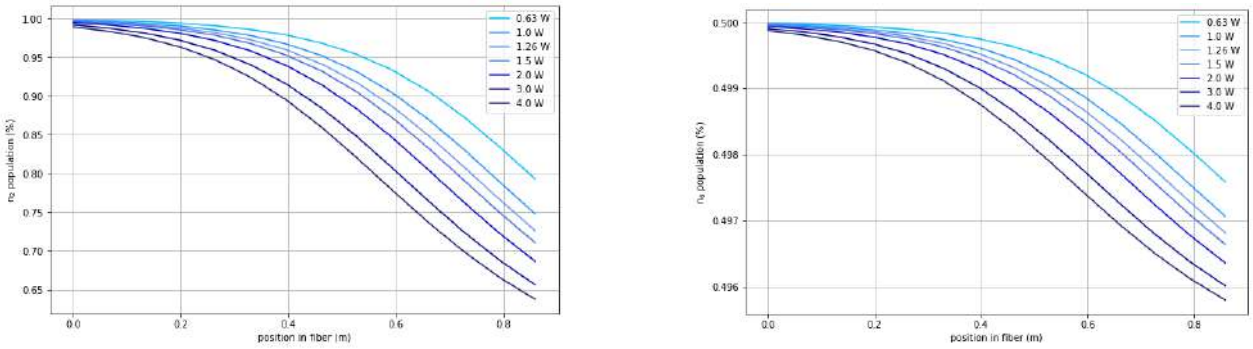

(a) Evolution of electronic population of the level 2 (Erbium)

(b) fraction of the electronic population of the level 6 (Ytterbium)

Figure 4.6 Evolution of the electronic populations of the high energy levels of the Erbium-Ytterbium pair, relative to the position in the fiber along with the initial peak power. The values are the peak power of the pulse before entering the fiber.

The length is determined through the pump power value at the beginning of the fiber. So long that P[0]>P_{sat}, the simulation operates within the hypothesis that stimulated emission is possible. The fiber's length is therefore extended until this condition is not respected. The populations are expected to decrease rapidly under the minimal populations needed to ensure stimulated emission, effectively preventing gain beyond this point.

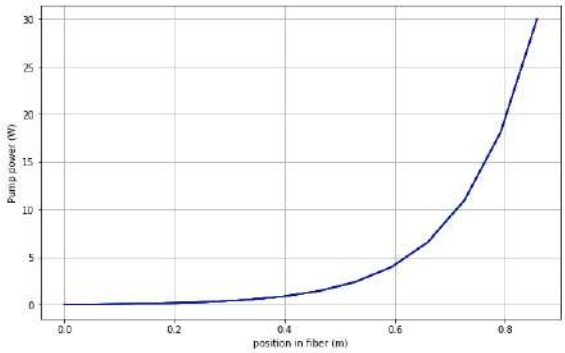

(a) Evolution of the pump power relative to the position in the fiber

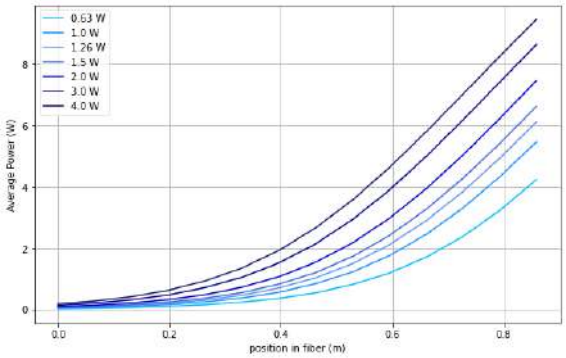

(b) Evolution of the average output power relative to the position in the fiber and relative to the initial peak power

Figure 4.7 Power evolution relative to the fiber length

In order to estimate the output power of a gaussian pulse, two cases are considered: a square pulse of peak power $I_0/2$ and a square pulse of peak power I_0. Both cases scenario are either an over-estimation of the amplified output power -as high power favors stimulated emission over spontaneous emission. As such, the gain at I_0 and $I_0/2$ -with respective output power at 5.86W and 3.60W- can be considered to be a first approximation and provide an uncertainty interval. The final output power gain is therefore estimated at 4.73 ± 1.13W.

With this estimated gain, the pump efficiency is evaluated at 16%, with a global Noise Figure of $\sim$ 7.5 dB.

4.3.3 ASE estimation and final fiber length

As already tackled in steady state, Y-ASE generation is an issue, as it redirect a significant fraction of the pump power toward another wavelength. This is all the more problematic that, because of the respective ion concentration and cross-section, the system is likely to tip toward the 1030nm. To prevent this it was briefly mentioned. The idea is to extend the fiber's length to retrieve the power directed toward Y-ASE. The amplifier becomes effectively a two system amplifier:

1. An EYDFA pumped at 976nm, the initial pump power. The main interest in pumping at 976nm is the cross section absorption/emission of ytterbium at this wavelength, allowing to increase the amount of energy stored in the medium. As demonstrated before, a significant part of the energy is directed toward 1030nm signal.

2. An EYDFA pumped at 1030nm, the source being the backward Y-ASE. The cross-sections of Ytterbium at this wavelength push the system toward emission rather than absorption. However, because of energy conservation, when pumping a fiber at a wavelength λ_p, the generated ASE is bound to have a wavelength superior to λ_p. This section of the fiber therefore absorbs Y-ASE at 1030nm to favor the generation of Y-ASE at higher wavelength, more precisely 1064nm. Given the cross-section constants of Ytterbium at 1064nm, the overall Y-ASE noise is less favorable and its contribution decreased. This can be pushed by applying a 1064nm at the entry of the fiber.

The fiber is extended by a factor 3 in order to ensure that the Y-ASE noise is absorbed by the fiber and its contribution at the input of the pump power limited. The final fiber length is therefore set at 2.54 m.

4.4 Experimental results

With the numerical determination of the amplifier parameters completed, the experimental implementation of the amplifier is currently in progress.

4.4.1 Presentation of the setup

The setup, Fig 4.8 is composed of 2.54m of double clad PM EYDF (PLMA- EYDF-25P/300-HE, Nufern) with terminaisons polished at 8°. The pump is set in a backward configuration. Since the signal and the pump have different diameters, lens with respective focal of 18mm and 60mm were used to collimate, the issue being due to the large fiber's diameter, there is a risk of coupling the signal into higher modes. However, since higher modes have lower overlap coefficients, the gain is expected to be lower. Therefore to ensure the signal is mostly coupled into the fundamental mode, the position of the 18-mm focal lens is adapted until maximum power is achieved. Similarly the position of the 60mm-lens is adapted to ensure the maximal collimation of the pump power into the fiber. Both the pump and signal are then coupled with a 1180nm-dichroïc mirror (DMLP1180R, Thorlab). The reflection of signal input is estimated under 0.8% (Thorlab) while the transmission of the pump signal is estimated at less than 0.01%. Then both signals are collimated in the fiber with achromatic C-coated lens (AC254-035-C,Thorlab), with a reflection of 0.12% for the signal input and 2.7% for the pump signal.

Given the pump power and the expected pump efficiency, thermal effects are expected. To prevent the fiber's temperature from increasing -which would impact negatively the gain- the

fiber was placed on a circular metallic holder.

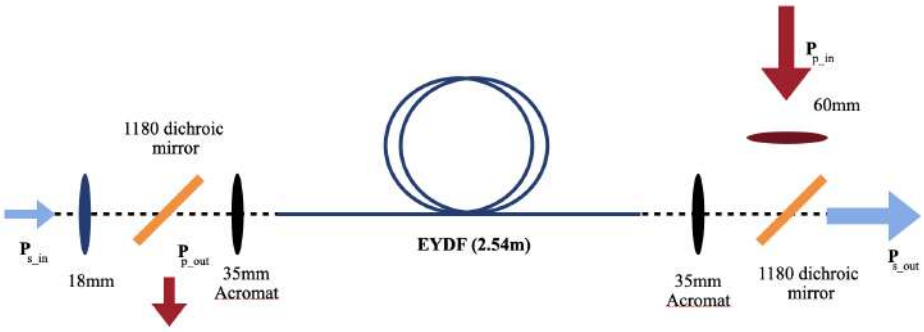

Figure 4.8 Amplification set up, inspired from [1]

4.4.2 Preliminary observations

The pump power is first set at 6W while the signal average power was estimated at 20 mW.

The reflection and transmission coefficient of the dichroïc mirror at 976nm and over the 1540-1610nm bandwidth is estimated respectively at 99.48% and over 99.27%. The signal is therefore composed solely of contribution at 1530-1610 nm wavelength, being the pulsed signal along with E-ASE forward signal. The The DC-component can be attributed to E-ASE and the AC component is attributed to the pulsed signal. A gain of 6.97 dB is observed, corresponding to an average power of 100 mW. This result is used to validate the numerical model. Based on these input powers and pump power, the model predicts an output power of 0.0836 ± 0.0278 W. The experimental results fall within the predicted values of the model. As power was increased, irreversible damage was inflicted on the fiber.

CHAPTER 5 CONCLUSION

5.1 Summary of Works

In order to achieve a matched stretcher/compressor set, three configurations, the Offner, the Martinez, and finally the Treacy grating pairs were investigated. The ranges of all parameters were evaluated until a consensus was reach that matches both the Offner stretcher and the Treacy compressor. The design was then slightly put off-balance in order to compensate dispersion taking place in the amplifier's fiber. To this end, optical aberrations were put in use to mitigate the third order discrepancy between the stretcher and the compressor. In the absence of fiber, the pulse FWHM is estimated at 631 fs through an IAC trace, which is expected to yield a final pulse FWHM of 243 fs after propagation in the fiber.

The amplifier's design was realised in two steps: first by implementing a classic steady-state resolution of both electronic rate equations and power propagation, and in a second time by implementing time dependence. Numerous structures were considered in order to introduce time dependence to the numerical simulations, however they were either too demanding in ressources or would deviate from the physical reality. Another approach was conducted. Given the characteristic times at play, the system was considered to be in relative equilibrium to steady-state and small temporal variations were introduced through the electronic populations. For a length of 0.85m, the output gain was estimated at 4.73W with an uncertainty of 1.13W and is assumed to be the maximum gain to be achieved by the system. Following this, ASE generation was evaluated and the fiber's length increased to 2.54m in order to mitigate the power loss induced by ASE. This numerical model of the pulse amplification was confronted with early findings done at 6W with an initial pulse power of 20mW. The output average power is estimated at 0.1 W, which is within the prediction of the model: 0.0836 ± 0.0278 W.

5.2 Limitations

This work, like any endeavor, is subject to limitations. Indeed, the experimental approach advocated for a flexible design of the setup.

Regarding the stretcher-compressor, all alignments and distance control between optics were achieved manually. While reasonable precision has been attained, there is room for improve-

ment and a true retrieval of the initial 100 fs should be pursued. Furthermore, during the design of both setups, fourth-order dispersion was entirely neglected. This approximation was made under the assumption that, given the pulse duration, the influence of fourth-order dispersion would be more corrective in nature. What's more is the measurement were made either with an oscilloscope or an IAC. While information regarding spectral phase was retrieved, a FROG measurement would characterize the entirely spectral phase, quantify the dispersive wave and the high order dispersion.

In all numerical simulations, the flatness of the gain was an implicit assumption, first in steady state and even more so in time-dependent simulations. However, given the shape of the pulse at the input of the fiber, this assumption may not entirely hold. Additionally, while a heatsink was implemented, as commonly done in literature, this aspect was not considered during the design phase. High temperatures could alter the electronic population dynamics, and achieving the target gain without a larger cooling system may be overly optimistic.

For simplicity's sake, only one spatial mode was considered during gain simulation, based on the core radius of 25m. However, this assumption is flawed as the overlap of higher spatial modes is lower than that of L_{00}. This affects all aspects of amplification, from the rate equations where coefficients are expected to be lower, favoring spontaneous emission over stimulated emission, to a smaller photon influx. The accuracy of the prediction is therefore dependent on the fraction of pulse power transferred to higher spatial modes.

5.3 Future Research

All these limitations of the design and simulations can be addressed systematically.

The initial focus of the stretcher-compressor process is on enhancing the precision of the gratings' angles and their relative positions to each other and other optics. To achieve this, motorized angular and plane stages will be incorporated. The objective is to align the second and third orders according to theoretical criteria. Once this alignment is perfected, attention will turn to addressing fourth-order dispersion. This involves calculating the respective fourth-order dispersion generated by both the compressor and the stretcher, as well as characterizing the fourth-order dispersion of the fiber. Following the evaluation of the fourth-order dispersion contribution, compensation methods will be explored. Unlike third-order dispersion, methodologies for compensating fourth-order dispersion have yet to be widely adopted. However, in recent years, there have been advancements in this area. Further investigation is

required to determine whether a slight adjustment of the convex mirror's focal length would be sufficient to introduce the necessary fourth-order dispersion to enhance the quality of the output pulse. The characterization of the pulse will also be achieved with a FROG trace in order to better apprehend the dispersive wave.

The amplifier will undergo further modifications. While the preliminary results align with the simulations, they were conducted using relatively low power signals. Pump power must be increased to reach the maximum of 30W. This necessitates a shift in focus towards cooling the fiber, which can be achieved by enhancing the cooling system and/or introducing a continuous wave at 1064 nm at the fiber entry to mitigate Ytterbium Amplified Spontaneous Emission (Y-ASE) noise and cool the system. Additionally, the introduction of a third optical signal will likely decrease the gain of the 1573nm pulse, the extent of which requires further investigation.

REFERENCES

[1] K. Charan, "Fiber based ultrafast laser sources for multiphoton imaging," 2017.

[2] B. Caroline, *Fundamentals of Biomedical Optics*, 1st ed. Montreal, Canada: Pollux Editions, 2017.

[3] Kebes, "Water absorption data," *Wikipedia Encyclopedia*, 2024. [Online]. Available: https://fr.m.wikipedia.org/wiki/Fichier:Absorption_spectrum_of_liquid_water.png

[4] S. Gomès, A. Assy, and P.-O. Chapuis, "Scanning thermal microscopy: A review," *physica status solidi (a)*, vol. 212, no. 3, pp. 477–494, 2015. [Online]. Available: https://onlinelibrary.wiley.com/doi/abs/10.1002/pssa.201400360

[5] M. Tamamitsu, K. Toda, H. Shimada, T. Honda, M. Takarada, K. Okabe, Y. Nagashima, R. Horisaki, and T. Ideguchi, "Label-free biochemical quantitative phase imaging with mid-infrared photothermal effect," *Optica*, vol. 7, no. 4, pp. 359–366, 2020.

[6] F. M. Gasparoli, A. Escobet-Montalbán, J. Early, G. D. Bruce, and K. Dholakia, "Is laser repetition rate important for two-photon light sheet microscopy?" *OSA Continuum*, vol. 3, no. 10, pp. 2935–2942, 2020.

[7] J. Tang, J. Ren, and K. Y. Han, "Fluorescence imaging with tailored light," *Nanophotonics*, vol. 8, no. 12, pp. 2111–2128, 2019.

[8] R. Jauberteau, A. Tonello, Y. Sun, M. Zitelli, M. Ferraro, F. Mangini, P. Parra-Rivas, T. Mansuryan, Y. Arosa, V. Couderc *et al.*, "Light tailored by multimode fiber for multiphoton fluorescence microscopy," *arXiv preprint arXiv:2404.15507*, 2024.

[9] D. Strickland and G. Mourou, "Compression of amplified chirped optical pulses," *Optics communications*, vol. 55, no. 6, pp. 447–449, 1985.

[10] B. García-Ramiro, J. Arrue, M. A. Illarramendi, F. Jimenez, J. Zubia, R. Evert, and D. Zaremba, "Numerical simulation of optical amplifiers based on eu-doped polymer optical fibers," in *2017 International Conference on Numerical Simulation of Optoelectronic Devices (NUSOD)*, 2017, pp. 175–176.

[11] R. Paschotta, J. Nilsson, A. Tropper, and D. Hanna, "Ytterbium-doped fiber amplifiers," *IEEE Journal of Quantum Electronics*, vol. 33, no. 7, pp. 1049–1056, 1997.

[12] A. Naji, B. A. Hamida, X. Cheng, M. A. Mahdi, S. Harun, S. Khan, W. Al-Khateeb, A. Zaidan, B. Zaidan, and H. Ahmad, "Review of erbium-doped fiber amplifier," *International Journal of the Physical Sciences*, vol. 6, no. 20, pp. 4674–4689, 2011.

[13] E. Desurvire, J. R. Simpson, and P. Becker, "High-gain erbium-doped traveling-wave fiber amplifier," *Optics letters*, vol. 12, no. 11, pp. 888–890, 1987.

[14] C. Giles and E. Desurvire, "Modeling erbium-doped fiber amplifiers," *Journal of Lightwave Technology*, vol. 9, no. 2, pp. 271–283, 1991.

[15] A. Malakzadeh, R. Pashaie, and M. Mansoursamaei, "Gain and noise figure performance of an edfa pumped at 980 nm or 1480 nm for dofss," *Optical and Quantum Electronics*, vol. 52, pp. 1–16, 2020.

[16] L. Qiao and P. J. Vella, "Ase analysis and correction for edfa automatic control," *Journal of lightwave technology*, vol. 25, no. 3, pp. 771–778, 2007.

[17] P. Booker, R. Caspary, J. Neumann, D. Kracht, and M. Steinke, "Pump wavelength dependence of ase and sbs in single-frequency eydfas," *Optics Letters*, vol. 43, no. 19, pp. 4647–4650, 2018.

[18] A. Lubana, S. Kaur, and Y. Malhotra, "Er–yb co-doped fibre amplifier performance enhancement for super-dense wdm applications," in *International Conference on Innovative Computing and Communications: Proceedings of ICICC 2020, Volume 2*. Springer, 2021, pp. 855–866.

[19] S. Muhd-Yassin, M. K. Anuar, M. Zulkifli, S. Harun, H. Abdul-Rashid, and M. Abd-Rahman, "56 db gain eydfa with improved noise figure with dual-stage partial double pass configuration," *Optik*, vol. 123, no. 20, pp. 1884–1887, 2012.

[20] L. Dong, T. Matniyaz, M. T. Kalichevsky-Dong, J. Nilsson, and Y. Jeong, "Modeling er/yb fiber lasers at high powers," *Optics Express*, vol. 28, no. 11, pp. 16 244–16 255, 2020.

[21] ——, "Modeling er/yb fiber lasers at high powers," *Optics Express*, vol. 28, no. 11, pp. 16 244–16 255, 2020.

[22] E. Treacy, "Optical pulse compression with diffraction gratings," *IEEE Journal of Quantum Electronics*, vol. 5, no. 9, pp. 454–458, 1969.

[23] H. Huang, "Generation, optimization and amplification of ultrashort infrared pulses," Ph.D. dissertation, 2023.

[24] O. Martinez, "3000 times grating compressor with positive group velocity dispersion: Application to fiber compensation in 1.3-1.6 µm region," *IEEE Journal of Quantum Electronics*, vol. 23, no. 1, pp. 59–64, 1987.

[25] I. V. Yakovlev, "Stretchers and compressors for ultra-high power laser systems," *Quantum Electronics*, vol. 44, no. 5, p. 393, 2014.

[26] G. Cheriaux, P. Rousseau, F. Salin, J. Chambaret, B. Walker, and L. Dimauro, "Aberration-free stretcher design for ultrashort-pulse amplification," *Optics letters*, vol. 21, no. 6, pp. 414–416, 1996.

[27] V. Ivanov, "Compact optical grating compressor," *Optics Express*, vol. 30, no. 20, pp. 35 338–35 347, 2022.

[28] S. Bucht, D. Haberberger, J. Bromage, and D. Froula, "Methodology for designing grism stretchers for idler-based optical parametric chirped-pulse-amplification systems," *JOSA B*, vol. 36, no. 8, pp. 2325–2337, 2019.

[29] Z. Li, C. Wang, S. Li, Y. Xu, L. Chen, and Y. Dai, "Fourth-order dispersion compensation for ultra-high power femtosecond lasers," *Optics Communications*, vol. 357, pp. 71–77, 11 2015.

[30] Vyhlídka, D. Kramer, A. R. Meadows, and B. Rus, "Offner stretcher aberrations revisited to compensate material dispersion," *Optics Communications*, vol. 414, pp. 207–211, 2018.

[31] Š. Vyhlídka, D. Kramer, G. Kalinchenko, and B. Rus, "Seidel aberrations in grating pulse stretchers," *Optics Express*, vol. 24, no. 26, pp. 30 421–30 432, 2016.

[32] Y. Dai and C. Xu, "Generation of high repetition rate femtosecond pulses from a cw laser by a time-lens loop," *Optics express*, vol. 17, pp. 6584–90, 05 2009.

[33] K. Wang and P. Qiu, "Nonquadratic spectral phase aberration with quadratic temporal phase modulation in an actively modulated ultrafast laser system," *IEEE Journal of Quantum Electronics*, vol. 50, no. 8, pp. 639–644, 2014.

[34] W. Zhang, W. Kong, G. Wang, F. Xing, F. Zhang, H. Zhang, and S. Fu, "Review of pulse compression gratings for chirped pulse amplification system," *Optical Engineering*, vol. 60, no. 2, pp. 020 902–020 902, 2021.

[35] B. Lemoff and C. Barty, "Quintic-phase-limited, spatially uniform expansion and recompression of ultrashort optical pulses," *Optics letters*, vol. 18, no. 19, pp. 1651–1653, 1993.

[36] F. Verluise, V. Laude, Z. Cheng, C. Spielmann, and P. Tournois, "Amplitude and phase control of ultrashort pulses by use of an acousto-optic programmable dispersive filter: pulse compression and shaping," *Optics letters*, vol. 25, no. 8, pp. 575–577, 2000.

[37] V. Leshchenko, A. Povrozin, and S. Karelin, "Calculation of stretching factor for optical pulse stretcher," , 2015.

[38] G. A. Mourou, T. Tajima, and S. V. Bulanov, "Optics in the relativistic regime," *Reviews of modern physics*, vol. 78, no. 2, p. 309, 2006.

[39] S. Toenger, R. Mäkitalo, J. Ahvenjärvi, P. Ryczkowski, M. Närhi, J. Dudley, and G. Genty, "Interferometric autocorrelation measurements of supercontinuum by two-photon absorption in a gap photodetector," in *2019 Conference on Lasers and Electro-Optics Europe European Quantum Electronics Conference (CLEO/Europe-EQEC)*, 2019, pp. 1–1.

[40] S. K. Kaushalya and H. Fried, "Measuring ultra-short pulse widths before and after the objective with a home built autocorrelator," 2021.

[41] M. Federighi and F. Di Pasquale, "The effect of pair-induced energy transfer on the performance of silica waveguide amplifiers with high er/sup 3+//yb/sup 3+/ concentrations," *IEEE Photonics Technology Letters*, vol. 7, no. 3, pp. 303–305, 1995.

APPENDIX A CHARACTERISTICS

Table A.1 Cross-section values of EYDFA (source N-Light) in $10^{-25}\mathrm{m}^2$

type	1573 nm	1030 nm	1064 nm	976 nm
Ytterbium absorption	-	1	0.2	25
Ytterbium emission	-	6	1.1	25
Erbium absorption	1.1	-	-	2.49
Erbium emission	2.49	-	-	0

Table A.2 Fiber characteristics (source Coherent, Nufern)

type	radius (μm)	α_{1535nm} core (dB)	α_{976nm} cladding (dB)
value	12.5	85	2.6

Table A.3 Reflection coefficient Treacy (source Spectrogon, Thorlab). All values are taken for a wavelength of 1573nm, in all cases, the mirrors are coated and aluminium, and the angle of incidence is 8° unless mentioned otherwise

component	grating	Mirror (Silver)
Reflection	92	99.88

Table A.4 Reflection coefficient Martinez (source Spectrogon, Thorlab). All values are taken for a wavelength of 1573nm, in all cases, the mirrors are coated and aluminium if not mentioned otherwise

component	grating	Mirror	Lens C-Coated	Mirror (Silver)
Reflection	92	95.00516	99.1	99.88

Table A.5 Reflection coefficient Offner (source Spectrogon, Thorlab, Eskma). All values are taken for a wavelength of 1573nm, in all cases, the mirrors are coated and aluminium if not mentioned otherwise (S for Silver)

component	grating	Mirror	Mirror (S, AOI at 45°)	Convex Mirror (S)	Concave Mirror (S)
Reflection	92	95.00516	97.96	96	96